The temporal evolution of the swell and magmatic fluxes along the Louisville hotspot

by

Madison Nichole Smith

B.S., Kansas State University, 2018

A THESIS

submitted in partial fulfillment of the requirements for the degree

MASTER OF SCIENCE

Department of Geology
College of Arts and Sciences

KANSAS STATE UNIVERSITY
Manhattan, Kansas

2021

Approved by:

Major Professor
Dr. Claudia Adam

Copyright

Abstract

The interaction of an ascending mantle plume and a moving lithosphere produces two main surface observations: a volcanic chain and swell. The study of the temporal evolution of the magmatic flux, Q_v, associated with the volume of magmatic material, and the buoyancy flux, Q_s, associated with the swell, provides important information on plume phenomenology, plume temporal evolution, and its interactions with the large-scale mantle flow and the drifting lithosphere. This study focuses on the temporal evolution of the Louisville hotspot. We utilize the MiFil filtering method to separate the swell and magmatic components. We translate a sliding box along the track to compute the temporal evolution of Q_s and Q_v. For the past ~35 m.y. Louisville's fluxes have been increasing, indicating an increase in hotspots activity which contradicts previous reports about its decline. This could be caused by variations in the degree of melting, an increase in the plume temperatures, or movement of a deep mantle source. Peaks in both fluxes are found at 2, 12, and 23 Ma along the Louisville seamount chain. Such variations, with a 10-20 m.y. periodicity have been reported for the Hawai'i, Walvis, and St. Helena chains. They may be induced by the tilt of the plume conduit. Variations on a scale of 5 m.y. are identified along the Louisville chain, and have also been reported on St. Helena, Walvis, and Hawai'i. They may be the result of solitary waves that form within the plume conduit after mantle motions have deformed it, allowing instabilities to form and increase plume activity. We find the buoyancy flux, B, associated with the Louisville chain to be 0.65 Mg s^{-1}, similar to the value reported by King and Adam (2004), which is consistent with a shallow plume origin.

Table of Contents

List of Figures

List of Tables

Chapter 1 - Introduction

1.1. Hotspot Origins

The formation of hotspots has been studied since the idea of hotspots originated with J. Tuzo Wilson, in 1963. Originally, it was thought that all hotspots have a mantle source from deep within the Earth (Wilson, 1963). More recently, the most widely accepted hypothesis states that plumes originate from the destabilization of a boundary layer (Whitehead, 1975; Courtillot et al., 2003). Between the core-mantle boundary and the surface, the main three boundary layers are (1) the D" layer just above the core-mantle boundary (CMB), (2) the boundary layer between the lower and upper mantle, and (3) the base of the lithosphere (Sleep 2002; Anderson 2000). Therefore, three different types of hotspots will coexist, and each type will have its own unique source. Plumes initiating by the destabilization of the D" layer will then have a deep origin (Olsen et al., 1987; Bercovivi et al., 1997). The second type of hotspot will originate along the boundary layer between the lower and upper mantle, and is created along transient domes (i.e., the top of superswells) (Anderson, 1998; Courtillot, 2003). Such a scenario has been proposed to account for the French Polynesia hotspot chains. The plumes creating these chains would initiate at the top of the South Pacific Superswell (Davaille et al., 2002). The third type of hotspot may originate from upper mantle features, e.g. where magma passively upwells to the surface through lithospheric discontinuities or weakness zones (Anderson, 1998).

According to Courtillot et al. (2003), a hotspot chain must satisfy five requirements to be considered created by a deep mantle plume: an age-progressive volcanic chain, flood basalts at the youngest part of the track, a large buoyancy flux, a high $^{3}He/^{4}He$ isotopic ratio in erupted basalt lavas (i.e., exceeding mid-oceanic ridge isotopic values of 7 – 9 Ra (Farley and Neroda, 1998)), and low shear wave velocities in the mantle. Based on these criteria, only seven of forty-

nine hotspots met these criteria (Courtillot et al., 2003). A more recent study by Jackson et al. (2021) reports that there are 30 hotspots that have a deep plume origin.

A plume can form due to the temperature gradient between the core-mantle boundary and the base of the lithosphere. The hot instability created by the temperature gradient is potentially brought up to the surface through mantle convection (e.g., Schubert et al., 2001). As the instability rises, the plume starts to develop a 'mushroom-shaped' head with a thinner trailing tail. The interaction between the lithosphere and the upwelling plume head causes flood basalts to form while the tail creates a volcanic trail as the lithosphere moves (Richards et al., 1989). These features are represented in Figure 1.1.

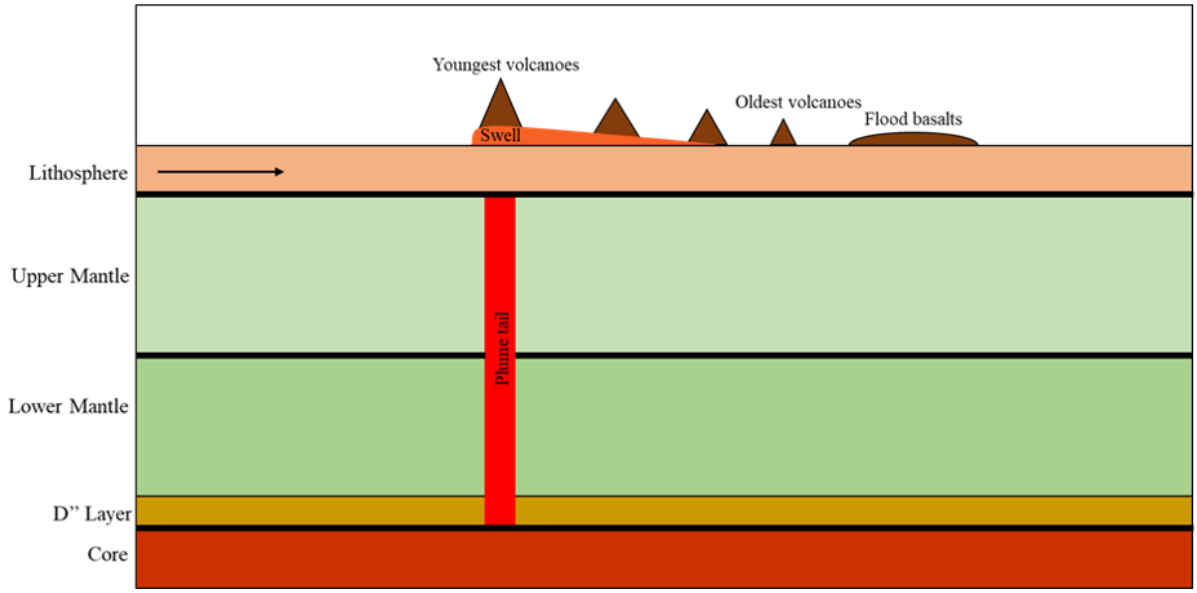

Figure 1.1. Formation of a hotspot from the destabilization of the D" Layer.
Not to scale cartoon of the formation of a mantle plume and its physical manifestations when it interacts with a moving lithosphere. Each location for a potential mantle plume to form is indicated by a bolded black line. The arrow represents the direction of lithosphere motion.

1.2. Swell Origin

The interaction between the mantle plume rising to the surface and a moving lithosphere creates the two main features along a hotspot chain: volcanoes and a swell (Crough, 1983). The volcanic chain is represented by the trail of volcanoes aligned along the direction of plate motion (Figure 1.1). They display a linear increase in the volcanism age, from the youngest part of the chain (sometimes active) to the oldest part of the chain. Swells are positive depth anomalies, generally occurring most prominently in the region of the youngest volcanic edifices of the hotspot chain, formed as a plume rises and interacts with a moving lithosphere (Crough, 1983). They can have a width of 1000-1500 km and a height of 500-1200 m (Crough, 1983). If the hotspot chains are located on the seafloor, which is the case for the chains discussed in this thesis report, the swells are anomalously shallow regions relative to adjacent seafloor (Crough, 1983).

Several hypotheses have been proposed to account for the origin of swells: sediment accumulation (Menard, 1964), crustal thickening (Betz and Hess, 1942; Watts and tenBrink, 1989), flexural rebound (Walcott, 1970) or deeper compensation (Burke and Wilson, 1976; McNutt and Bonneville, 2000). The latter hypothesis implies that there are regions associated with low density magmatic material, situated at different depths. These low-density regions, the origin of which is either thermal or chemical, require an uplift of the seafloor for the isostatic equilibrium to be satisfied. These anomalous regions can be found at the base of the lithosphere (Burke and Wilson, 1976) and at base of the crust (McNutt and Bonneville, 2000). They could also be associated with the heating and re-melting of the lithosphere (Detrick and Crouch, 1978; Crough, 1983). Sandwell et al. (1995) propose that swells could be created by lithospheric thinning. A more recent study proposes that dynamic upwellings, such as the ones associated with rising plumes, can account for the observed swells (Adam et al., 2010).

While the volcanoes and swell form at the same time, the volcanoes will be seen across the entire track while the swell will only be observed in association with the youngest part of the chain (Crough, 1983; Adam et al. 2010). Studying the temporal evolution of the magmatic and swell fluxes associated with these features may provide information on the variations of the plume activity, or on temporal variations in the plume/lithosphere interaction (Sleep, 1990; Vidal and Bonneville, 2004; Adam et al., 2007). Studies have previously been conducted along long lived hotspots by Vidal and Bonneville (2004) and Adam et al. (2007) and will be discussed in the *Background Information* section. This project will involve the study of the magmatic and swell flux along the Louisville seamount chain. We have chosen Louisville as the focus for this project because it is a long-lived hotspot that has not undergone such a study before.

Louisville is located within the southern part of the Pacific Ocean. This area of the Pacific Plate has been moving in a general northwestern direction due to the Kermadec-Tonga subduction zone and has created a volcanic chain that is 4300km in length. The track itself is separated into three segments due to two bends in the track, occurring at 47 and 25Ma, respectively, that correspond to shifts in plate motion (Davies, 1992). It has been active for ~80 m.y. with its oldest activity recorded at the Osborn seamount at 76.7±0.8Ma and its youngest activity at 1.11±.04Ma at 50^{o}26'S, 139^{o}W (Koppers et al., 2004; 2011). Figure 1.2 represents the locations, ages, and bends of Louisville's volcanic chain. We will be observing the magmatism and swell flux of this chain to better understand the plumes activity and to observe how it interacts witht the moving lithosphere.

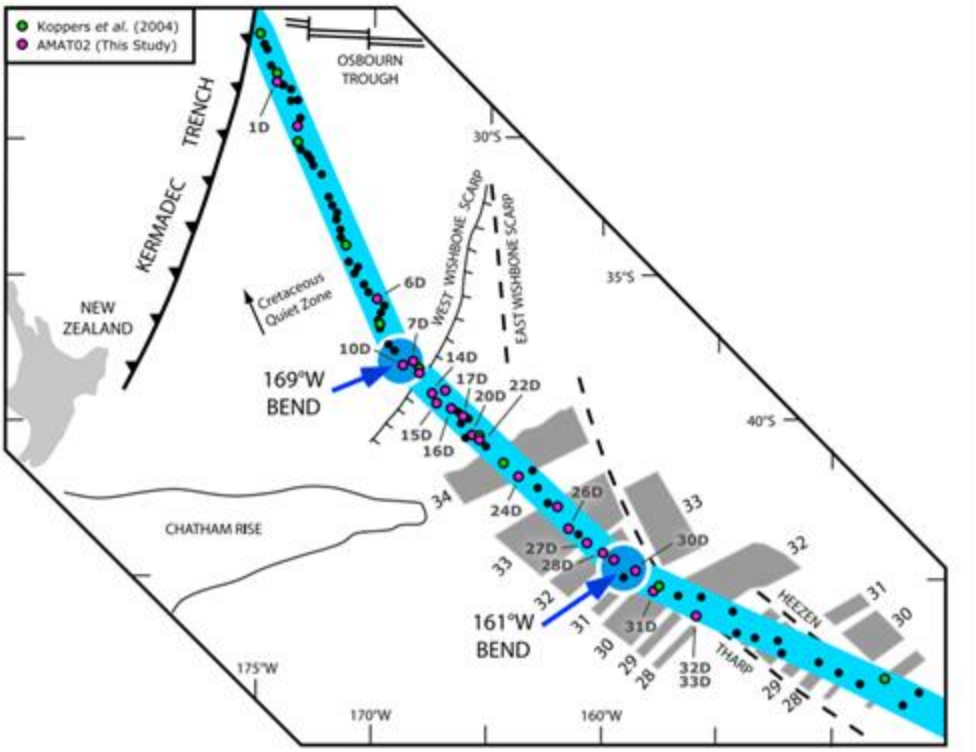

Figure 1.2. Track and geological features of the Louisville hotspot.

Black dots represent volcanoes, green dots are samples from Koppers et al. (2004). Pink dots are samples from Koppers et al. (2011). Figure from Koppers et al. (2011).

Chapter 2 - Background Information

Vidal et al. (2004) and Adam et al. (2007) have conducted studies on the temporal evolutions of the Hawaii chain in the Pacific, and the Walvis and St. Helena chains in the Atlantic, respectively. These studies provide a template for the approach used here to examine the Louisville seamount chain. We, therefore, briefly review the results from these prior studies below.

The Walvis Ridge is located in the Atlantic Ocean (Figure 2a) and volcanism ranges between ~130Ma and 1Ma. It is created by the interaction of a plume with the lithosphere (Adam et al. 2007). The plume first expressed itself on the South American plate, but then migrated under the African plate due to westward migration of a spreading axis (O'Connor and Duncan, 1990; Schilling et al., 1985). The volcanoes forming the St. Helena chain display volcanism ages between ~81Ma and 1Ma (O'Connor and le Roex, 1992). The hotspot chain consists of scattered seamounts and volcanic ridges that were created as the lithosphere moved over the plume and was interacting with a spreading ridge (O'Connor and le Roex, 1992). In Vidal and Bonneville (2004) Hawaii is described as a long-lived hotspot located in the Pacific Ocean that has experienced at least 70 m.y. of activity, forming when a mantle plume started to interact with the Pacific Plate (Wilson, 1963). From ages 64.7 to 42.2 Ma, the Pacific Plate moved in a 172.5^{o}N direction; from 42.2 Ma plate motion changed to a 110^{o}N direction, creating a bend in the hotspot chain at the Daikakuji seamount (Dalrymple and Clague, 1976; Dalrymple et al., 1980). The trends of these tracks are shown in Figure 2.1.

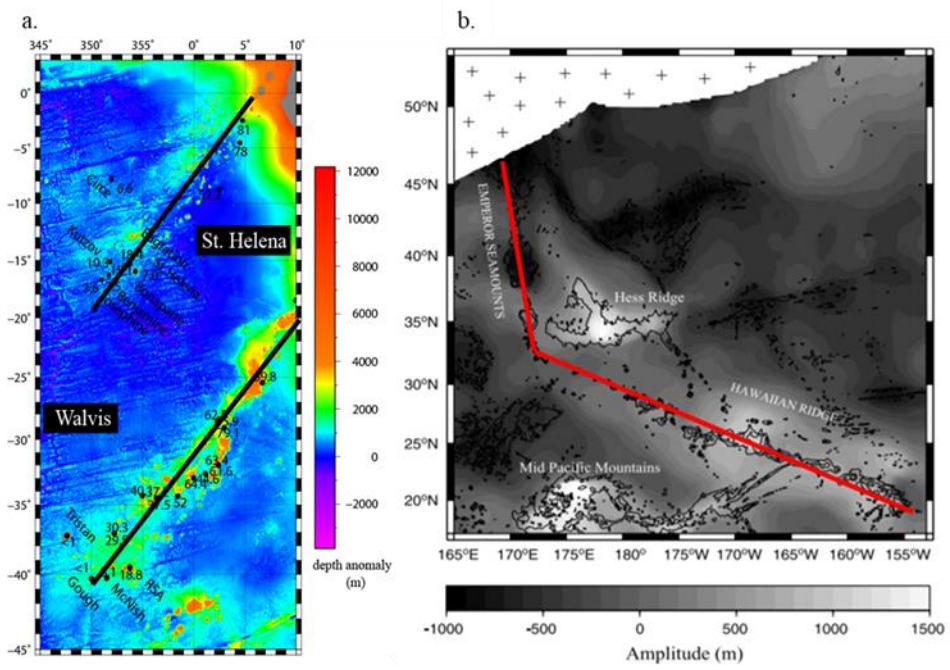

Figure 2.1. Tracks of (a) St. Helena, Walvis, and (b) Hawai'i hotspots.
Trends of Walvis and St. Helena are represented by black lines. The Hawai'i-Emperor seamount chain trend is represented by a red line. Walvis and St. Helena contain the ages of each seamount. Figure is modified from (a) Adam et al. (2007) and (b) Vidal and Bonneville (2004).

We are reviewing these studies because we are using the same methods as the authors to calculate the temporal evolution of the magmatic and swell fluxes of the Louisville hotspot. The computed fluxes from Louisville will be compared to these studies in order to interpret the trends of the plumes activity.

2.1. Temporal Evolution Calculation

In this study, the volume of volcanic material erupted on the seafloor is defined as the magmatic flux, Q_v, while the buoyancy of the plume is defined as the swell flux, Q_s (Sleep, 1990; Vidal et al., 2004; Adam et al., 2007). To calculate the Q_v and Q_s of these previous studies, the volcanic chain and swell of each hotspot were separated from one another. To separate influence of the volcanic edifice from the swell, the authors used the MiFil filtering method, developed by

Adam et al. (2005). After the filtering, they computed the volcanism, Q_v, and swell, Q_s, through the "sliding box" method. The volumes of swells and volcanic edifices encompassed in this box, translated along the main axis, are computed for each iteration step. This allows the computation of the magmatism and swell fluxes. A detailed description of these methods is provided in the *Methods* section.

These results of previous studies are reported in Figure 2.2. They show that for Walvis and St. Helena, Q_v is decreasing as the age of volcanism gets younger. This means that the volume of volcanic material being erupted is decreasing, suggesting that the plume's activity is decreasing (Adam et al., 2007). For Hawaii, Q_v is increasing with decreasing age of volcanism. This means that the volume of volcanic material being erupted is increasing, indicating an increase of plume activity (i.e., production of magma) (Vidal et al., 2004). Each hotspot also experiences variations in Q_v with wavelengths of 10-20 m.y. (Walvis and St. Helena) and 5 m.y. (St. Helena, Walvis, and Hawaii). The 10-20 m.y. variations can be caused by the dip of the plume conduit being more than 60^o (Whitehead, 1982) or large-scale mantle convection (Steinberger, 2000; Whitehead, 1982). The 5 m.y. variations may be caused by solitary waves being present within the plume conduit (Whitehead and Helfrinch, 1990). The maximum for Q_s of the Walvis chain occurs at ~10 Ma with two smaller ones at 38 and 54 Ma, while St. Helena has a large bump at ~ 30 Ma (Adam et al., 2007). The Q_s for Hawaii has two sharp increases, one around 13-15 Ma and another at ~5 Ma (Vidal and Bonneville., 2004). These variations are observed in both the swell and volcanism fluxes in Figure 2.2.

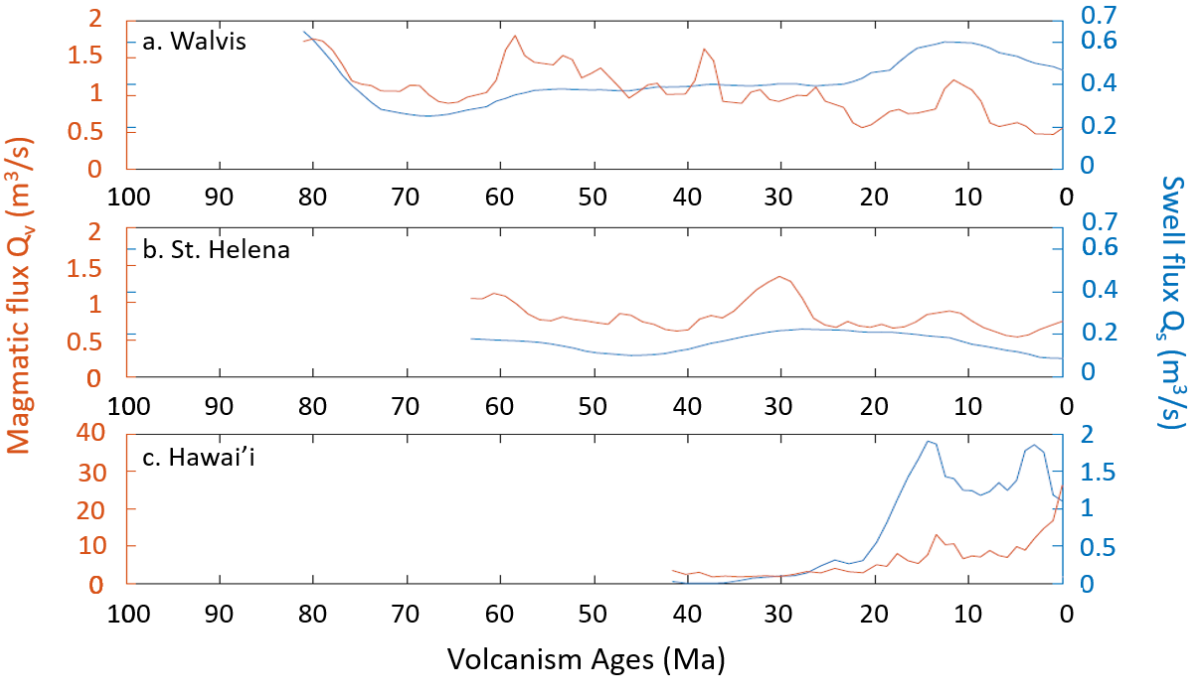

Figure 2.2. Swell (blue) and magmatic (red) fluxes of the (a) Walvis, (b) St. Helena, and (c) Hawai'i hotspots.

Figure is modified from Adam et al. (2007).

Chapter 3 - Methods

As mentioned in the *Background Information* portion of this thesis, the volcanic chain and swell are the two main topographic signatures of the interaction between a plume and the drifting lithosphere (Crough, 1983). We studied these features in order to characterize the temporal evolution of the volcanism and buoyancy fluxes.

3.1. Defining the Main Axis of the Louisville Hotspot Chain

The main axis of the Louisville hotspot follows the volcanic trail, representing the chains general trend, and is illustrated in Figure 3.1. We use the main axis defined by Koppers et al. (2004; 2011). In Figure 5, we can see that the Louisville chain is composed by three different segments, characterized by slightly different trend orientations. The bends relating the three segments occurred around 47 Ma (191^{o}W) and 25 Ma (199^{o}W) and are caused by small changes in the rotational poles (Koppers et al., 2004; 2011). Koppers et al., (2004; 2011) provide the main axis of the Louisville chain, as well the location and age of the volcanoes composing this chain. Table 1 illustrates the location and age of some of the volcanoes composing this chain. A complete table with all volcanoes within the chain is provided in Appendix Table 1.

Table 1. Latitude, longitude, and volcanic ages of some of the volcanoes along the Louisville hotspot. Modified from Koppers et al., (2004; 2011).

Latitude °S	Longitude °W	Age ± 2σ (Ma)
25.5	186.0	76.7 ± 0.8
27.5	185.7	70.8 ± 0.4
27.5	185.7	69.6 ± 0.5
27.2	186.8	68.9 ± 0.6
30.1	186.8	61.4 ± 0.5
38.2	191.3	50.1 ± 0.4
38.2	191.3	49.4 ± 0.6
28.0	191.7	48.4 ± 0.3
37.1	191.0	47.0
39.2	192.4	44.7 ± 0.4
39.7	193.3	43.3 ± 0.4
39.9	194.0	41.3 ± 0.3
40.5	194.3	40.4 ± 0.3
40.8	194.5	39.6 ± 0.3
40.8	194.5	38.9 ± 1.2
41.6	195.8	36.5 ± 0.4
41.9	196.3	34.5 ± 0.4
40.8	194.7	33.9 ± 0.3
43.6	198.5	30.3 ± 0.2
43.6	198.5	29.5 ± 0.3
44.0	199.4	26.3 ± 0.2
44.8	201.5	26.0 ± 0.3
44.6	199.9	25.0
45.4	202.3	24.6 ± 0.2
45.4	202.3	23.9 ± 0.3
46.2	204.1	21.7 ± 0.3
46.2	204.1	21.5 ± 0.2
46.2	204.1	21.6 ± 0.2
46.2	204.1	21.3 ± 0.2
48.2	211.2	13.2.7 ± 0.2
50.4	220.9	1.11 ± 0.4

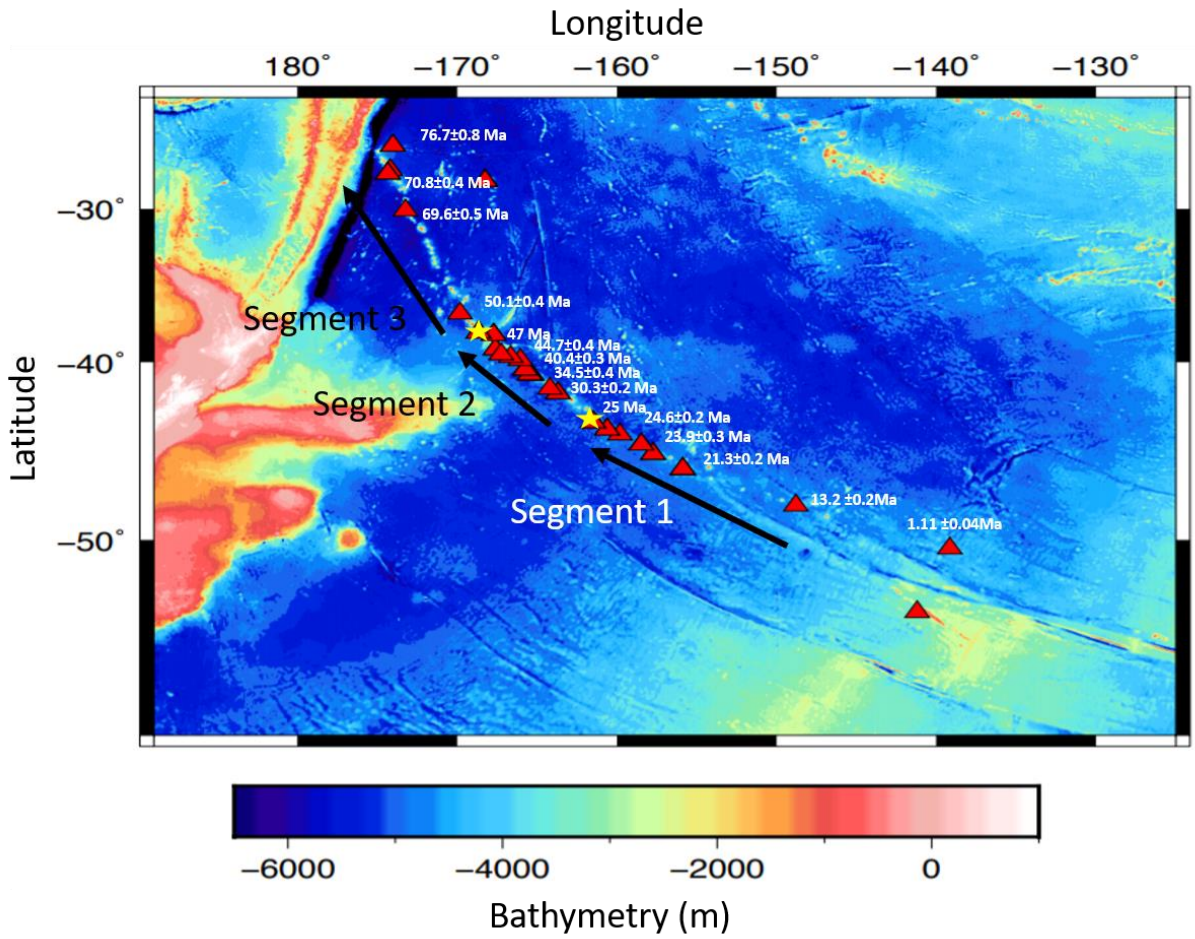

Figure 3.1. Louisville chain.

The color map represents the bathymetry along the chain. Individual volcanoes are represented by the red triangles. The ages of each seamount, extracted from Koppers et al. (2004; 2011), are reported in white next to them. The black arrows represent the main axis of the Louisville hotspot and indicate the present day and past direction of the Pacific plate motion.

We used the main axis and the ages of volcanism published by Koppers et al. (2004; 2011) to create a discrete field of volcanism age and distance from the youngest volcanoes along the main axis of the Louisville chain. As stated earlier, Koppers et al. (2004; 2011) define the main axis by three segments of slightly different orientation. In Figure 3.2a, a plot of latitude vs. longitude, the locations of the volcanoes are reported by blue stars and the extremities of each

segment are reported by red open circles. For each segment, we interpolate the latitude and longitude of the main axis, in between these two extremities (red open circles on Figure 3.2a), with a constant step of 1 km. We use the "interp1" function in Matlab for this step. Along the three segments of the main axis, represented in green, black and red in Figure 6a, we obtain the longitude and latitude of the main axis. The distance between two consecutive points is 1 km. This allows us to compute the distance from the youngest extremity of the chain (red open circle at the right side of Figure 3.2a), along the same points.

The ages of the volcanoes published by Koppers et al., (2004; 2011) are reported in Figure 3.2b as a function of the longitude. The volcanic ages are scattered because the seamount distribution along the chain is not exactly linear, and because some of the volcanoes have not been dated. In order to obtain a regular distribution of the volcanism ages along the main axis interpolated with a 1 km increment, we use the "polyfit" function in Matlab. The extrapolated volcanism ages are shown by the green, black and red lines in Figure 3.22b. In summary, this step allows us to obtain the longitude, latitude, distance from the youngest volcano, and the volcanism ages, along the main axis, interpolated with a constant step of 1 km.

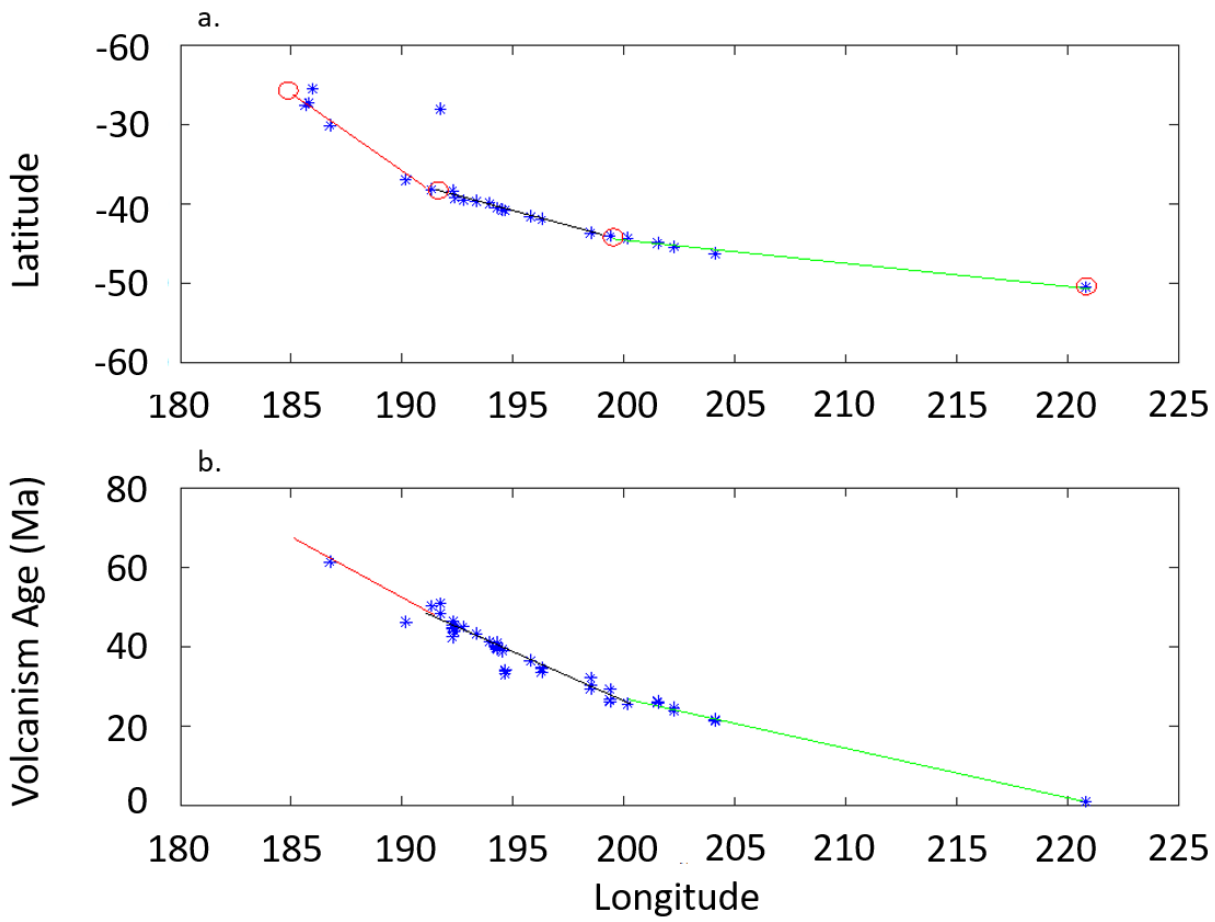

Figure 3.2. Main axis and volcanism ages along the Louisville chain.
(a.) Location of the volcanoes (blue stars), and extremities of these segments composing the Louisville seamount chain (red open circles) (b). Volcanism ages as a function of the chain longitude. The blue stars are the volcanism ages published in Koppers et al., (2004; 2011), and the green, black, and red lines, our extrapolation of the volcanism ages along each segment.

3.2. Obtaining the depth anomaly map

The depth anomaly is the difference between the observed bathymetry and a theoretical depth, describing the deepening of the seafloor as a function of its age. For the observed bathymetry, we used a digital bathymetry map designed by Becker et al. (2009). It was corrected for sediment loading by using the sediment thickness published by Divins (2011). The

theoretical depth was computed by using the Global Depth and Heat Flow Model (GDH1 model) from Stein and Stein (1992) and the seafloor age grid data from Müller et al. (2008). The GDH1 model predicts the theoretical variation of the seafloor depth as a function of its age. It has been obtained by considering constraints from several types of geophysical data: heat flow, bathymetry, and gravity. The obtained depth anomaly is reported in Figure 3.3.

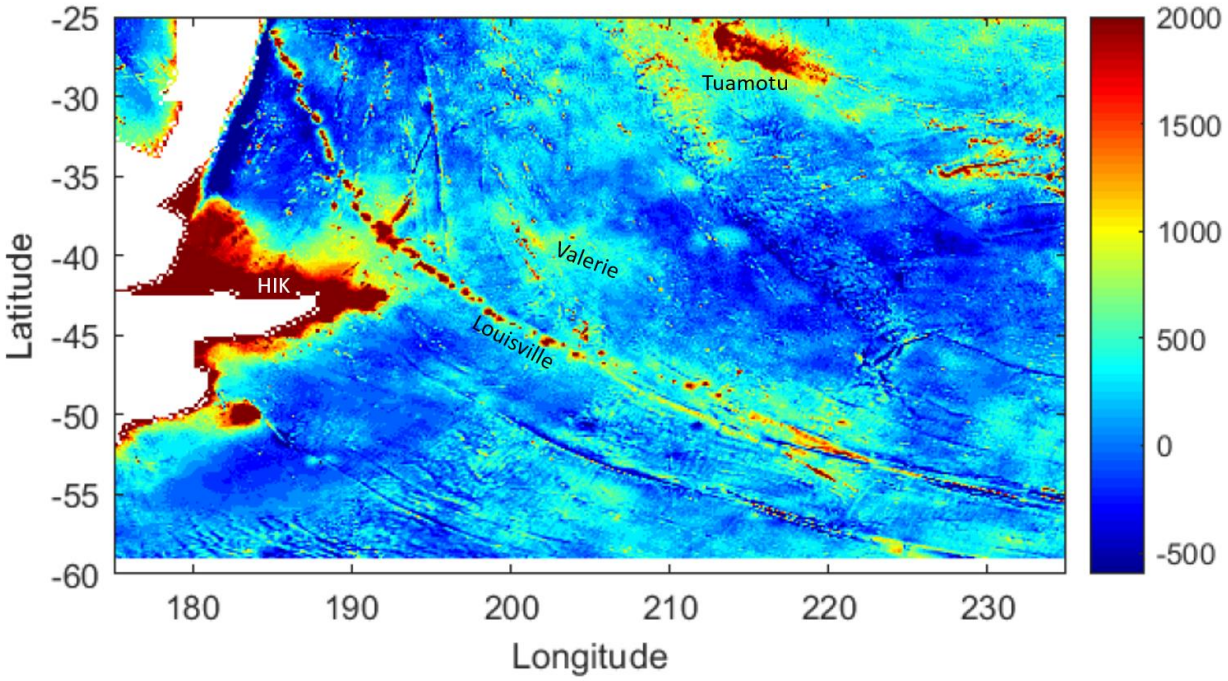

Figure 3.3. Depth anomaly map.

Depth anomaly map of the Louisville hotspot area. The colder colors represent the lower parts of the oceanic floor while the warmer colors represent the higher points. The dark red areas on the left represent the Hikurangi (HIK) plateau, the red positive depth anomaly represents the Tuamotu swell, the positive depth anomaly around latitude 40°S, longitude 205°E is associated with the Valerie seamounts.

3.3. Separation of the volcanic edifice and swell components along the Louisville hotspot

In order to quantify the temporal evolution of the Louisville hotspot, we first have to separate the contributions made to the depth anomaly from the swell and the volcanic edifice. To do this, we used a filtering method, specially designed to characterize depth anomalies emplaced on the seafloor, MiFil (Adam et al., 2005). This method has been applied to the 2-D depth anomaly grid, described in the previous section. The MiFil method has two stages. The first step involves a minimizing filter, designed to remove any topographic features related to volcanism. In the second step, the minimized grid is filtered with a median filter in order to remove any remaining depth anomaly and to smooth the resulting grid (Vidal et al., 2004; Adam et al., 2005). Detailed descriptions of each stage are in the following sections.

3.3.1. Minimization

As stated before, the main goal of the minimization stage is to remove any topographic features associated with volcanism from the swell along the hotspot track (Adam et al., 2005). For each of the point of the depth anomaly grid, i.e., for each latitude, and longitude (the red circle in Figure 3.4 represents an example of one point of the grid), we sweep a region of radius r (green circle in Figure 3.4). The minimal value of the depth anomaly of all the points encompassed in this green circle is then imposed in the center of the green circle.

Mathematical demonstrations show that such filtering eliminates any feature with wavelength smaller or equal to λ_c, where

$$r \sim \lambda_c/4. \quad (1)$$

(Adam et al., 2005.)

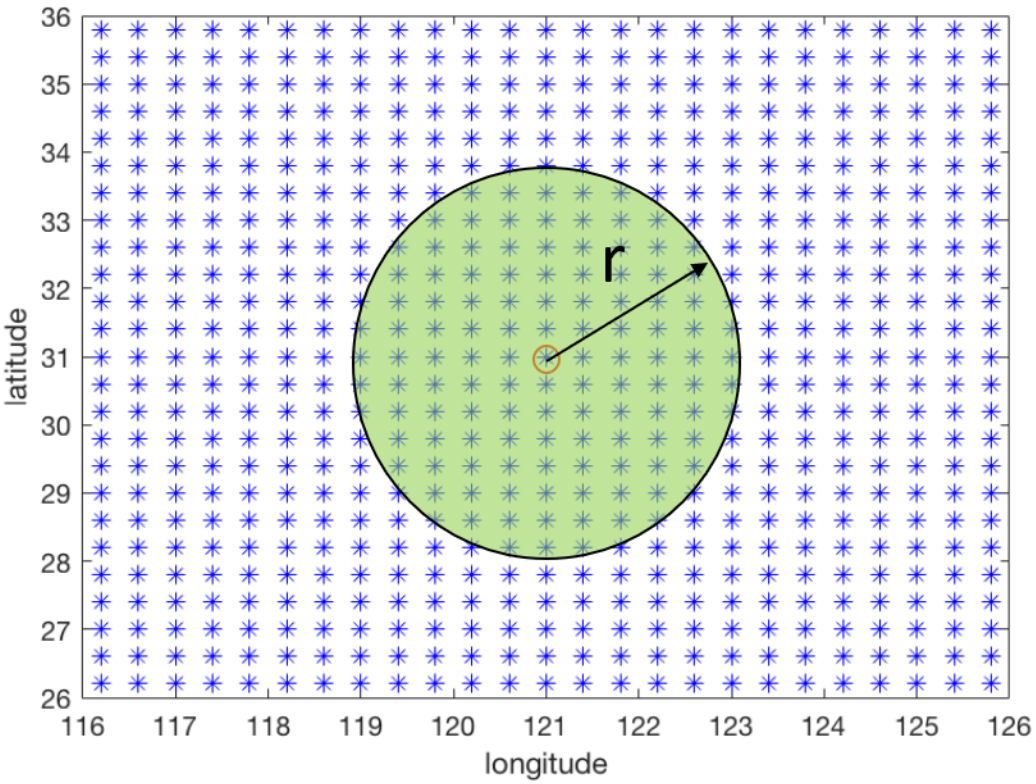

Figure 3.4. Illustration of minimizing filter, r.

The blue dots represent the grid points. The red circle is highlighting the individual point to which we apply the minimizing filter with the r radius. The green area represents the region in which the grid points are within a distance r from the individual point highlighted by the red circle.

3.3.2. Median filtering

In the filtering stage, we apply a median filter to the minimized depth anomaly grid in order to smooth it out by removing any remaining small-scale depth anomalies (Adam et al., 2005). The method is relatively similar to the one previously described: for each of the points of the depth anomaly grid, i.e., for each latitude and longitude (the red circle in Figure 4 represents an example of one point of the grid), we sweep a region of radius R (like the green circle in Figure 4, but the radius will be R instead of r). This time however, the value imposed at the

center of the green circle is the median value of the points encompassed in this green circle. The stage removes any topographic anomaly with a wavelength smaller or equal to λ, where

$$R \geq \sqrt{2}\lambda. \quad (2)$$

(Wessel, 1998).

The minimizing and median filters have been applied with the Generic Mapping Tool (GMT) software from Wessel and Smith (1991). In order to enhance the accuracy of our characterization of the Louisville swell, we varied the radii of the minimizing (r) and median filters (R). If r is too small, part of the swell and volcanoes will still remain combined together. If the r is too large, then the filter will remove the entire swell along with some topography from the volcanoes. If the R is too small, not all of the swell topography will be separated from the volcanoes, and the swell will be overestimated. If R is too large, the swell will be underestimated. These issues, as well as the values considered for the minimizing and median filters are discussed in more details in section 4.1 Swell determination. Figure 3.5 illustrates the separation of the volcanic and swell fluxes of the profile, indicated by the black line, along the Walvis volcanic chain after Adam et al. (2007).

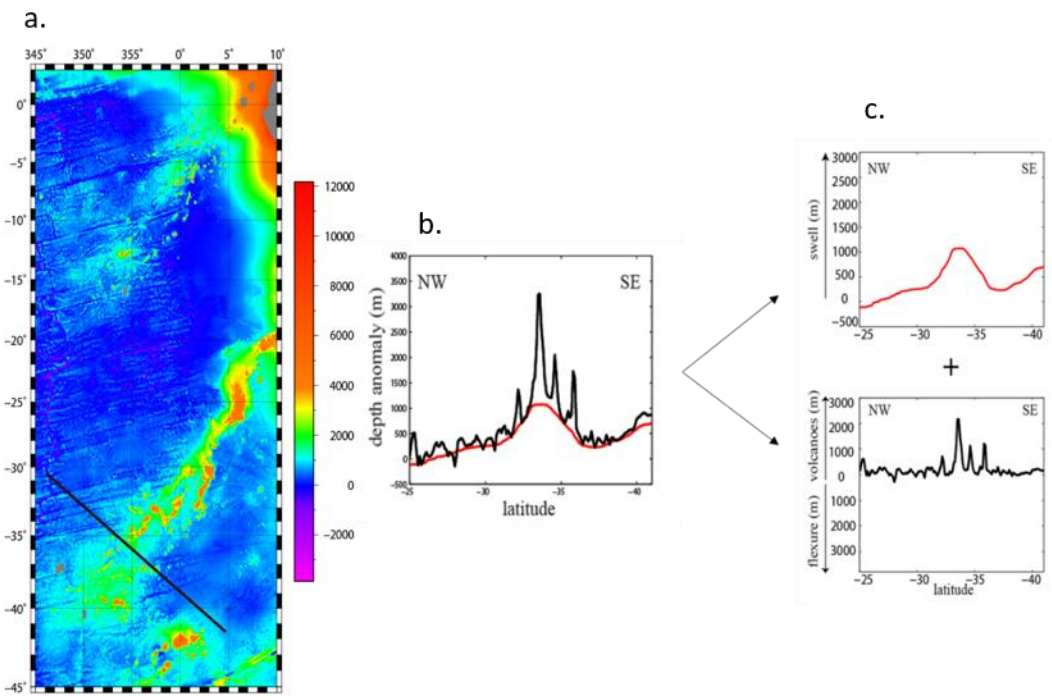

Figure 3.5. The separation of the volcanoes and swell along the Walvis chain.
(a). Bathymetry and emplacement of the profiles along which we studied the depth anomaly. (b). Depth anomaly (black line) and swell (red line) are found by filtering the depth anomaly with the MiFil filter. (c). Swell (red line) and volcanoes (black line) components, separated through the MiFil method. Figure is modified from Adam et al. (2007).

3.4. Sliding Box

This study's main outputs are volcanism and swell fluxes as a function of the volcanism age. To compute the volcanism and swell fluxes, we compute the volume contributions from the swell and volcanoes encompassed in the box represented in Figure 3.6.

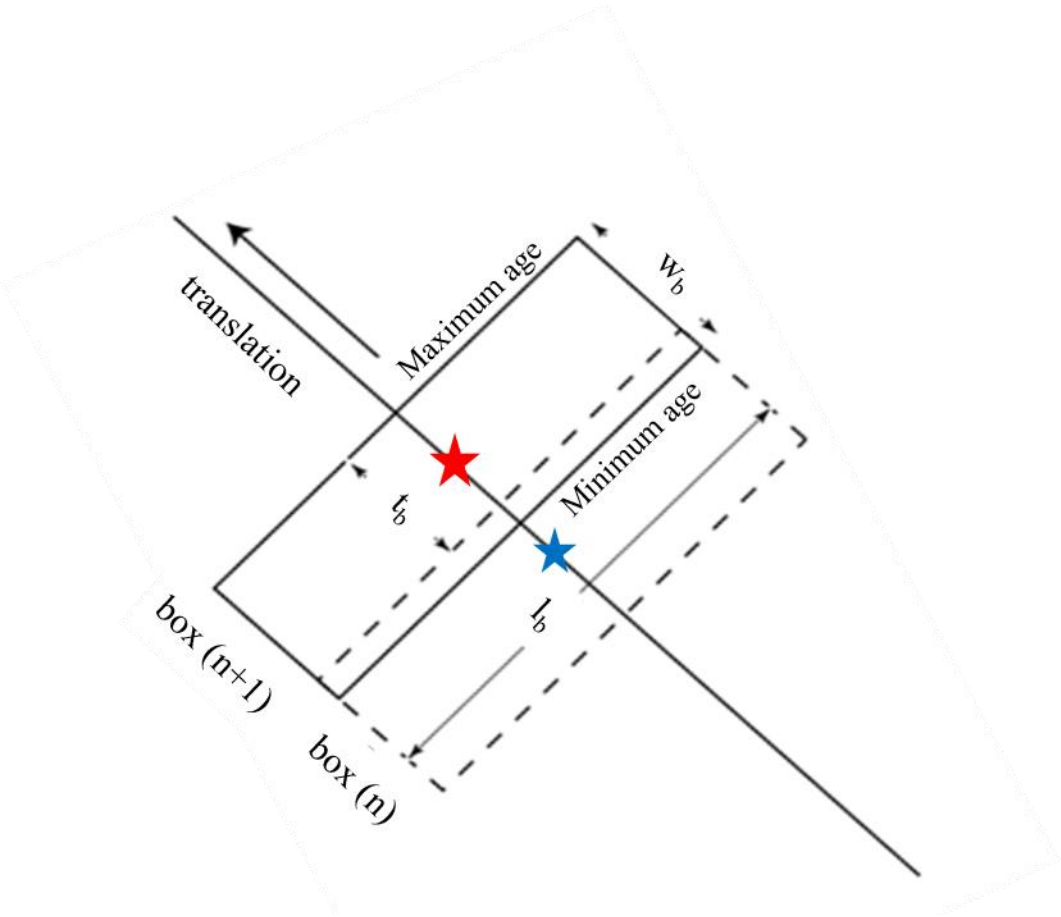

Figure 3.6. The parameters of the translating box.

The parameters of the sliding box are width (w_b), length (l_b), and the translation step (t_b). The dashed lines illustrate the box at the translation step t_n, the center of which is shown by the blue star. The box defined by the solid black lines is the translation box at step t_{n+1}, the center of which is shown by the red star. The distance between the red and blue stars is t_b, the translation step. Maximum ages are found at the far-left side of the box while the maximum ages are found to the right of each box. Figure is modified from Vidal and Bonneville (2004).

This box was created perpendicular to the hotspots main axis and has a width, w_b, and a length, l_b. The center of the box is located along the main axis, which we defined in section 2.1. For each iteration step, i.e., for each point along the main axis, the volume of the swell is the

volume comprised between the surface defined by the swell (red line on Figure 3.7a) and the reference depth anomaly (depth anomaly = 0, hachured red region on Figure 3.7b).

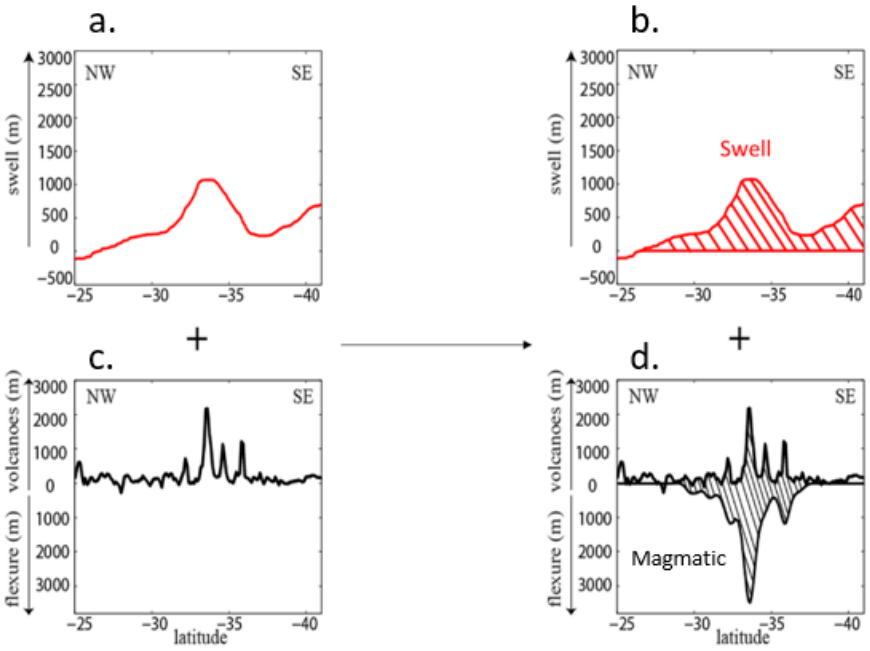

Figure 3.7. Computing magmatic and swell volumes.
(a & c) The separated swell (red) and volcanic edifice (black). (b &d) Volumes used to calculate the swell flux is illustrated by the red hachured region and the volume used to calculate the magmatic flux is illustrated by the black hachured region. Figure is modified from Adam et al. (2007).

To compute the volume of the volcanic edifices and compensation root, we had to consider that the lithosphere has a finite strength, and therefore flexes downwards when loaded by magmatic products (Watts et al., 1975; 1980). The flexure beneath the volcanic chain has been pointed out by studies based on gravity (Zucca and Hill, 1980; Zucca et al., 1982; Watts et al., 1985; Hill and Zucca, 1987; Adam and Bonneville, 2008) and seismic data (Watts et al., 1985; Lindwall, 1988; Watts and ten Brink, 1989). In particular, seismic reflectors show the morphology of the flexure beneath volcanoes (Watts et al., 1985; Lindwall, 1988; Watts and ten

Brink, 1989), (Figure 3.8). The volcanic material is emplaced over the pre-existing oceanic crust (Figure 12). At the beginning, the oceanic crust is not flexed. After a period of 1 m.y., when most of the volcanic material has been emplaced, the lithosphere will then flexure, in response to the weight of the volcano (McNutt, 1980). Ignoring the volume of volcanic material encompassed in the flexural root would lead to underestimating the volume of erupted volcanic material (Smith and Wessel, 1990; White, 1993; Vidal and Bonneville, 2004; Adam et al, 2007).

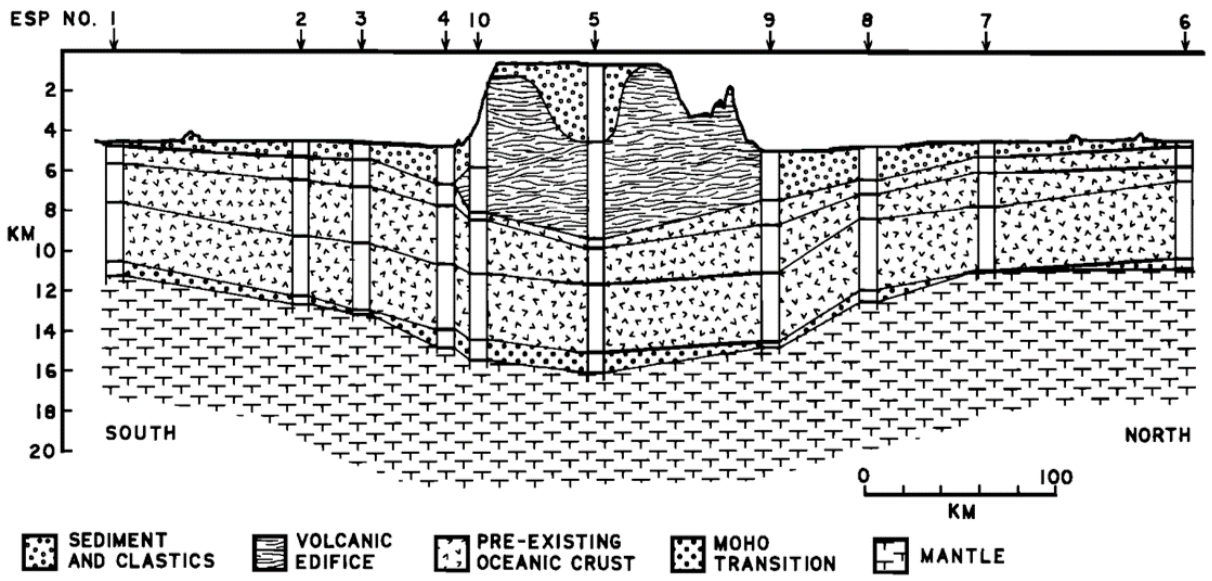

Figure 3.8. North-south cross section through the Hawaiian chain, near Oah.
The structure of the crust has been obtained by integrating seismic refraction data. Each of the solid lines corresponds to a seismic reflector. The different layers of rocks are identified with the legend in the image. Figure is from Lindwall et al. (1988).

Although the existence of the compensation root is generally agreed upon, the models of compensation (regional compensation vs. local or 'Airy' compensation) are still debated. We know that the simple Airy compensation is not the actual compensation mechanism for the hotspot chains (Watts and ten Brink, 1989), and a regional compensation by an elastic plate must

be invoked (Watts and tenBrink, 1989). In the results section, we investigated the influence of the compensation mechanism on the flexure and fluxes computation.

Once the flexure is computed, we can then compute the volume of magmatic material. This volume is comprised between the surface defined by the volcanoes (blackline on Figure 3.7b) and the reference flexure (hachured black region on Figure 3.7b). To calculate the volume in this hachured region, we use the 'volume' function in MatLab which computes the volume between two surfaces (i.e., swell and magmatic hachured region in Figure 3.7b) in 3D (Adam et al. 2007).

The volumes of swell and volcanoes encompassed in the sliding box are computed at each point of the main axis. The corresponding volcanism age is the volcanism age at the center of the sliding box. We will vary the parameters of the box, such as width (w_b), and the length (l_b), in order to make sure that their choice does not influence the final result. The box is translated along the main axis, in order to compute these volumes all along the Louisville chain. The influence of the translation step (t_b) will also be discussed. In particular, we will discuss the overlap of the sliding boxes.

To obtain the swell and magmatic fluxes, we divide the volume of the swell and magmatic material contained in the sliding box by Δt. Δt is the difference between the maximum and minimum volcanic ages that are found in the sliding box along the main axis, for each iteration. For example, if the swell volume encompassed in the sliding box is 300 km^3, and Δt = 1 Ma, the swell flux, Q_s, will be 0.0095 m^3/s (300 x 10^9/(1 x 10^6*365*24*3600 = 0.0095). The volume of swell is generally reported as the buoyancy flux, *B*, (Sleep, 1990), with

$$B = (\rho_m - \rho_w)Q_s \quad (3)$$

where ρ_m and ρ_w are the densities of the mantle and the seawater (ρ_m = 3300 kg m^{-3}, ρ_w= 1000 kg m^{-3}). In the result section, we will report these fluxes as a function of the volcanism age.

Chapter 4 - Results

This section will cover which filter was determined to be the best fit for all three sections of the Louisville chain and how we came to that decision. It will also explain which parameters for the sliding box have been chosen and how they affect the calculated fluxes. Lastly, it will include the calculated swell and volcanism fluxes.

4.1. Swell Determination

As stated previously, we have to remove the contribution of the volcanic edifices from the calculated depth anomaly by using the MiFil filtering method (Adam et al., 2007). For brevity, we will refer to this in future as the influence of the swell and magmatic components. In this section, we discuss the influence of the radius of the minimizing and median filters on the determination of the swell.

4.1.1. Segment 1

Segment 1, defined in the *Methods* section in Figure 3.1, of the Louisville chain is located near the mid-oceanic ridge and contains the youngest volcanoes. The youngest volcano has a 1.11 ± 0.4 Ma age and is located at latitude 50.4^{o}S, 220.9^{o}E (Koppers et al. 2011). This segment extends to latitude 44.6^{o}S, and longitude 199.9^{o}E (Koppers et al., 2004; 2011). As this segment of the volcanic chain is associated with the most recent volcanism, we expect the swell to be maximal (Vidal and Bonneville, 2004).

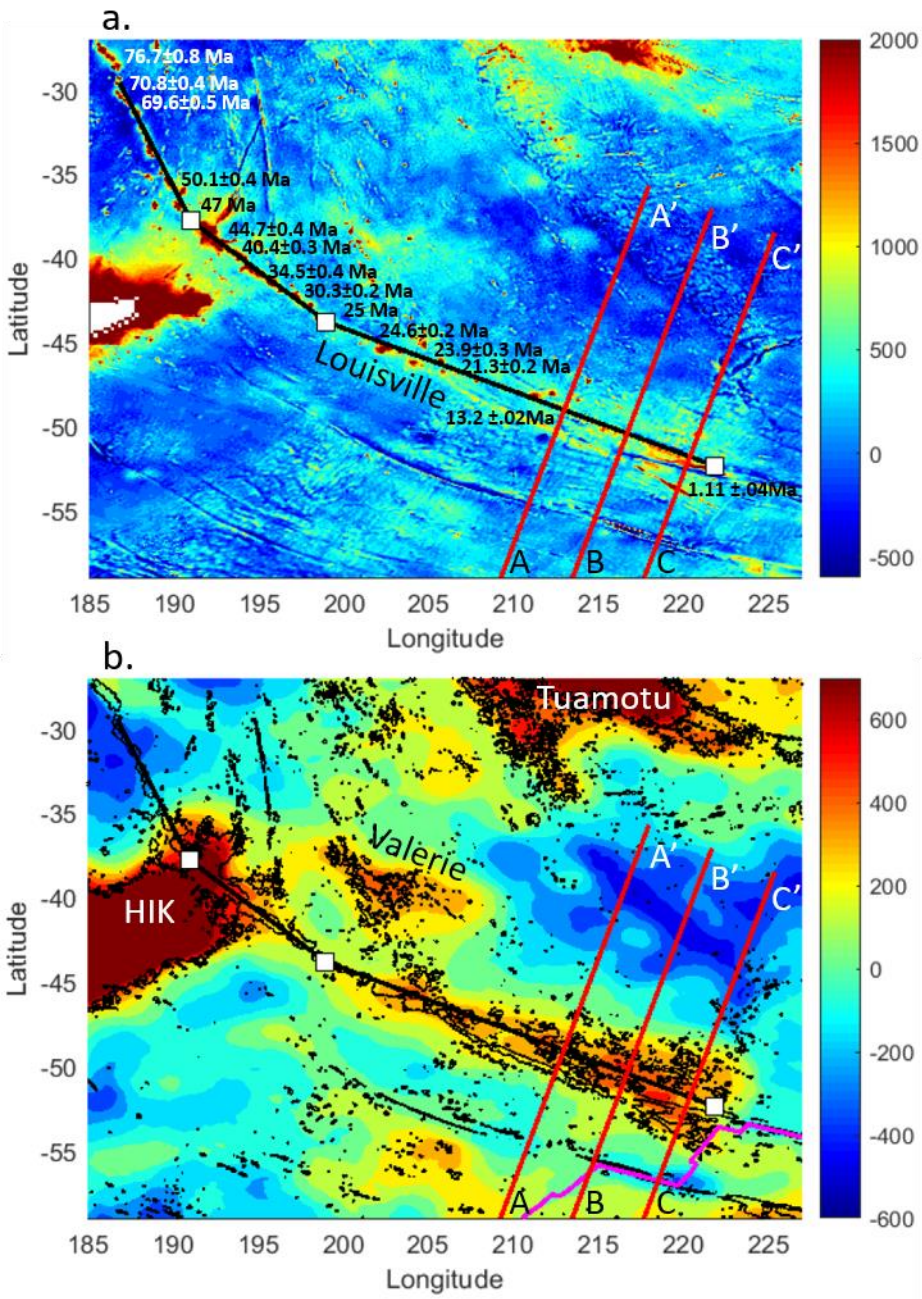

Figure 4.1. Depth anomaly (a) and swell (b) along the Louisville chain.

The black line represents the main axis, and the red lines are trajectories perpendicular to the main axis for the first segment. The Mid-Oceanic Ridge (MOR) is reported in magenta. The dark area around latitudes 40-45°S and longitudes 185-195°E is the Hikurangi (HIK) plateau (Ito and van Keken, 2007). The features around latitude 40°S and longitudes 200°E is the Valerie seamounts (Clouard and Bonneville, 2005). The volcanism ages, taken from Koppers et al. (2004; 2011), are reported in black and white text in panel a.

The depth anomaly and the swell are displayed in Figure 4.1. The swell is a low pass filter of the depth anomaly. By filtering the depth anomaly, we remove the short-wavelength features (such as fracture zones and individual volcanoes), which allows better observation of the long wavelength depth anomalies, such as the swell. The swell has been computed using a minimizing filter of radius 20 km, and a median filter radius of 250 km. Several positive and negative depth anomalies can be observed in the depth anomaly and swell maps (Figure 4.1).

The positive depth anomalies reported in red in Figure 4.1 are mainly located along the youngest part of the Louisville chain, along segment 1, between longitudes 207° to 222°E. This swell is probably formed by the interaction of a hotspot and the drifting oceanic lithosphere above. The largest depth anomaly of the swell is located from latitudes 48° to 52°S and longitudes 213° to 219°E, illustrated by the reds on Figure 4.1. The corresponding volcanism ages found in this area are between 13±0.2 and 1.11±0.4 Ma. Other positive anomalies are observed along the Hikurangi (HIK) plateau (Ito and van Keken, 2007), the Valerie seamounts and the Tuamotu chain (Clouard and Bonneville, 2005). These separate swells will not be considered in our calculation of the swell and magmatic fluxes.

As stated in the *Methods* section, a minimizing filter of radius r will remove the features of wavelength λ_m or lower, with $\lambda_m \sim 4r$. A median filter of radius R will remove the features of wavelength λ_M or lower, with $\lambda_M \leq R/\sqrt{2}$ (Wessel, 1998). The wavelength we try to remove is the spacing of the volcanoes. Along the Louisville chain, the volcanoes have a spacing varying between 100 and 200 km (Figures 4.1 and 4.2). In theory, the corresponding r should then vary between 25 and 50 km, and R between 140 and 280 km. However, as stated in Adam et al. (2007), if the value chosen for r is too large, the signature from fracture zones would be

exaggerated and the swell underestimated. In order to study the influence of r and R on the swell computation, we considered several values of r and R, chosen by considering the theoretical range discussed here. More precisely, we consider values for r = 10, 20, and 30 km, and R = 150, 250, and 350 km.

The influence of varying r is shown in Figure 4.2, a plot that compares the depth anomaly and the filtered depth anomalies along the three profiles located in Figure 4.1. The three profiles (red lines in Figure 4.2) were chosen because they are located in the area where a majority of the swell is found. Profiles AA' and CC' intersect volcanoes along the main axis, while the BB' profile is not. The volcanoes along profiles AA' and CC' are identified by the black arrows.

Following the MiFil method, we first tested the minimizing filters along these profiles. We kept the median filter (R) constant at 250 km and varied the minimizing filter (r) at 10, 20, and 30 km. Figure 4.2 illustrates the effects of these filters along the profiles. In this figure, the blue line represents r = 10 km, the red line is r = 20 km, and the green line illustrates r = 30 km.

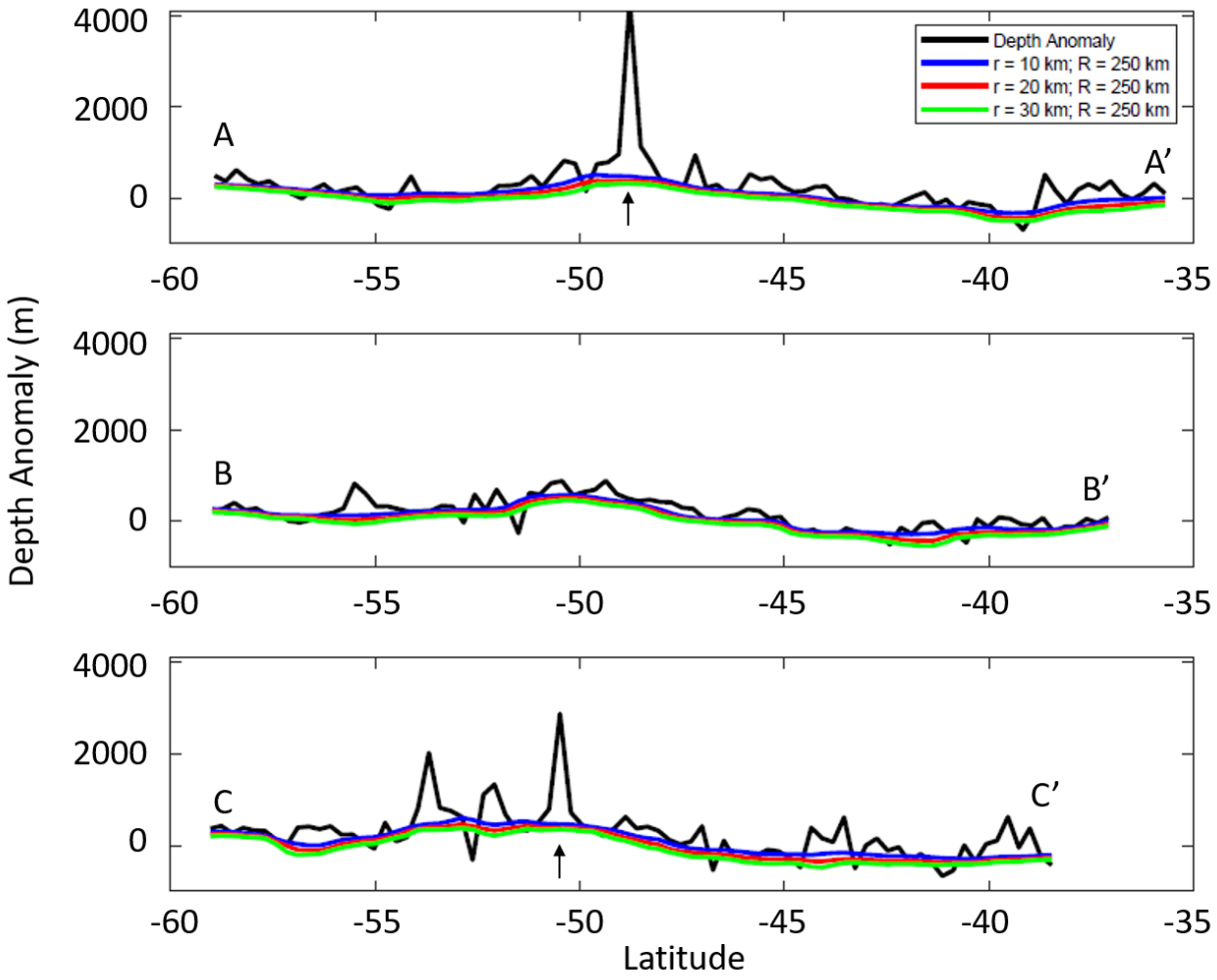

Figure 4.2. Influence of the minimizing filter radius on the swell calculation for the first segment.

The black line represents the depth anomaly along the AA', BB', and CC' profiles, shown in Figure 4.1. The black arrows represent individual volcanoes the profiles intersect. The color lines represent the filtered depth anomaly. The radius of the median filter is constant at R = 250 km. The radius of the minimizing filter is fixed at 10, 20, and 30 km (color code in the legend).

At a first glance, figure 4.2 shows that that the minimizing filters make little differences in the filtered depth anomaly for all three profiles. Since the filters along profiles AA', BB', and CC' are hard to distinguish from one another, we magnified the y-axis of these profiles from a

depth anomaly value of -500 to 1000 m. This is illustrated in Figure 4.3. Figure 4.2 is useful, as it illustrates that our filters provide a good general, basic approximation of the swell.

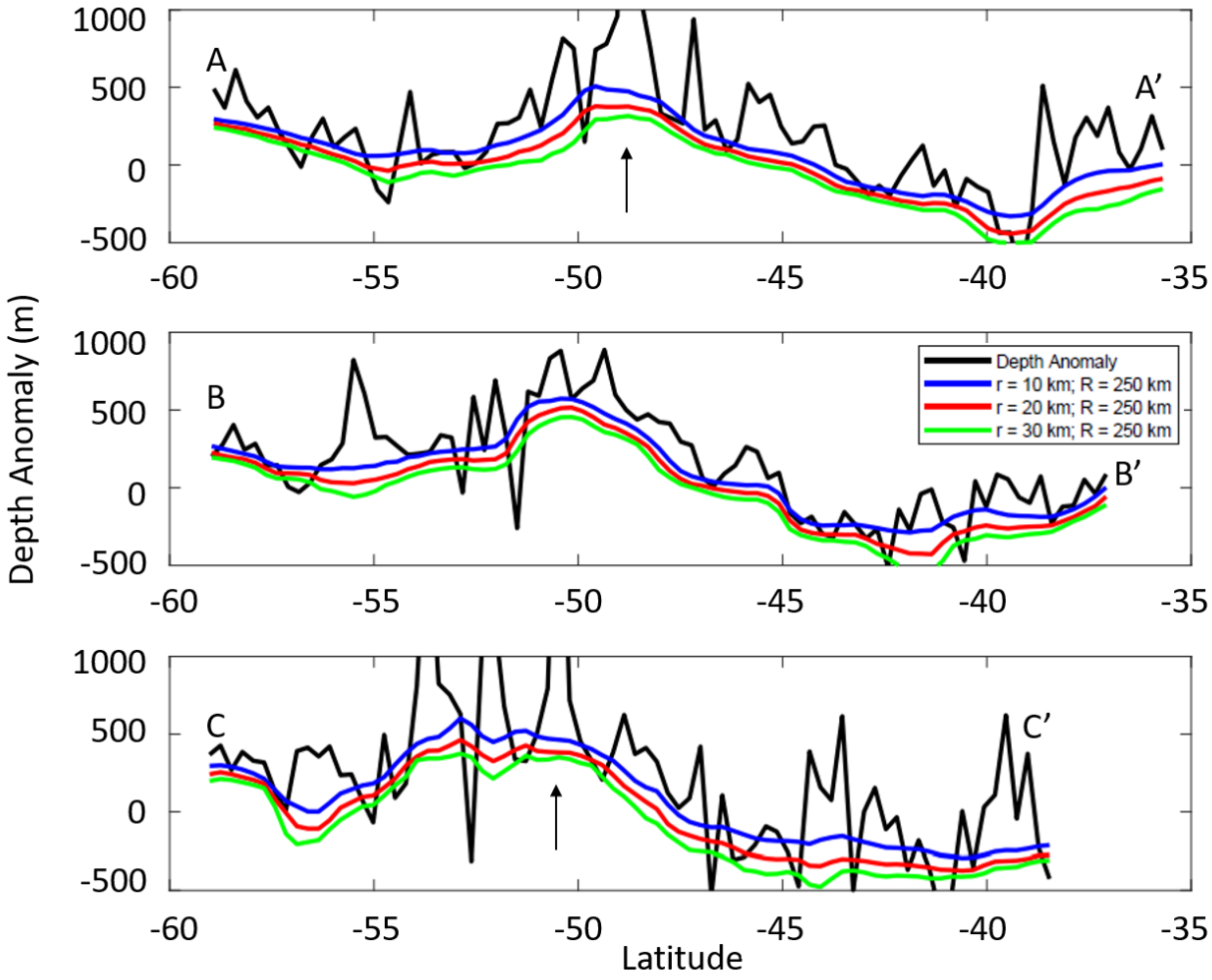

Figure 4.3. Magnification on the profiles displayed in Figure 4.2. to study the influence of the minimizing filter radius on the swell calculation.

The color schemes are the same from Figure 4.2. The black arrows represent individual volcanoes the profiles intersect. The profiles along AA', BB', and CC' focus on a more limited depth range of -500 to 1000 m to be able to identify any differences between the minimizing filters.

The filters have a similar shape and wavelength across all three profiles but departures from each other can be noticed. We saw that by increasing the minimizing radius, r, we decrease

the value of the swell (i.e., removing more topography associated with volcanoes). This means that r = 10 km (blue line) removes the largest amount of topography while r = 30 km (green line) removes the least, with r = 20 km (red line) removing an average of the two.

Looking at profile AA' from latitude 47^{o} to 50^{o}S, at profile BB' from latitude 45^{o} to 50^{o}S, and profile CC' from latitude 47^{o} to 55^{o}S, we identify the areas where most of the swell is located for each profile. The volcanoes in profiles AA' and CC' are identified by the black arrows. In profile AA' and CC', we can see that the 10 km filter is passing through the volcanoes in this area (i.e., the blue curve is located above the base of the depth anomaly, rather than at the base). This means that the filter is removing too much of the topography because it is underestimating the volume of the volcanoes while overestimating the swell. Between latitudes 40^{o} and 43^{o}S on profile BB' the 30 km filter (green line) is too low (i.e., the green curve is located beneath the depth anomaly, rather than at the base). This is probably due to the influence of the fracture zone, located at latitude 43^{o}S. This means that the minimizing filter r = 20 km, passing at the base of the volcanoes volume, is the best fit for the youngest part of the chain since it fully separates the swell and volcano components from one another.

To test the median filter, we kept the minimizing filter constant at the chosen r = 20 km. We then varied the radius of the median filter at R = 150 km, R = 250 km, and at R = 350 km. Figure 16 illustrates the results of these tests. We see that the blue line represents R = 150 km, the red line is R = 250 km, and the green line is R = 350 km.

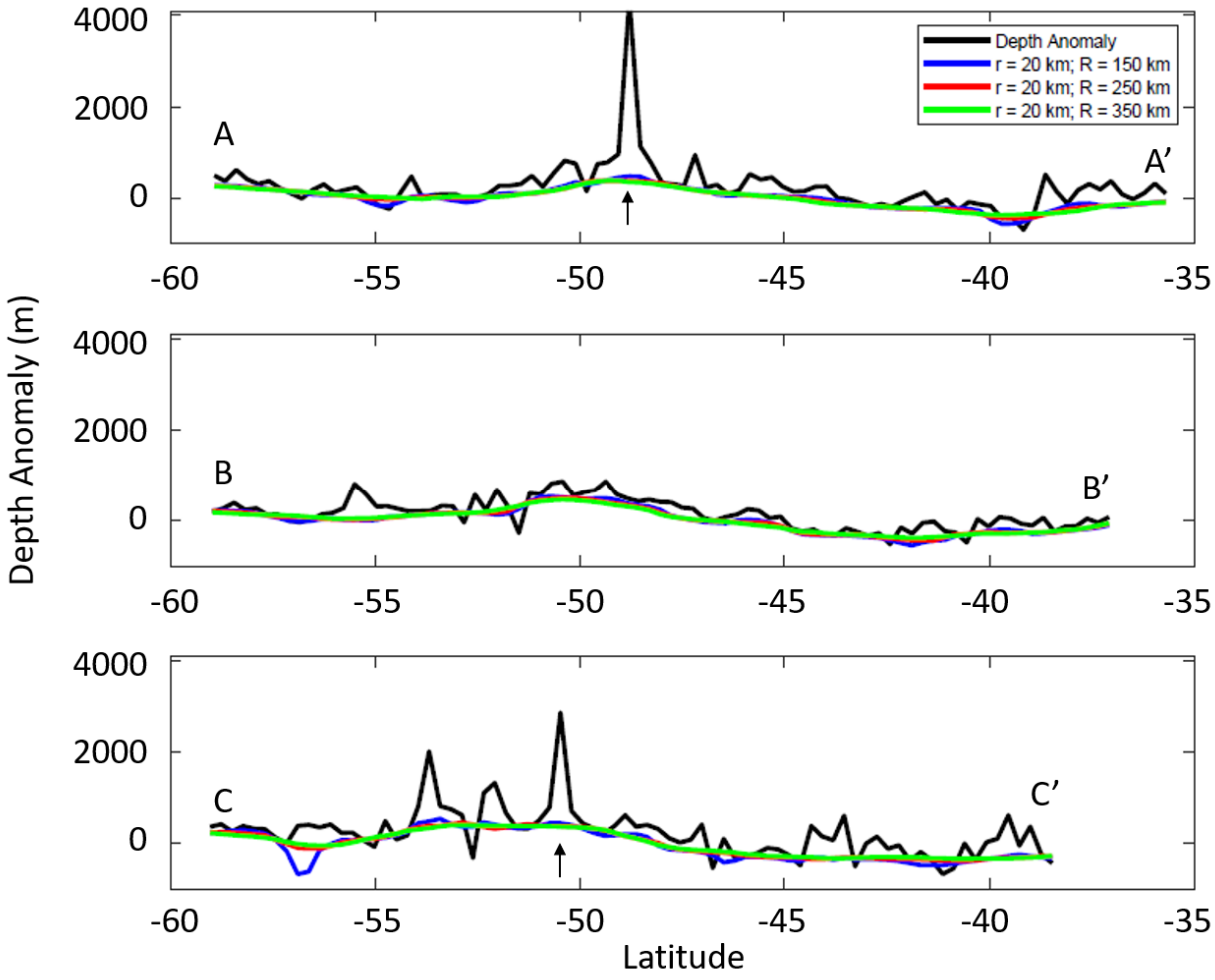

Figure 4.4. Influence of the median filter radius on the swell calculation.
The black line represents the depth anomaly along the AA', BB', and CC' profiles, shown in Figure 4.1. The black arrows represent individual volcanoes the profiles intersect. The color lines represent the filtered depth anomaly. The radius of the minimizing filter is r = 20 km. The radius of the median filter is fixed at 150, 250, and 350 km (color code in the legend). Depth anomaly is reported in meters.

Along all three profiles, the filtered depth anomaly profiles created by the three filters are indistinguishable. This is because the vertical scale is set to encompass the maximum depth anomaly found in profile AA'. Viewing the results at this scale shows whether the filters provide a good approximation of the swell. However, to better observe the differences among

the depth anomaly curves generated by the three filters along profiles AA', BB', and CC', we magnified the vertical scale so that it varies between -500 and 1000 km. These results are illustrated in Figure 17.

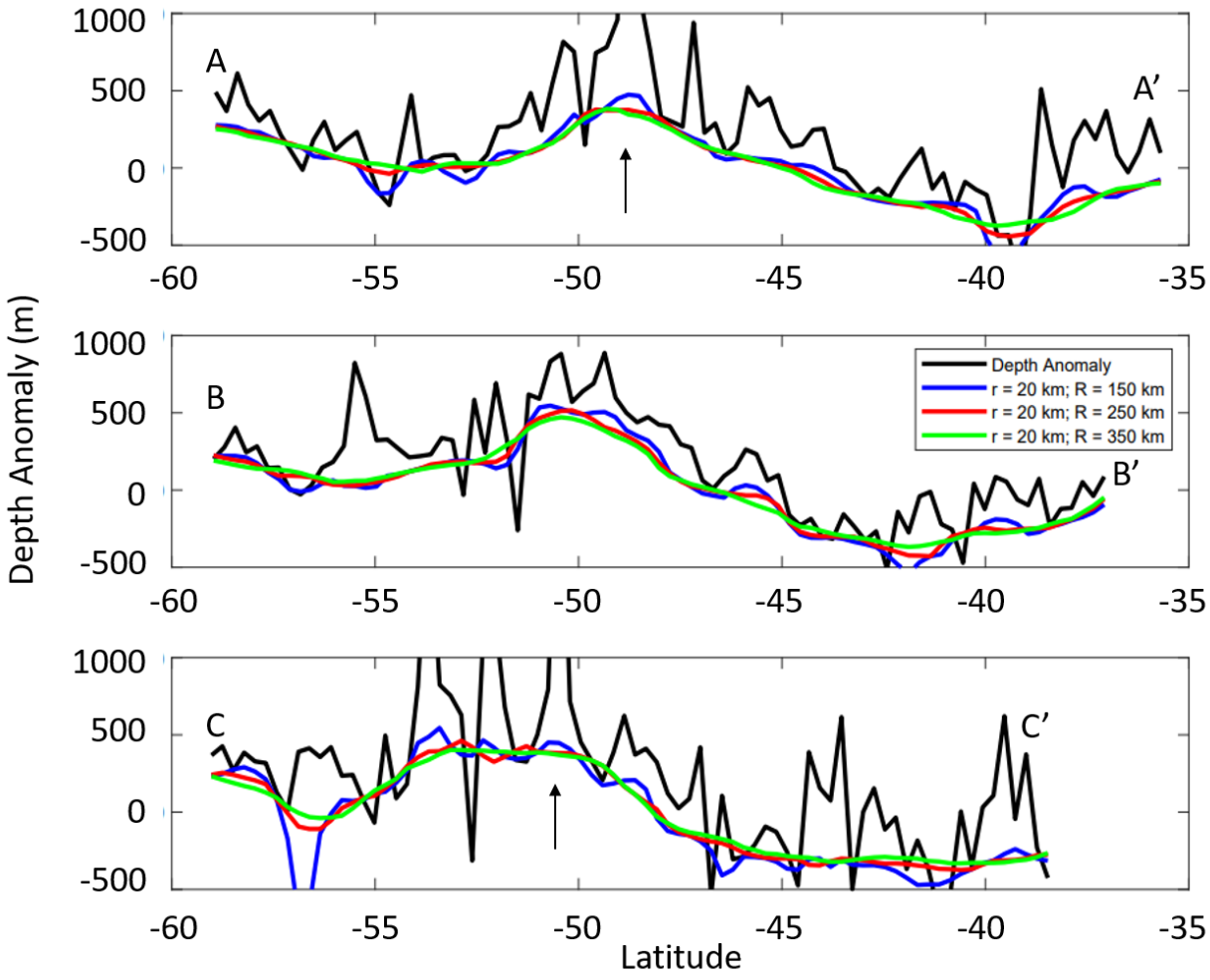

Figure 4.5. Magnification of the profiles displayed in Figure 4.4 to study the influence of the median filter radius on the swell calculation.

The color schemes are the same from Figure 4.4. The black arrows represent individual volcanoes the profiles intersect. All profiles have been magnified from -500 to 1000 m to identify any differences between the median filters.

The biggest differences among the filtered depth anomaly curves are found along the profile CC', around latitude 57°S. At this location, the curve calculated using a filter of R = 150 km drops sharply, thus providing a negative swell. The amplitude and the wavelength of the swell at this location indicate that the curve calculated using a filter of R = 150 km (blue line) is not adequate to characterize the Louisville swell. This filter also shows short wavelength variations along the three profiles that are inconsistent with the swell morphology described by previous authors (Crough 1983). We can, therefore, eliminate R = 150 km as a viable median filter for explaining the swell at this location. The curves calculated with the R = 350 km (green line) and R = 250 km (red line) filters produce similar results and cannot be distinguished unambiguously using this analysis. We, therefore, consider that results from other profiles, such as the main axis and along older segments of the chain, in order to see which median filter best characterizes the Louisville swell.

4.1.2. Segment 2

The second segment of the chain extends from latitude 44.6°S and longitude 199.9°E to latitude 37.1°S and longitude 191.0°E in between the two bends of the track (denoted by white square on Figure 4.6, from Koppers et al. 2004; 2011). The volcanism ages along this segment vary between 25 and 40 Ma (Figure 4.6a). The swell associated with Hawaii disappears for volcanic ages 20 – 30 Ma (Vidal and Bonneville, 2004). Therefore, we expect the swell to be small or non-existent along this segment of the Louisville seamount chain. Along the profile EE' (Figure 4.7b), we can see a very small swell of amplitude ~100 m. Along this profile, the main axis is located at latitude 43°S. The curve calculated by the filter r = 10 km (blue line) has already been eliminated in the previous sections. The difference between the calculated curves of the r = 20 km (red line) and r = 30 km (green line) filters is minimal. Along the profile DD'

(Figure 4.7a), there is no more swell associated with the Louisville chain. Most of the swell we see along this profile is the swell associated with the Hikurangi plateau. Along this profile, the main axis is located at latitude 40^{o}S.

In Figure 4.8, we test the influence of the median filter radius, R, for the middle segment of the Louisville chain. As the swell is not present along the DD' profile, we focus our discussion on the EE' profile. In the previous section, we eliminated curve calculated by the filter R = 150 km (blue line). The curves calculated by the R = 250 km (red line) and the R = 350 km (green line) filters produce similar results, and both provide a good approximation of the swell along this profile.

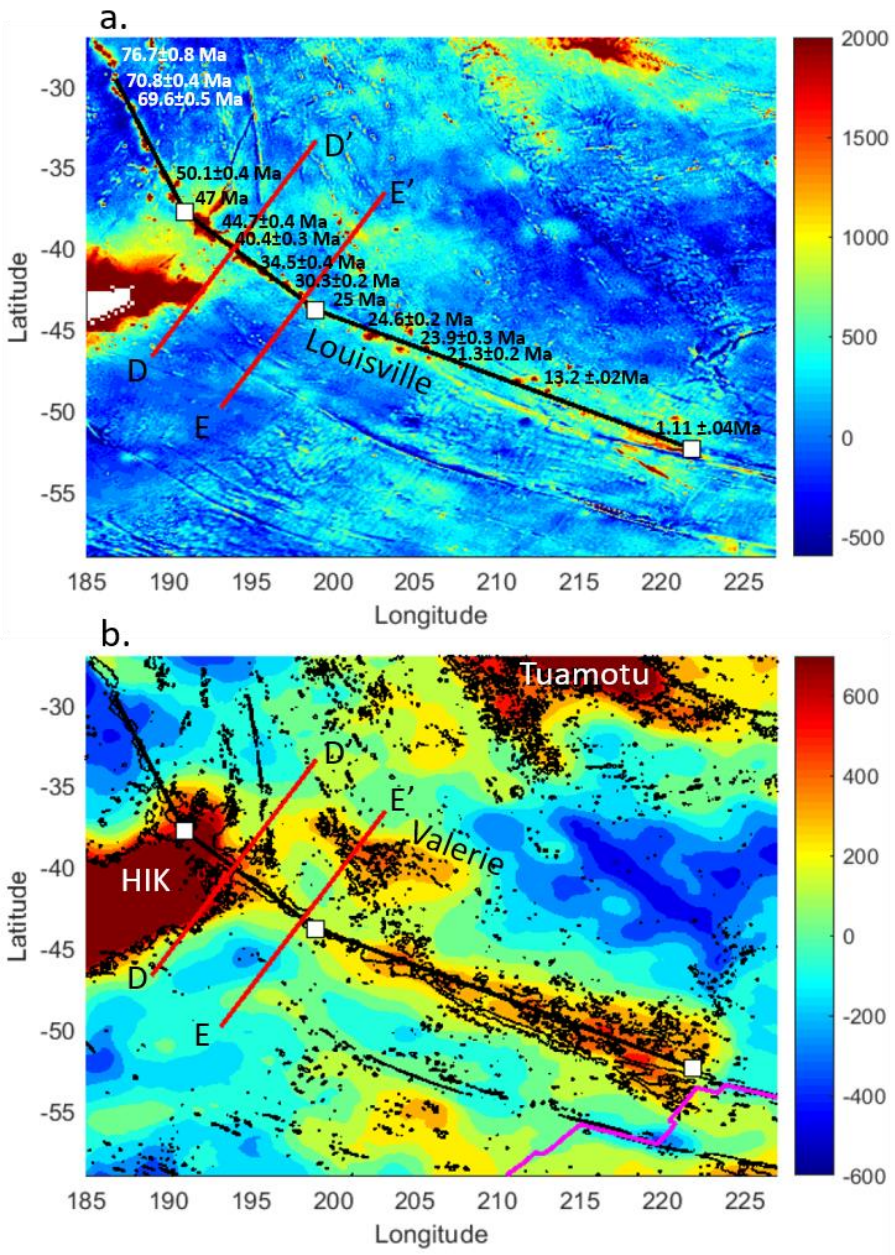

Figure 4.6. Depth anomaly (a) and swell (b) along the Louisville chain.

The black line represents the main axis, and the red lines are trajectories perpendicular to the main axis for the second segment. The Mid-Oceanic Ridge (MOR) is reported in magenta. The dark red area around latitudes 40-45°S and longitudes 185-195°E is the Hikurangi (HIK) plateau (Ito and van Keken, 2007). The feature around latitude 40°S and longitudes 200°E is the Valerie seamounts (Clouard and Bonneville, 2005). The volcanism ages, taken Koppers et al. (2004; 2011), are reported in black and white in panel a.

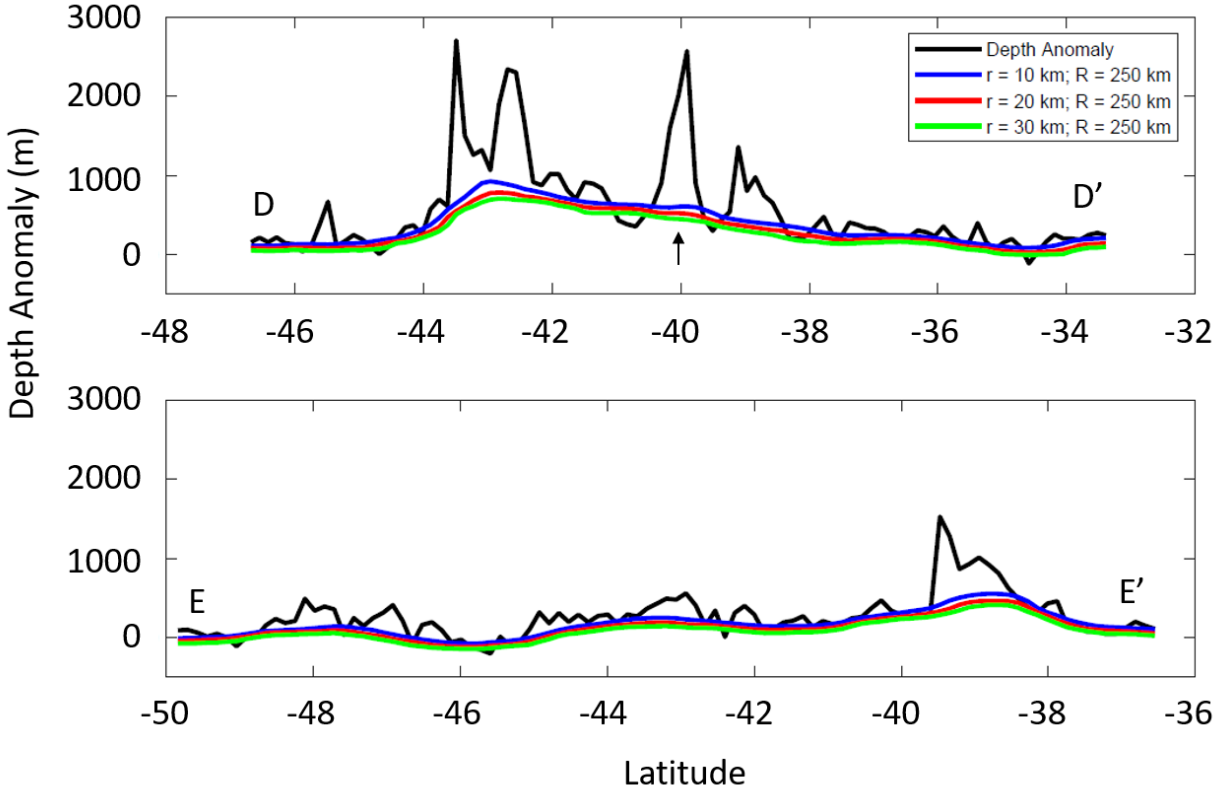

Figure 4.7. Influence of the minimizing filter radius on the swell calculation for the second segment.

The black line represents the depth anomaly along the DD' and EE' shown in Figure 4.6. The black arrow represents individual volcanoes the profile intersects. The color lines represent the filtered depth anomaly. The radius of the median filter is constant at R = 250 km. The radius of the minimizing filter is fixed at 10, 20, and 30 km (color code in the legend).

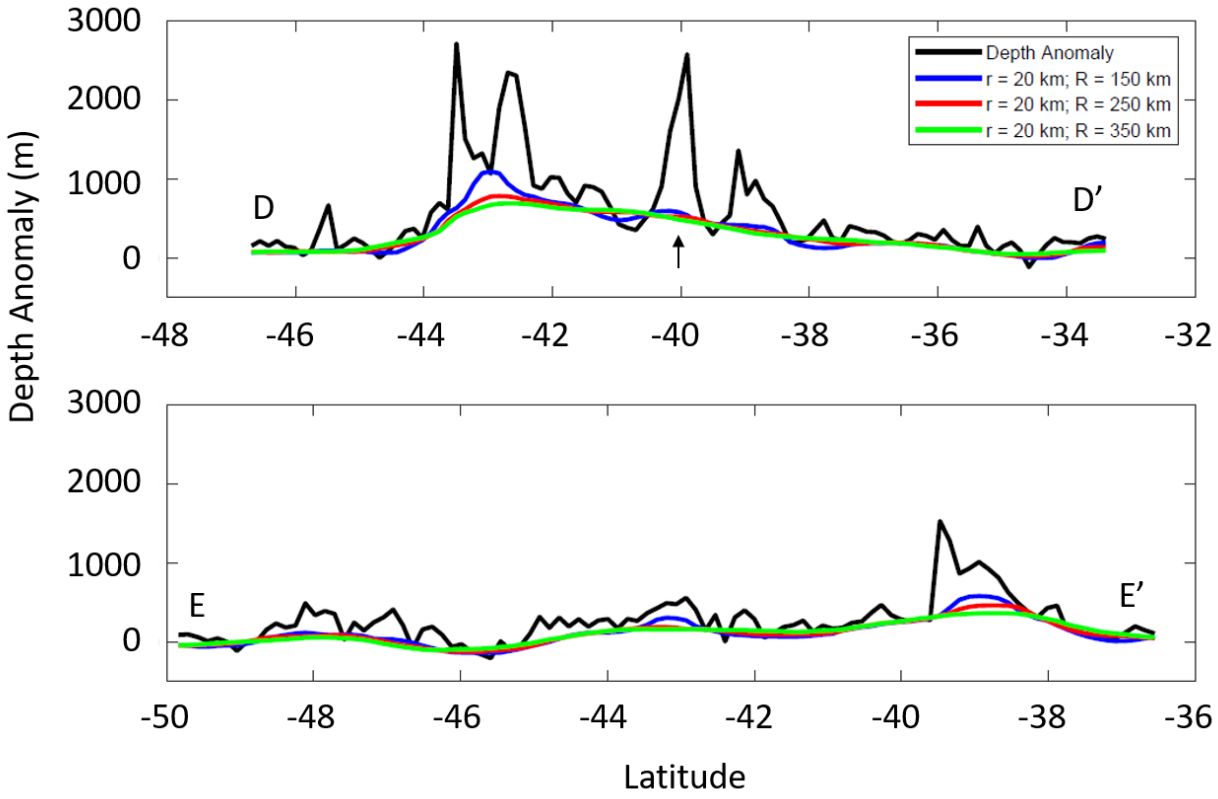

Figure 4.8. Influence of the median filter radius on the swell calculation along the second segment.

The black line represents the depth anomaly along the DD' and EE' profiles shown in Figure 4.6. The black arrow represents individual volcanoes the profile intersects. The color lines represent the filtered depth anomalies. The radius of the minimizing filter is r = 20 km. The radius of the median filter is fixed at 150, 250, and 350 km (color code in the legend).

4.1.3. Segment 3

The third segment is the oldest part of the Louisville chain. This segment extends from the bend in the track at latitude 37.1°S and longitude 191.0°E to the oldest recorded part of the chain at latitude 25.5°S and longitude 186.0°E. That location is the Osbourn seamount, which has the oldest recorded volcanic age at 78.8 ± 0.8 Ma (Koppers et al. 2004; 2011). Since this area is the oldest part of the chain, there should be no swell present in the area because the

lithosphere associated with this part of the track has migrated away from the mantle plume. We can see this in both the depth anomaly and swell map in Figure 4.9.

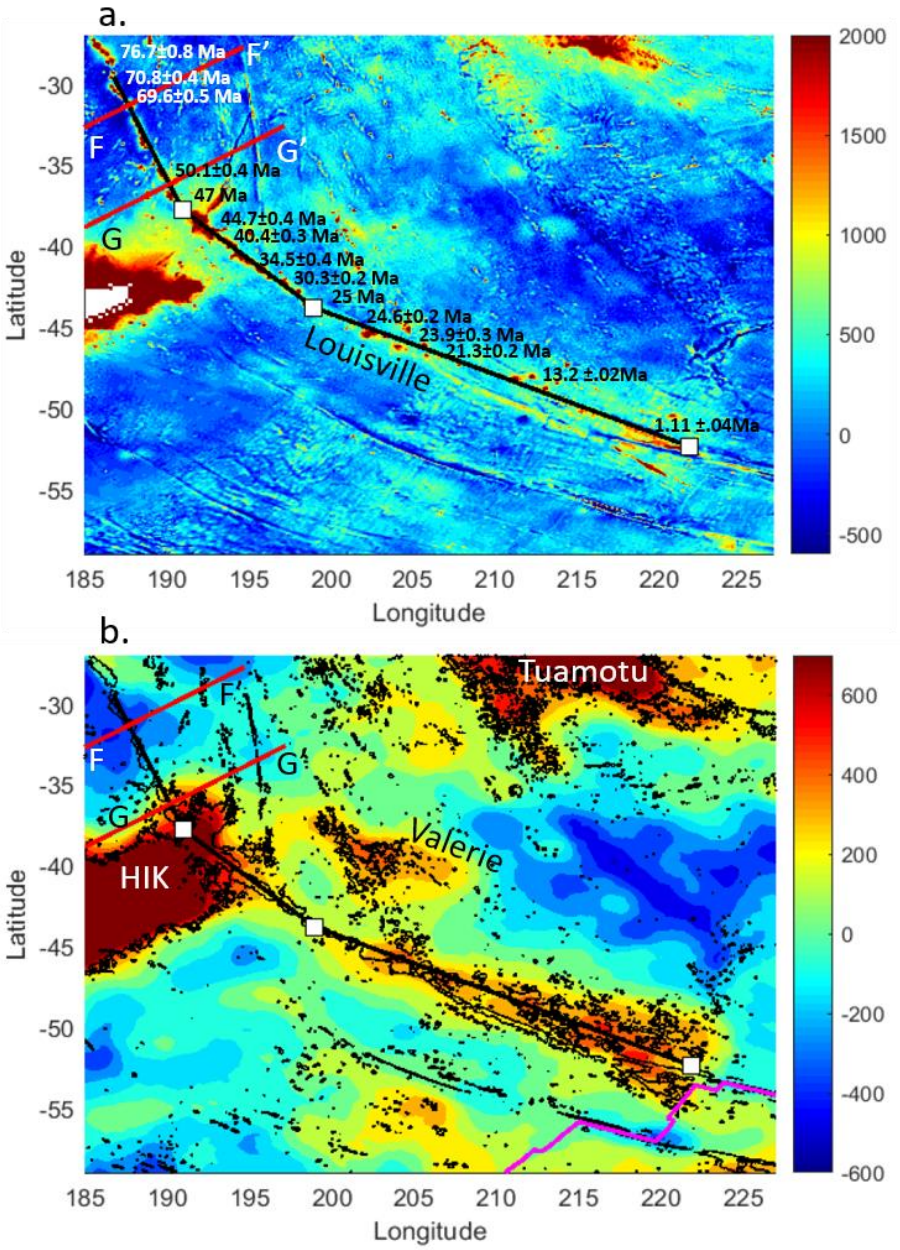

Figure 4.9. Depth anomaly (a) and swell (b) along the Louisville chain.
The black line represents the main axis, and the red lines are trajectories perpendicular to the main axis for the third segment. The Mid-Oceanic Ridge (MOR) is demarcated by a magenta line. The dark red area around latitudes 40-45°S and longitudes 185-195°E is the Hikurangi (HIK) plateau (Ito and van Keken, 2007). The feature around latitude 40°S and longitudes 200°E

are the Valerie seamounts (Clouard and Bonneville, 2005). The volcanism ages, from Koppers et al. (2004; 2011), are reported in black and white in text panel a.

In Figures 4.10 and 4.11, we can see that there is no swell associated with this part of the chain. Along the FF' and GG' profiles, the main axis is located at latitude 32°S and 37°S respectively. The swell observed along the GG' profile is associated with the Hikurangi plateau. All of our filters indicate a lack of swell along this part of the chain. This agrees with previous studies on swells, which are, in general, not found along the older parts of hotspot chains (see discussion in section 2.1, *Background Information*). The calculated depth anomaly profiles are indistinguishable along this part of the chain, regardless of filter parameters chosen.

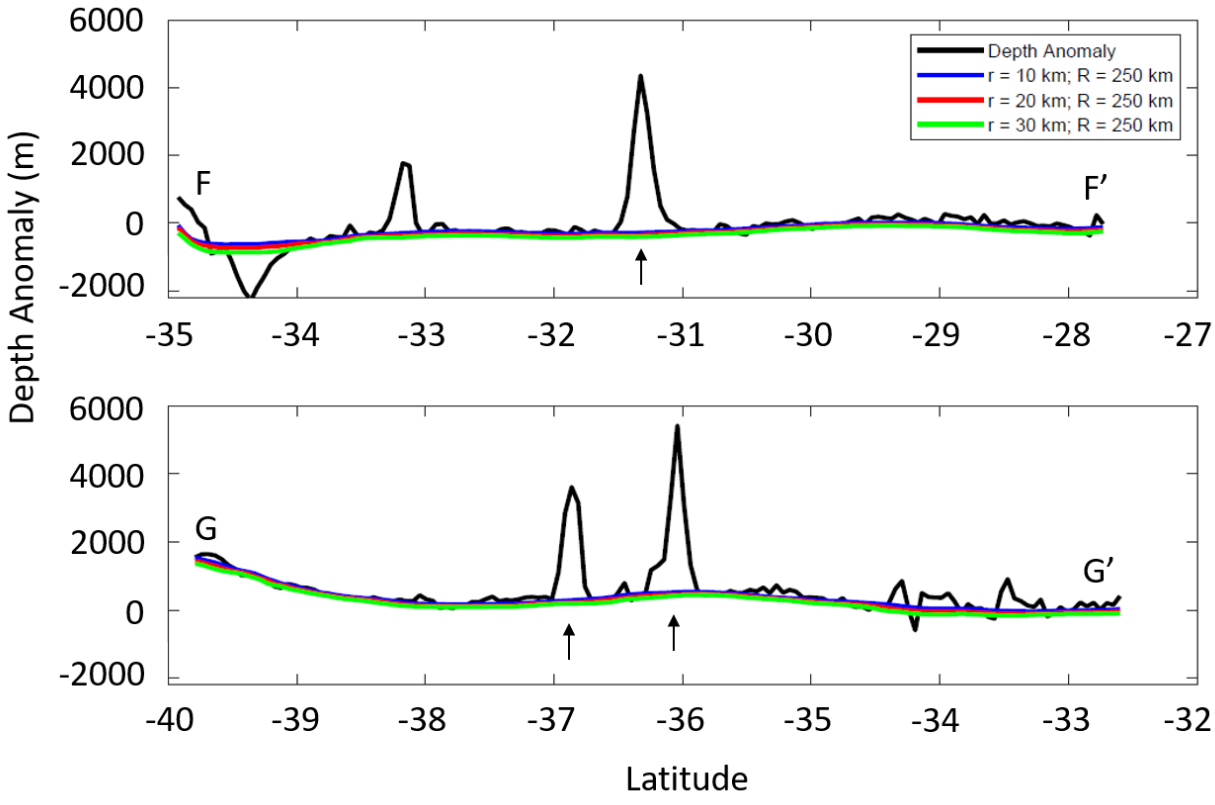

Figure 4.10. Influence of the minimizing filter radius on the swell calculation for the third segment.

The black line represents the depth anomaly along the FF' and GG' profiles, shown in Figure 4.9. The black arrows represent individual volcanoes the profiles intersect. The black colored line represents the depth anomaly. The radius of the median filter is constant at R = 250 km. The radius of the minimizing filter is fixed at 10, 20, and 30 km (color code in the legend).

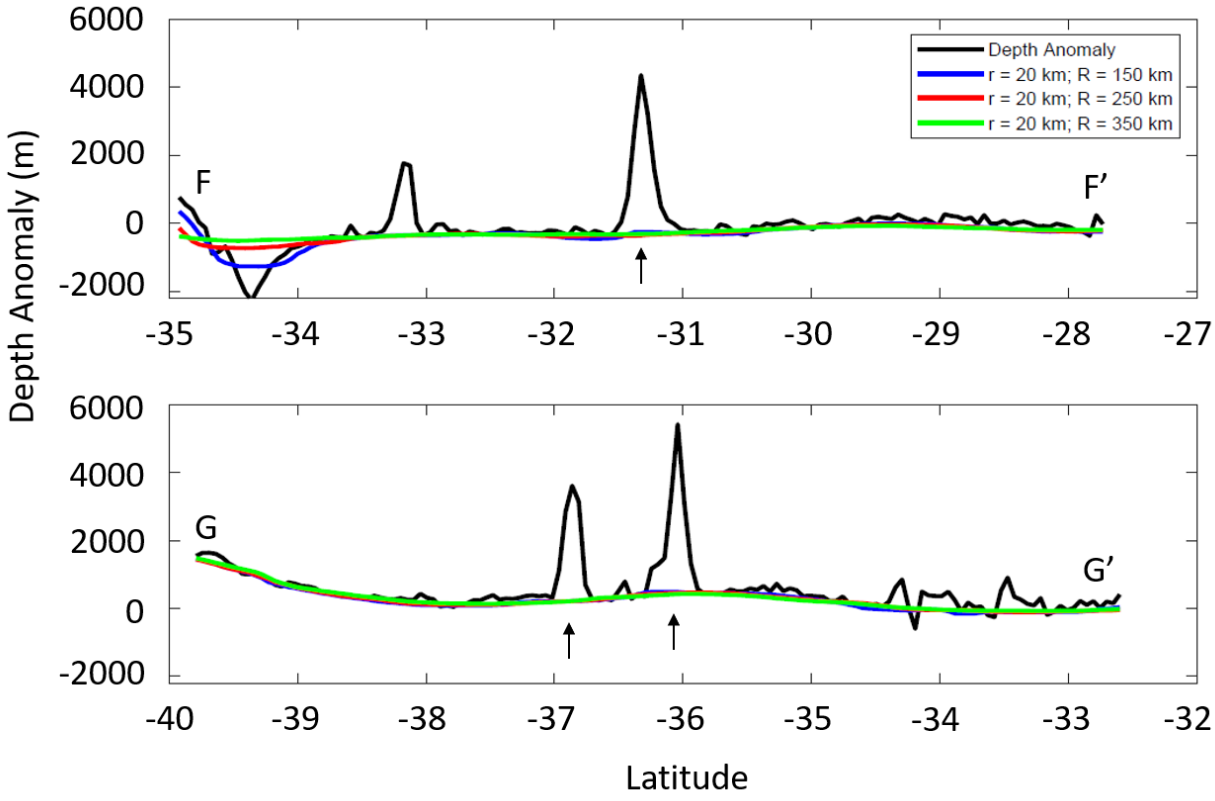

Figure 4.11. Influence of the median filter radius on the swell calculation of the third segment.

The black line represents the depth anomaly along the FF' and GG' profiles, shown in Figure 4.9. The black arrows represent individual volcanoes the profiles intersect. The color lines represent the filtered depth anomaly. The radius of the minimizing filter is r = 20 km. The radius of the median filter is fixed at 150, 250, and 350 km (color code in the legend).

4.1.4. Swell along the main axis

In this section, we investigate the impact of different filter parameters on calculated depth anomaly curves along the main axis of the Louisville chain. Figures 4.12 and 4.13 illustrates the effects of the minimizing filters r = 10, 20, and 30 km along the entire track while the median filter remains constant at 250 km.

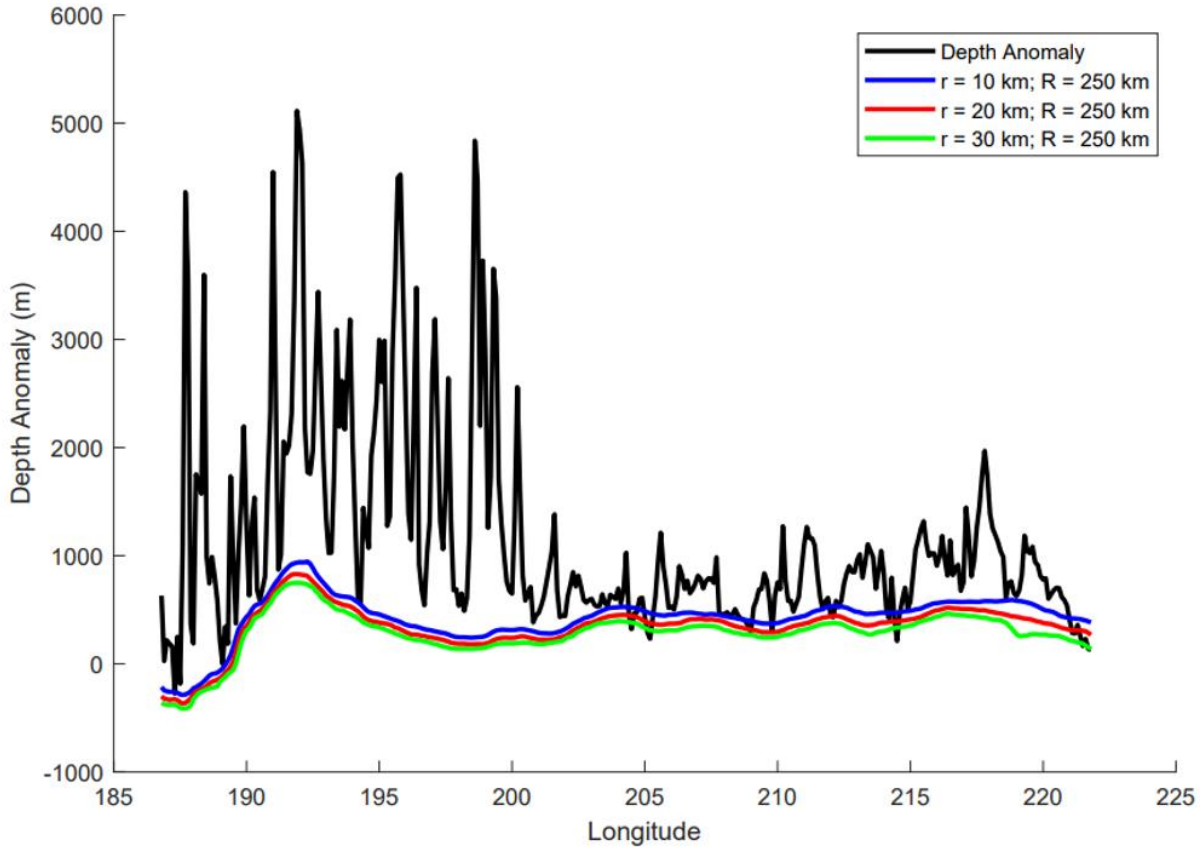

Figure 4.12. Influence of the minimizing filter radius along the main axis.
The color scheme is reported in the legend.

The oldest part of the Louisville chain, from 191.0°E to 186.0°E has no associated swell. The swell observed west of longitude 200°E is associated with the Hikurangi plateau, the boundaries of which are from 195°E to 190°E. The large variations in the depth anomaly from

190° to 185° could still be caused by the HIK plateau or interference from the Valarie seamount chain. Figure 4.12 shows the swell along the whole Louisville chain, while Figure 4.13 focuses on youngest part of the chain, where the swell associated with Louisville is present.

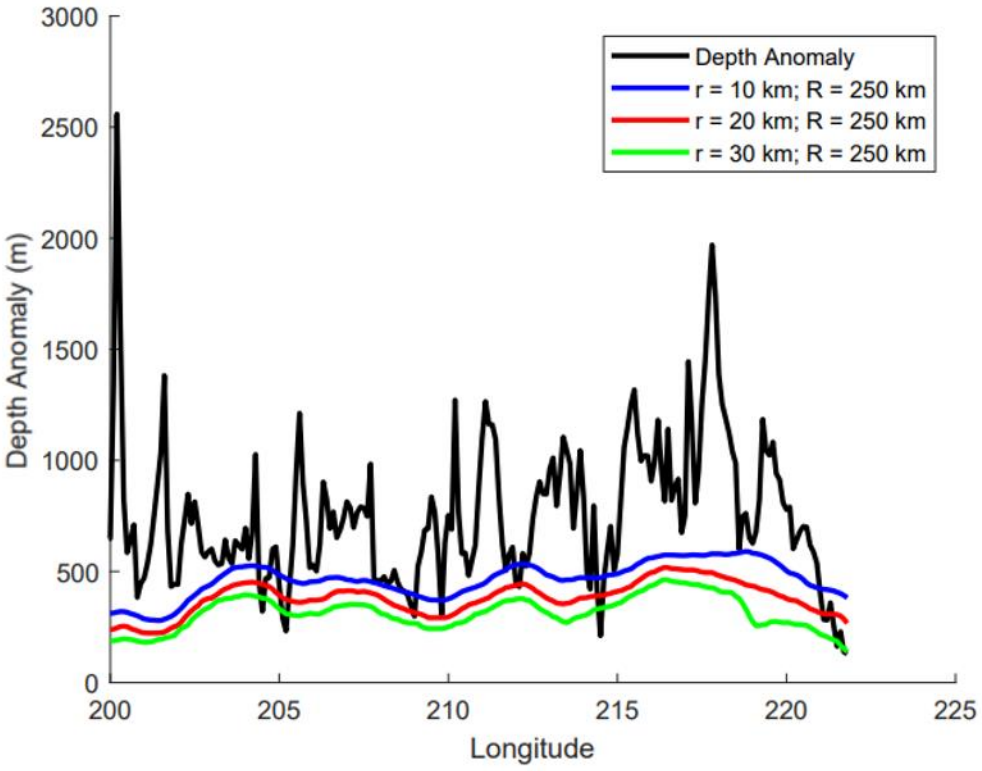

Figure 4.13. Influence of the minimizing filter radius along the main axis.
Magnification along the youngest part of the chain.

In the previous section, we showed a minimizing filter of r = 20 km produces the characterization of the swell. The same conclusion can be made while looking along the main axis. The curve of filter r = 10 km (blue line) is indeed too high and removes a non-negligible part of the volcanoes while the curve of filter r = 30 km (green line) is too low. It overestimates the volume represented by the volcanic products and underestimates the swell volume.

Figures 4.14 and 4.15 show graphically the influence of the median filter, R, on the filtered depth anomaly curve. Figure 4.15 focuses on the youngest part of the chain, where the swell is associated with the seamount chain. In the previous section, we eliminated the curve calculated by the filter R = 150 km (blue line) but could not distinguish between the R = 350 km (green line) or R = 250 km (red line) curves. Along the main axis, we can see that the curve from the R = 250 km filter provides the best estimate of the swell component. The curve from the R = 350 km filter smooths out too much the long scale variations (wavelength ~500 km), which we can see in the depth anomaly (black line in Figure 4.15), and that are generally associated with hotspot swells (Crough 1983; Vidal and Bonneville, 2004; Adam et al., 2007).

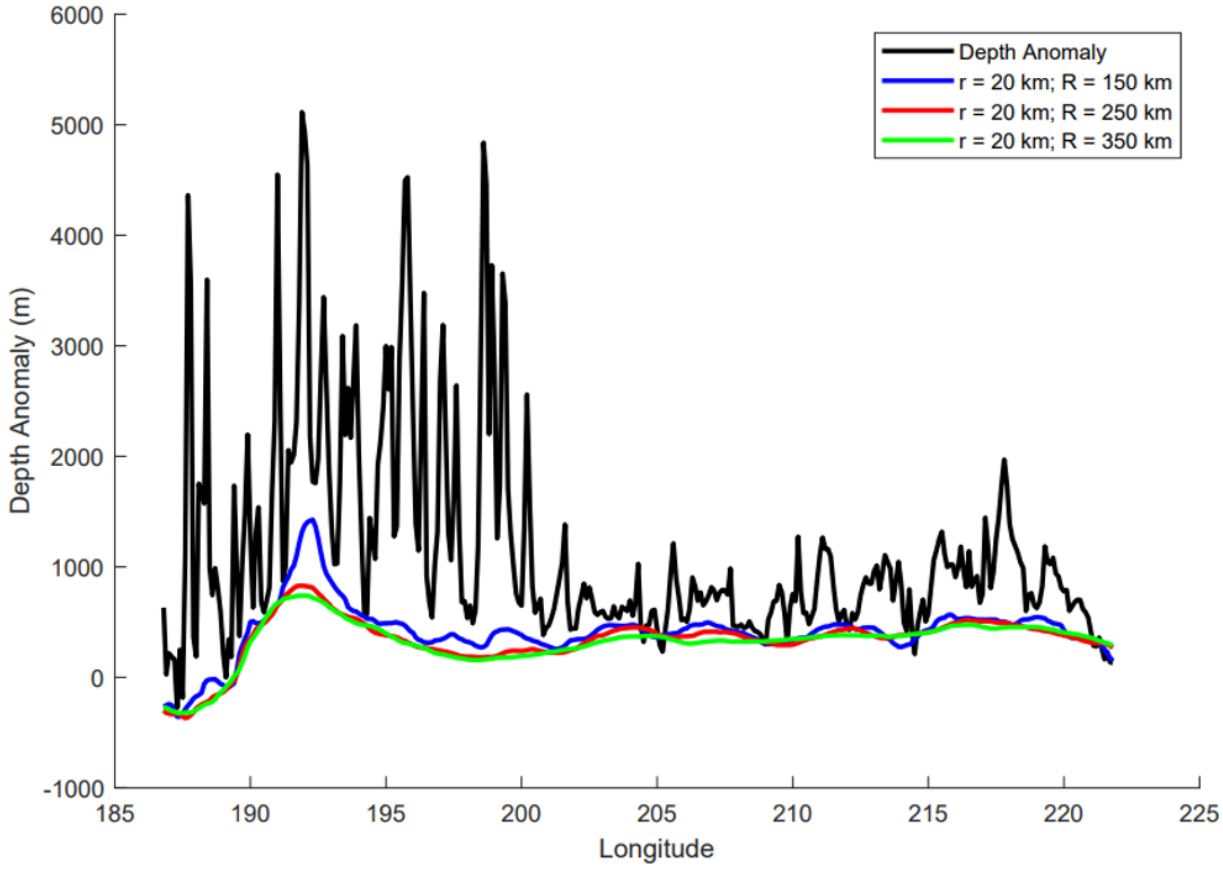

Figure 4.14. Influence of the median filter radius along the main axis.
The color scheme is reported in the legend.

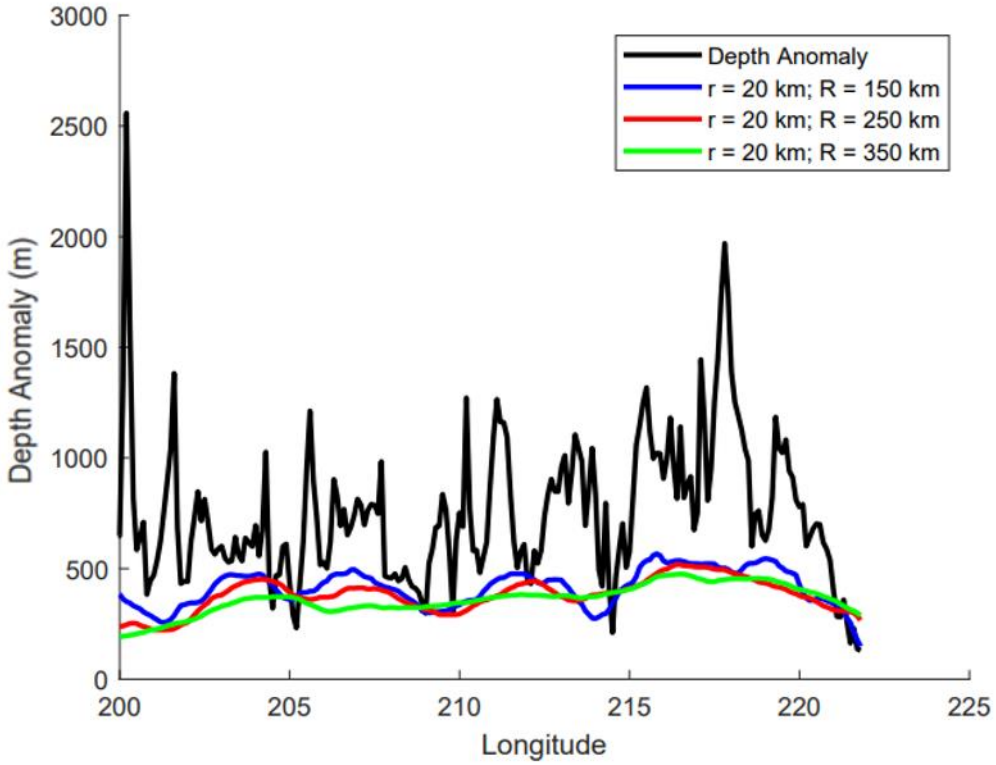

Figure 4.15. Influence of the median filter radius along the main axis.
Magnification along the youngest part of the chain.

4.2. Influence of the compensation root

Before we compute the swell and magmatic fluxes, we must first consider the compensation root. As stated in the Methods section, in order to compute the volume of magmatic products, i.e., the volcanic edifices volume, we had to take into account that the lithosphere has a finite strength, and therefore flexes downwards when loaded by volcanoes (Watts et al., 1975; 1980). Previous studies have pointed out that ignoring the volume of magmatic material encompassed in the flexural root would lead to underestimating the total

volume of erupted magmatic material (Watts et al., 1975; 1980; Smith, 1990; White, 1993; Vidal and Bonneville, 2004; Adam et al, 2007).

There are two main models of compensation to consider. The compensation can be local (this is called 'Airy' compensation) or regional. If the compensation is regional, its computation takes into account the fact that the lithosphere has an elastic thickness (Watts and tenBrink, 1989). The elastic thickness depends on the age of the lithosphere at the time of loading, as illustrated in Figure 4.16.

Calculation of the lithospheric flexure was done by my advisor, Dr. C Adam, so I will only briefly summarize this calculation. It is, however, important to test the influence of the compensation mechanism of the fluxes' computation. The elastic thickness is generally considered to be situated between the isotherms 450^{o}C and 600^{o}C (Watts and Ribe, 1984), as illustrated in Figure 4.16. The youngest volcano along the Louisville chain, (1.1 Ma), is located on seafloor that is 45 Ma old (Figure 4.17a). This corresponds to an elastic thickness of 20 – 25 km.

In Figure 4.17b, I report in blue the flexure computed with an elastic thickness of 25 km, and in the red the flexure computed assuming a local or 'Airy' compensation, along the AA' profile represented in Figure 4.17c. When the compensation is local, most of the flexure is located immediately beneath the volcanoes. When the flexure is computed assuming an elastic thickness of 25 km, the flexure wavelength is larger, while the amplitude is smaller.

In Figure 4.18, I report the magmatic flux computed with the local compensation (in red) and with a regional model assuming an elastic thickness of 25 km (in blue). The means of each mode are reported in Table 2. We have only included the first two segments of the Louisville

chain, where the swell is observable. The estimated fluxes calculated by the two approaches are similar, with only a .5 difference between them. This lack of sensitivity of the magmatic flux to the compensation mechanism has already been noticed by Vidal and Bonneville (2004). The Airy approximation gives the same results as the regional model. This is illustrated in Figure 4.19, extracted from Vidal and Bonneville (2004). This can be explained by the fact that the flexure volume is the same whatever the compensation mechanism. The shape of the flexure (i.e., its wavelength) and amplitude changes however. In the following we used a compensation root, computed assuming an elastic thickness of 25 km (blue line in Figure 4.18).

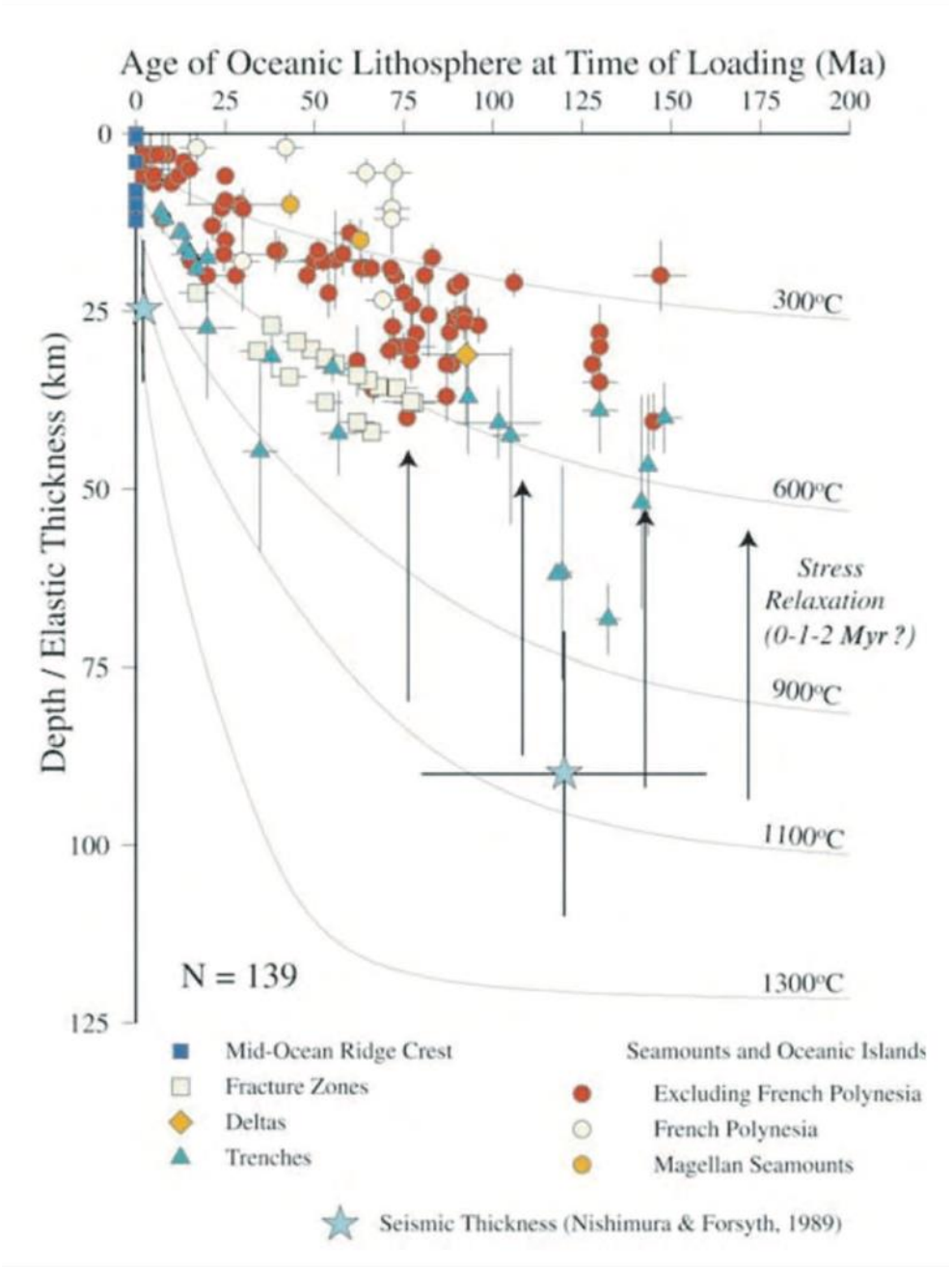

Figure 4.16. Elastic thickness of the lithosphere as a function of the seafloor age at the time of loading

The isotherms correspond to the plate model (Parsons and Sclatter, 1977). The seismic thinness is from Nishimura and Forsyth (1989). The arrows indicate the short-term relaxation of the seismic thickness.

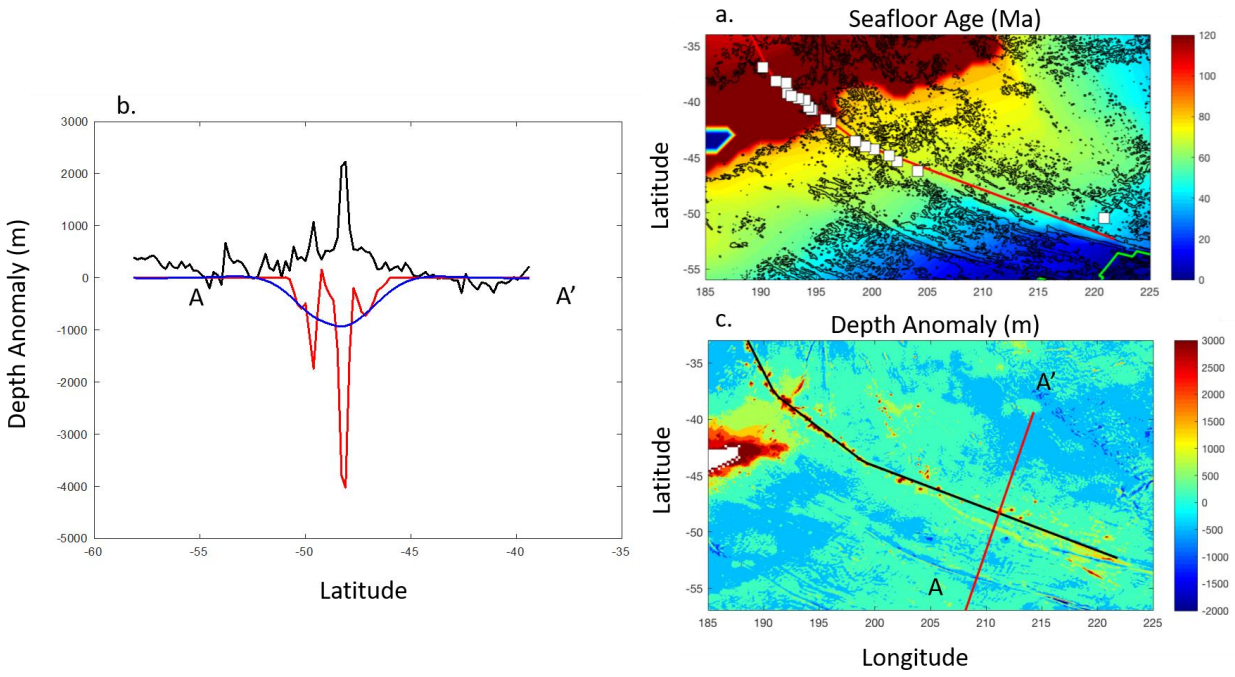

Figure 4.17. Compensation root.

(a) Seafloor age along the Louisville chain. (b) Profile showing the depth anomaly, in black as well as the flexure computed with an elastic thickness of 25 km in blue, and the flexure computed assuming a local or 'Airy' compensation in red. (c) Location of the profile along which we study the compensation along the depth anomaly map.

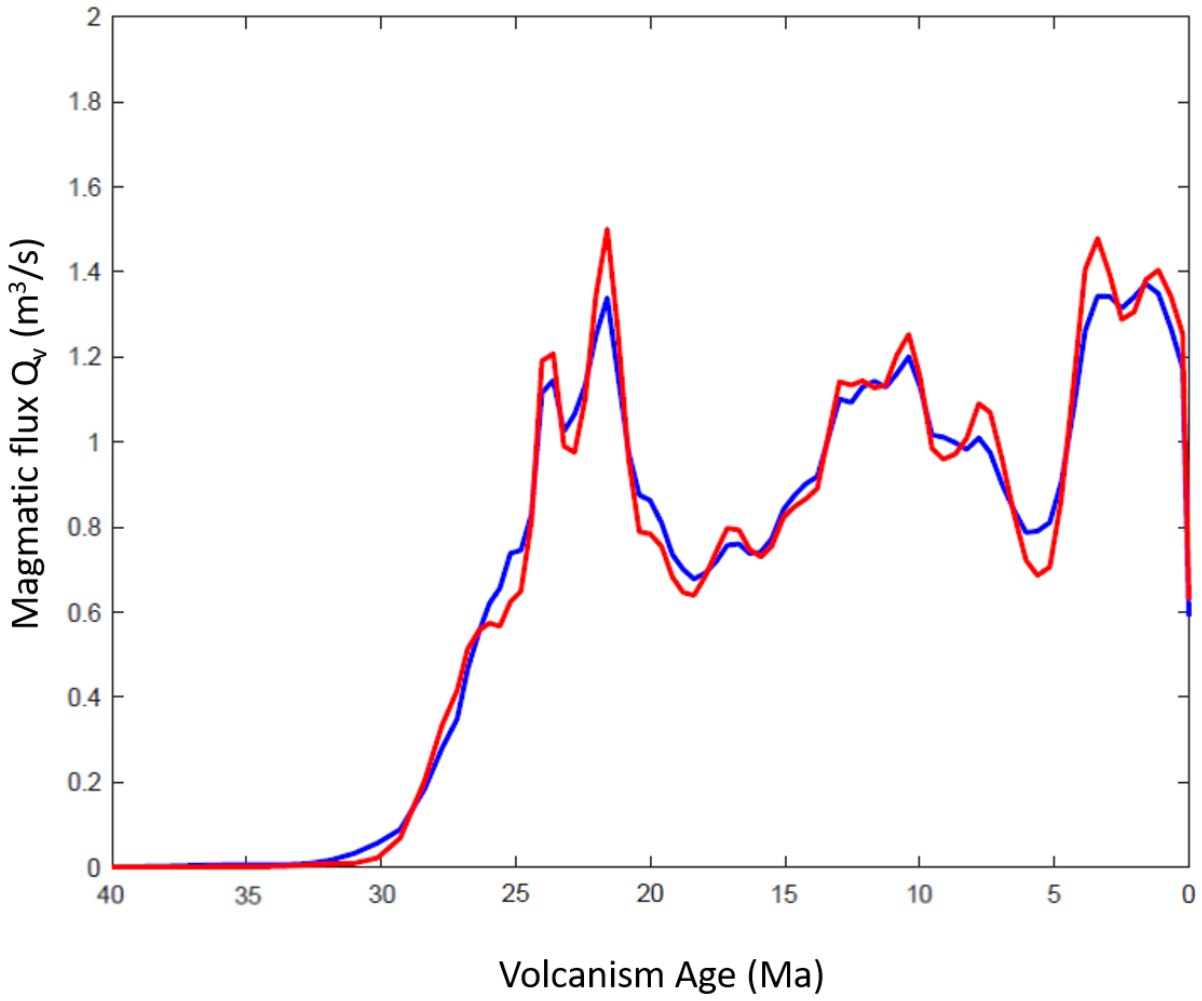

Figure 4.18. Magmatic flux, Q_v.

Computed assuming a local compensation (in red) and with a regional model assuming an elastic thickness of 25 km (in blue).

Table 2. Mode of compensation magmatic fluxes

Mode of Compensation	Magmatic Flux ($m^3\ s^{-1}$)
Elastic Thickness	0.92
Local ('Airy')	0.95

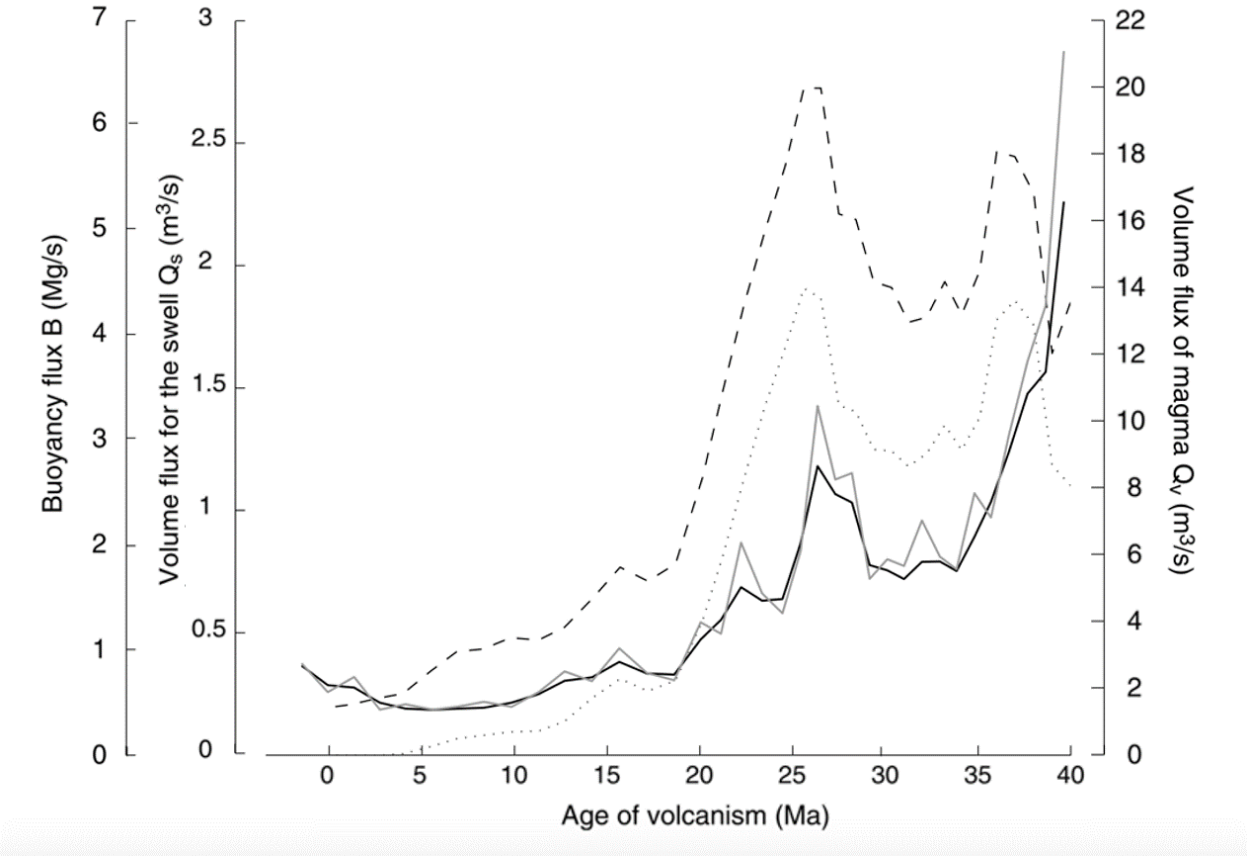

Figure 4.19. Magmatic and swell fluxes along the Hawai'ian chain.
Correlation between the two calculated parameters: (1) temporal variation of the volume flux of magma (left axis) when assuming an Airy compensation (gray line) or a flexural deformation (black line) and (2) temporal variation of the volume flux Qs associated with the swell and buoyancy flux B (right axis) for the Parsons and Sclater (PS) model (dashed line) and the Global Depth and Heat flow model (GDH1) (dotted line) thermal subsidence models Figure modified from Vidal and Bonneville (2004).

4.2.1. Influence of the filter parameters on the flux determinations

A minimizing filter of radius r = 20 km and a median filter of radius of R = 250 km produces a good estimate of Louisville's swell. The difference between the results for a median

filter of R = 250 km vs. R = 350 km is relatively small, so we use the R = 250 km filter for the remaining calculations.

In this section, we investigate the influence of these parameters on the preliminary swell and magmatic fluxes. The official swell and magmatic fluxes will be calculated in the next section. As stated previously in the *Methods* section, we used the sliding box method to calculate the swell and magmatic fluxes (Figure 3.6). The magmatic flux is calculated by the sliding box measuring the volcanic edifices volume between the topography and regional flexure (i.e., elastic thickness of 25 km) along the filtered depth anomaly. The swell flux is calculated in a similar way. The sliding box measures the swell's volume between the base of the seafloor and the top of the swell. To make this a function of time, the volumes of the swell and magmatic material will be divided by the volcanic age difference contained within the box. The influence of the parameters of the box (w_b, l_b, and t_b) will be described in the next few sections.

In Figures 4.20 and 4.21, we show the swell and magmatic fluxes computed while varying the filtering parameters. In Figure 4.21, we magnified the y-axis to observe the youngest part of the chain where we can find the Louisville swell. The mean swell and magmatic fluxes for the youngest part of the chain are reported in Table 3. In Figures 4.20a and 4.21a, we can see that varying r has a noticeable effect on the amplitude of the swell flux, Q_s. The differing minimizing filters calculate a difference in the mean swell flux of .4 – .5 $m^3 s^{-1}$. When r is too small, as is the case for r = 10 km, we underestimate the volume of the volcanic edifice and overestimate the swell volume, as discussed above. The shape of Q_s seems relatively unaffected by variations in r. The magmatic flux, Q_v, (Figures 4.20b and 4.20b) also varies as a function of r. However, the amplitude of Q_v varies less than the amplitude of Q_s. The difference among the

mean magmatic fluxes ranges from .002 – 3 $m^3 s^{-1}$. Results presented in sections 4.1.1. – 4.1.4. and below show that a value of r = 20 km provides the best fit for the minimizing filter.

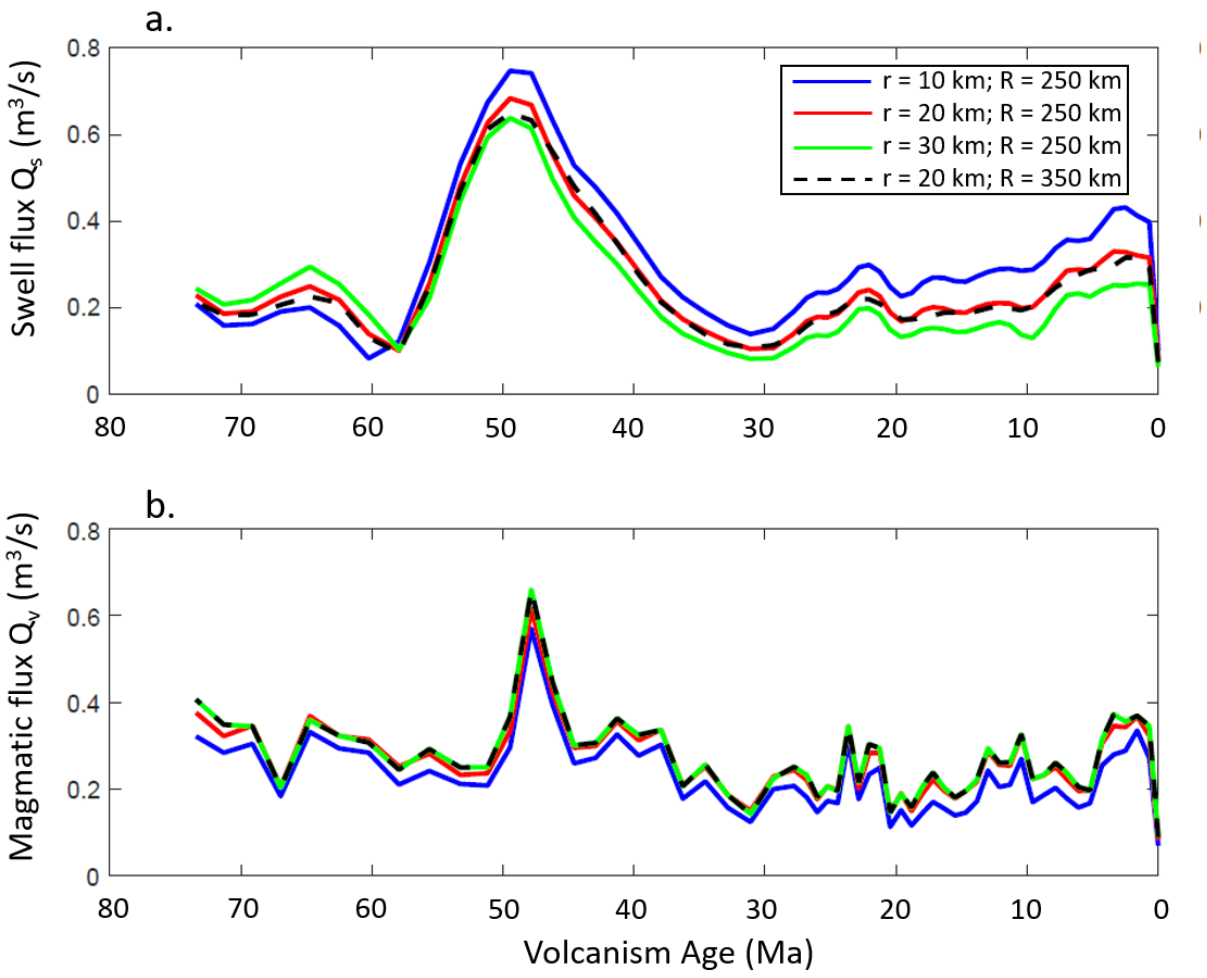

Figure 4.20. (a) Swell and (b) magmatic fluxes computed along the Louisville chain. The different color lines represent the fluxes computed with different filters. Blue, r = 10 km, R = 250 km. Red, r = 20 km, R = 250 km. Green, r = 30 km, R = 250 km. Dashed black r = 20 km, R = 350 km.

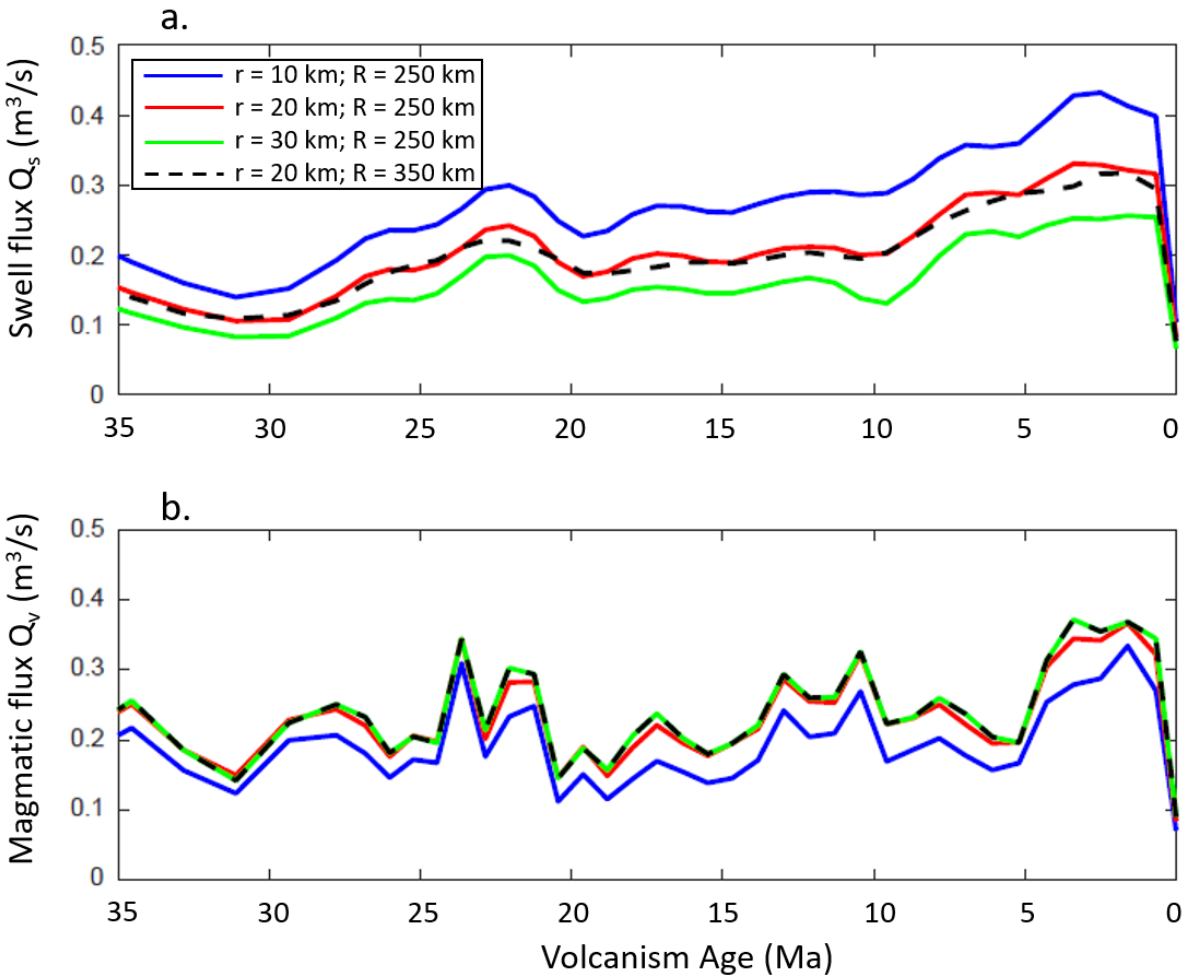

Figure 4.21. Magnification of (a) swell and (b) magmatic fluxes computed along the Louisville chain.

Magnification of the youngest part of the chain, from volcanic ages 0 – 35 Ma, where the swell is located from Figure 4.20.

Table 3. Summary of swell and magmatic fluxes of varying minimizing and median filters

Minimizing Filter (r)	Median Filter (R)	Swell Flux (m^3 s^{-1})	Magmatic Flux (m^3 s^{-1})
10	250	0.2746	0.1908
20	250	0.2092	0.2307
30	250	0.1623	0.2371
20	350	0.2018	0.2371

4.3 Influence of the sliding box parameters on the swell determination

Once the swell and magmatic components have been separated, we used the "sliding box" method, (described in *Methods* section) previously developed by Vidal and Bonneville (2004) and Adam et al. (2007), to compute the final swell and magmatic volumes. During this process, a box with characteristic length (l_b), and width (w_b), is translated along the main axis, with a translation step (t_b) (Figure 5 in *Methods* section). The volume of magmatic material and swell encompassed in this box is computed for each translation step. In this section we tested the influence of the sliding box parameters on the swell and volcanism fluxes along the Louisville volcanic chain.

4.3.1 Influence of the length of the box, l_b

We first tested the influence of the length of the box, l_b, on the swell and magmatic flux computations. This parameter depends on the characteristics of the volcanic chain and associated swell. Previous studies on the Hawaiian, Walvis, and St. Helena chains have used l_b = 1000 km (Vidal and Bonneville, 2004; Adam et al., 2007) due to their physically larger and more widespread volcanoes. Since the volcanoes associated with the Louisville chain are smaller and less widespread relative to the main axis (Figure 3, Background Information), we also tested smaller values. To test the influence of the length of the box, we considered values of l_b = 500 (black line in Figure 23), 700 (red line), and 1000 km (blue line), while the width and translation step of the sliding box are kept constant ($w_b = t_b$ = 50 km). The swell and magmatic fluxes obtained with these parameters are displayed in Figure 4.22a (magmatic flux) and Figure 4.22b (swell flux).

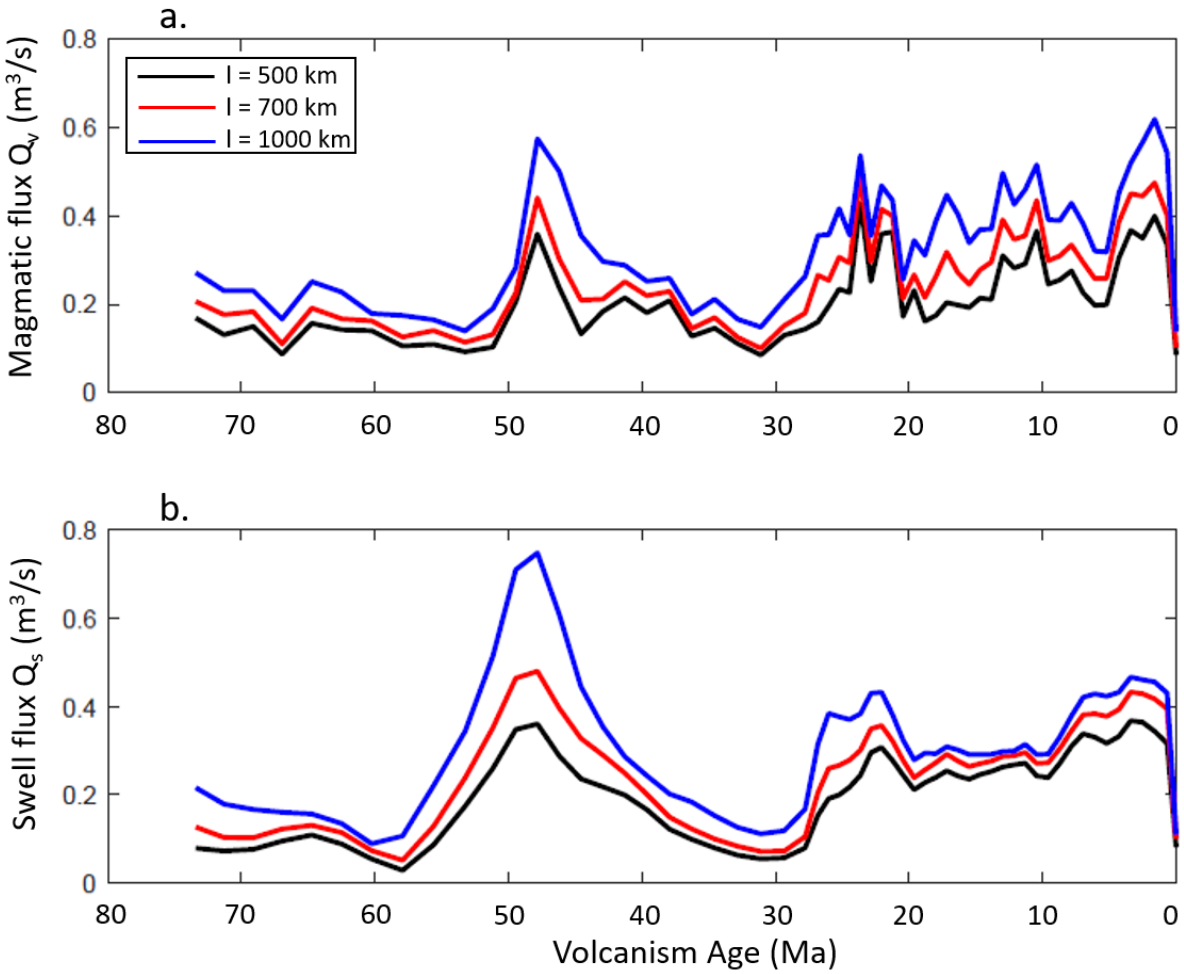

Figure 4.22. The influence of length of the translating box on the (a) magmatic and (b) swell fluxes.

For both fluxes, the width and translation step are at 50 km. The x axis represents the age of volcanism and the y axis represents the depth anomaly.

We noticed that increasing the length of the sliding box, decreases the amplitudes of both fluxes (Figure 4.22). This is due to the fact that most of the volcanoes and swell are concentrated along the main axis. If the box is not long enough, the computation will not consider all the material created by the Louisville plume, especially towards the end of the track. As the fluxes are the volumes of the swell and the volcanoes encompassed in the sliding box, divided by the

surface area of this box, this will lead to an overestimation of the flux amplitude. Only the maximal values of the swell and magmatic volumes will be encompassed in the sliding box. If the box is too long, we underestimate the flux amplitudes, as regions not associated with volcanoes or swell will be encompassed in the box. Based on considerations of the volcano and swell characteristics, we decided that the length of 700 km (l_b = 700 km) is the best parameter for both fluxes along the Louisville chain. l_b = 700 km was chosen because this length encompasses all of the volcanoes and the associated swell. Anything bigger will be gathering unneeded information and anything less will be cutting out volcanoes from the measurements. Figure 4.23 illustrates the different sizes of the boxes being sent along the chain.

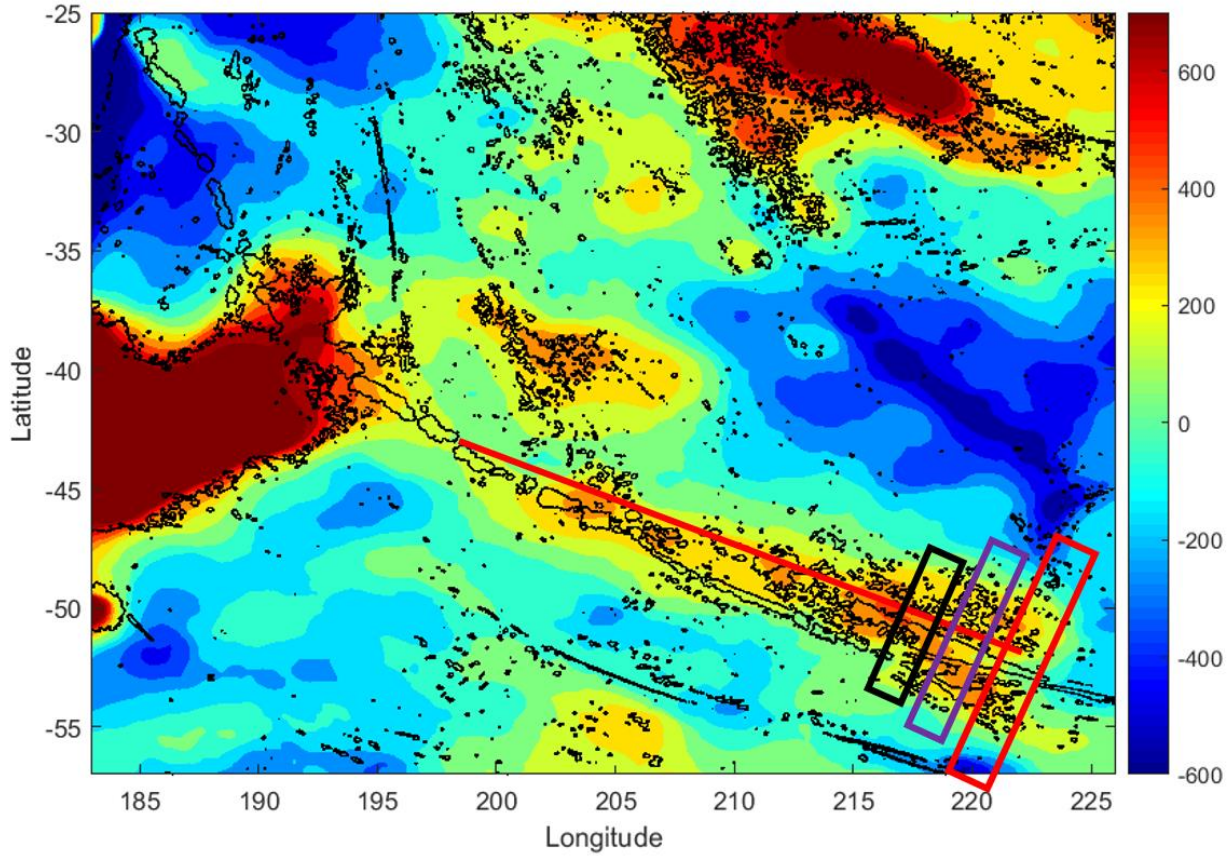

Figure 4.23. Illustration of the sliding boxes length along the youngest segment of the chain. The swell map was created with a r = 30 km; R = 250 km filter. The black box represents l_b = 500 km, the purple box represents l_b = 700 k, and the red box represents l_b = 1000 km.

The tests on the length of the box, l_b, are necessary to see whether this parameter has any influence of the computed fluxes. As we can see in Figure 25, l_b has an influence on the amplitude of the fluxes, but the pattern of theses fluxes remains almost unchanged while varying l_b. Two exceptions have been noted, however.

In Figure 4.22b, we see that l_b = 500 and 700 km identify the smaller variations associated with the swell flux while the flux computed with l_b = 1000 km starts to lose these for ages less than 20 Ma. Similarly, the magmatic flux computed with l_b = 1000 km show fewer details than the other fluxes for ages younger than 5 Ma (Figure 4.22a).

4.3.2. Influence of the width of the box, w_b

Similar to Vidal and Bonneville (2004) and Adam et al. (2007), our test on the influence of the box width set the translation step and width of the box equal to one another ($t_b = w_b$). Previous studies assigned a box width of 100 km for Hawaii (Vidal and Bonneville, 2004) and 20 km for Walvis and St. Helena (Adam et al., 2007). In our study, we kept the length constant at l_b = 700 km, had the translation step equal the width of the box, and varied the width from w_b = 20, 50, and 100 km. Figure 4.24a illustrates the influence of the width of the sliding box on the volcanism flux, while Figure 4.24b illustrates its influence on the swell flux.

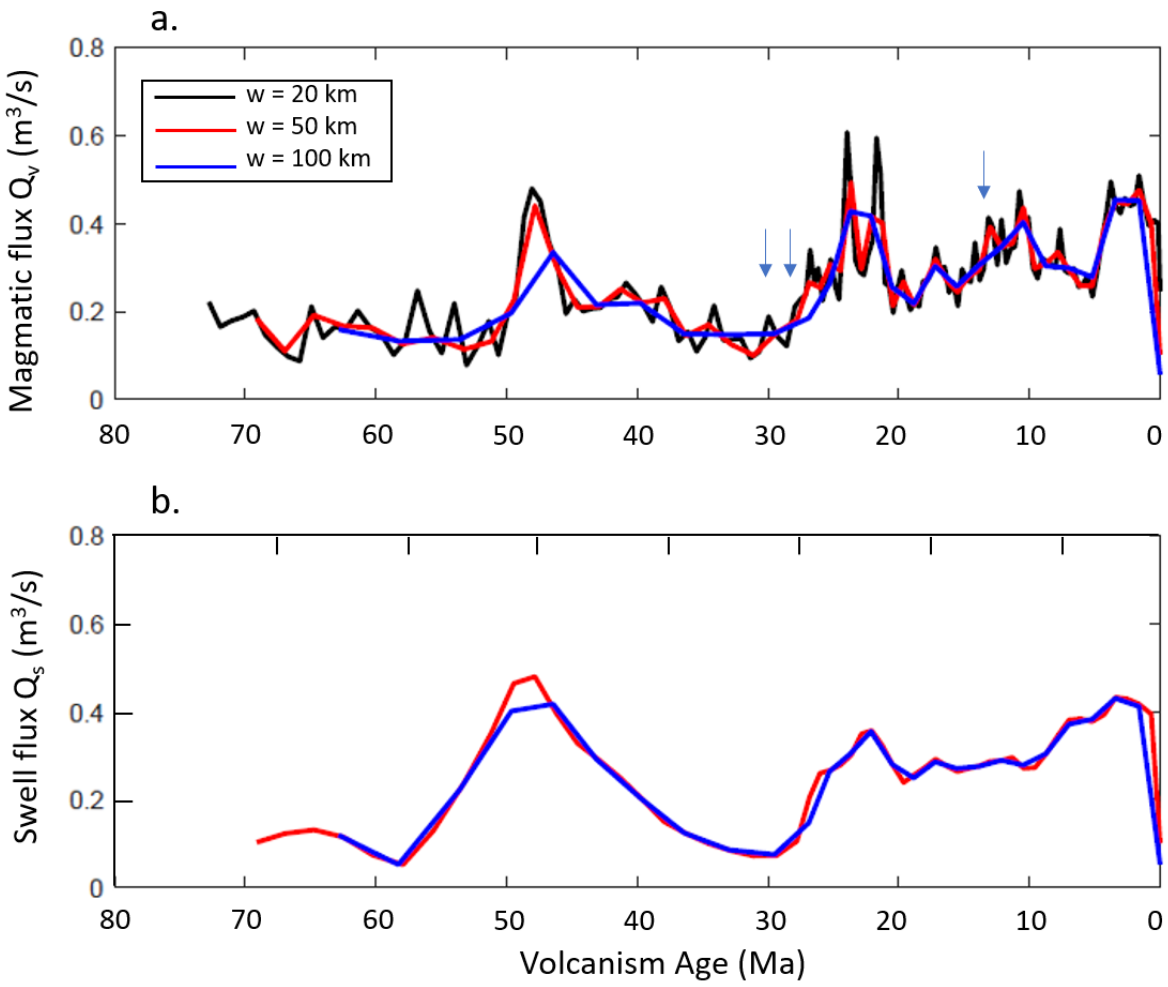

Figure 4.24. The influence of width of the sliding box on the (a) magmatic and (b) swell fluxes.

For both fluxes, the length of the sliding box is 700 km and the translation step is equal to the width for each test. Blue arrows indicate individual volcanoes.

We noticed that by increasing the width value, w_b, the amount of detail in both fluxes is reduced. We see the largest difference are found for the magmatic fluxes (Figure 4.24a). There are almost no differences in the calculated swell fluxes (Figure 4.24b). The differences between the black (w_b = 20 km) and red (w_b = 50 km) lines in Figure 27a are consistent with the locations of individual volcanoes (indicated by the blue arrows). Since we wanted a flux that illustrates

the general trend of the fluxes, without details at the scale of volcanoes, we decided that w_b = 50 km is a better parameter than w_b = 20 km. When comparing the blue (w_b = 100 km) and red (w_b = 50 km) lines in Figure 4.24a, we can see that more variations are seen with w_b = 50 km. Using w_b = 100 km does not encompass all the variations we want to study. Therefore, w_b = 50 km is the most suitable value for this parameter.

4.3.3. Influence of the translation step, t_b, and overlap of the sliding boxes

In previous studies, the translation step is equal to the width of the box ($t_b = w_b$), (Vidal and Bonneville, 2004; Adam et al., 2007). This means that there is no overlap between the sliding boxes. Here we test the influence of the overlap of the sliding boxes. We varied the step as t_b = 50, 25, and 5 km as we kept the length and width constant at 700 and 50 km respectively. The overlap of the boxes when t_b = 50 km is 0%. When t_b = 25 km and t_b = 5 km, the overlap is 50 % and 90% respectively. Illustrations of these overlaps are reported in Figure 4.25. The results of the sensitivity of the fluxes on the translation step are reported in Figure 4.26. Figure 4.26a illustrates the volcanism flux while Figure 4.26b illustrates the swell flux.

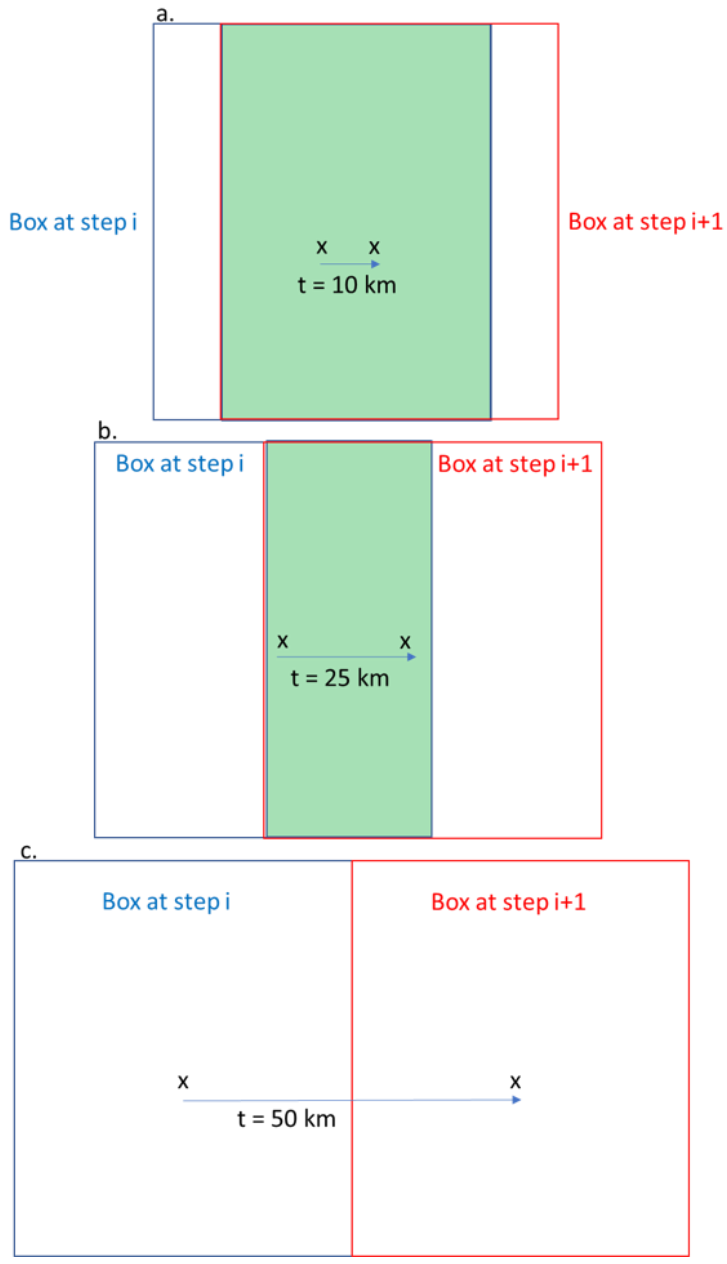

Figure 4.25. Varying the translation step, t_b, and the overlap

For the three cases illustrated here, the length and width of the sliding box are 700 and 50 km respectively. In panel a, the translation step, t_b, is 10 km, in panel b 25 km, and in panel c is 50 km. The blue and the red rectangles represent the sliding box at two consecutive iterations. The green area represents the overlap between two computation steps. The overlap percentage in panels a, b, and c is 90%, 50%, and 0% respectively.

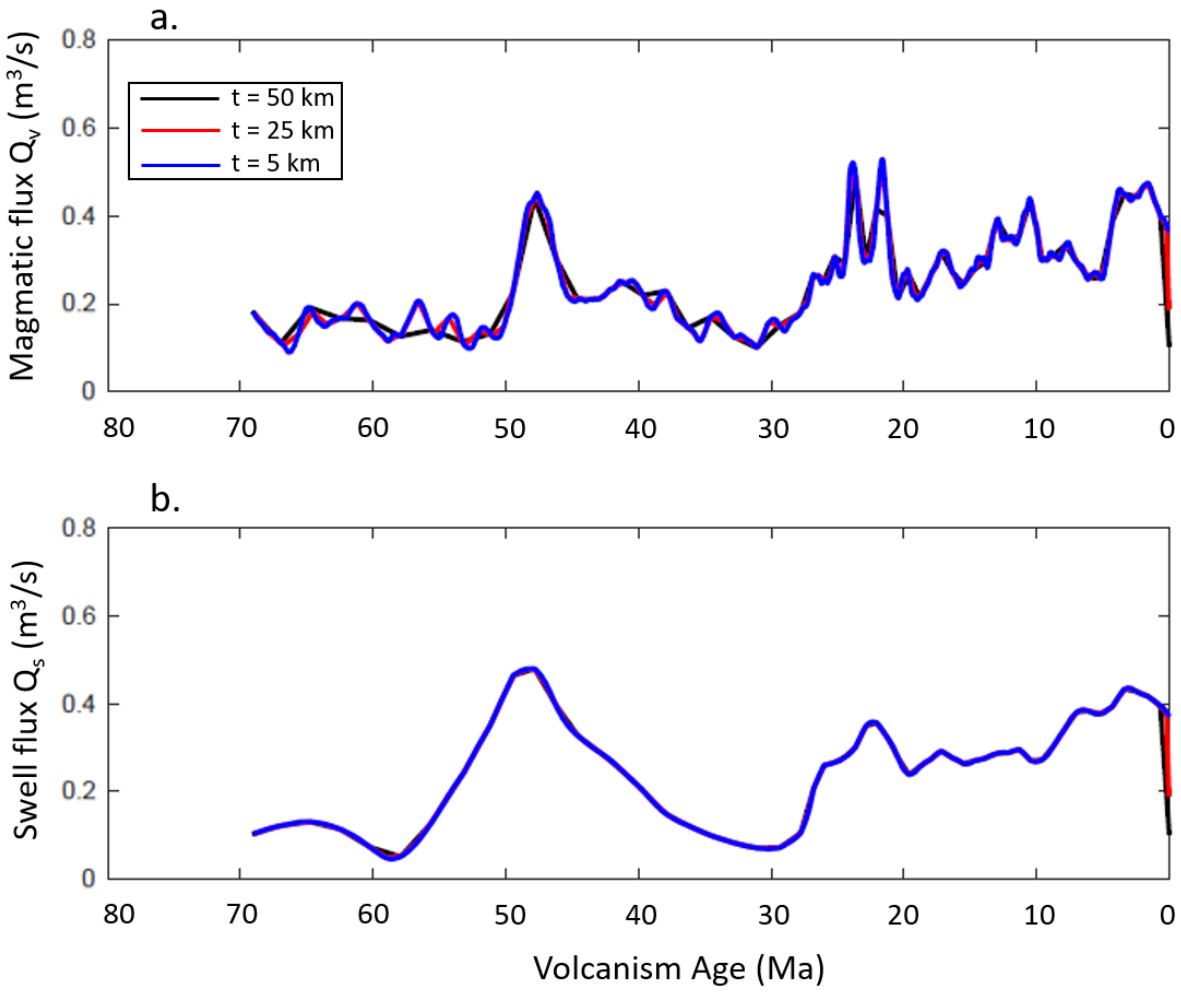

Figure 4.26. The influence of the translating steps on the (a) magmatic and (b) swell fluxes. For both fluxes, the length of the sliding box is 700 km and the width 50 km. The x axis represents the age to active volcanism and the y axis represents the depth anomaly.

In Figure 4.26, we see that increasing the translation step, t_b, decreases the amount of details seen in the fluxes. We can also see that there is actually very little difference between the magmatic fluxes, Q_v, computed with t_b = 5 km (blue line, corresponding to a 90% overlap) and t_b = 25 km (red line, corresponding to a 50% overlap). The Q_v represented in black has been computed with t_b = 50 km, and therefore, there is no overlap in this case. Some details in the Q_v

variations seem to be lost by using this last value. We decided that a step of 25 km is the most adequate, as it gives us a detailed description of the temporal variations of the volcanism flux. In Figure 29b, we can see there is very nearly no difference between the swell fluxes computed while varying t_b. To summarize, the box parameters to best approximate the swell and magmatic fluxes are l_b = 700 km, w_b = 50 km, and t_b = 25 km.

Chapter 5 - Discussion

In this section, we discuss the temporal evolution for the swell and magmatic fluxes along the Louisville hotspot. We will focus on the Louisville swell and magmatic fluxes for ages younger than 35 Ma because any variations seen from the swell fluxes at older ages are associated with the Hikurangi plateau (see section 4.1.4; Ito and van Keken, 2007). The fluxes are also compared to the previous studies performed by Vidal and Bonneville (2004) and Adam et al. (2007) on Hawai'i-Emperor, Walvis, and St. Helena volcanic chains. We then discuss the potential origin of the temporal variations of the swell and magmatic fluxes.

5.1 Temporal evolution of the swell (Q_s) and magmatic (Q_v) fluxes

5.1.1 Variations observed along the Louisville seamount chain

The calculated swell and magmatic fluxes, computed along the Louisville chain, through the methods described in sections 3 and 4 (see for example Figure 4.18 in section 4.2 and Figure 4.20 in section 4.2) are illustrated in Figure 5.1 in the upper and lower panels respectively. For the past 30 m.y. both of these fluxes have been increasing, which indicates that the plume's activity (i.e., magma production) is also increasing (Figure 5.1). These trends are highlighted by the black lines in Figures 5.1 and 5.2. The black lines have been computed through linear regression between the fluxes and the volcanism age ("polyfit" function in Matlab).

We observe several maxima in both Q_s and Q_v at 2, 12, 25 Ma (blue arrows on Figure 5.1) which occur around every 10 m.y. We also notice oscillations that occur for ~5 m.y., which are identified by dashed green ellipses in Figure 5.2. These ~5m.y. variations occur from 25 – 20 Ma, 15 – 10 Ma, and 5 – 0 Ma in both fluxes. In the following, we discuss the origin of the flux's variations along the Louisville hotspot chain and compare them to the variations observed along other long-lived chains.

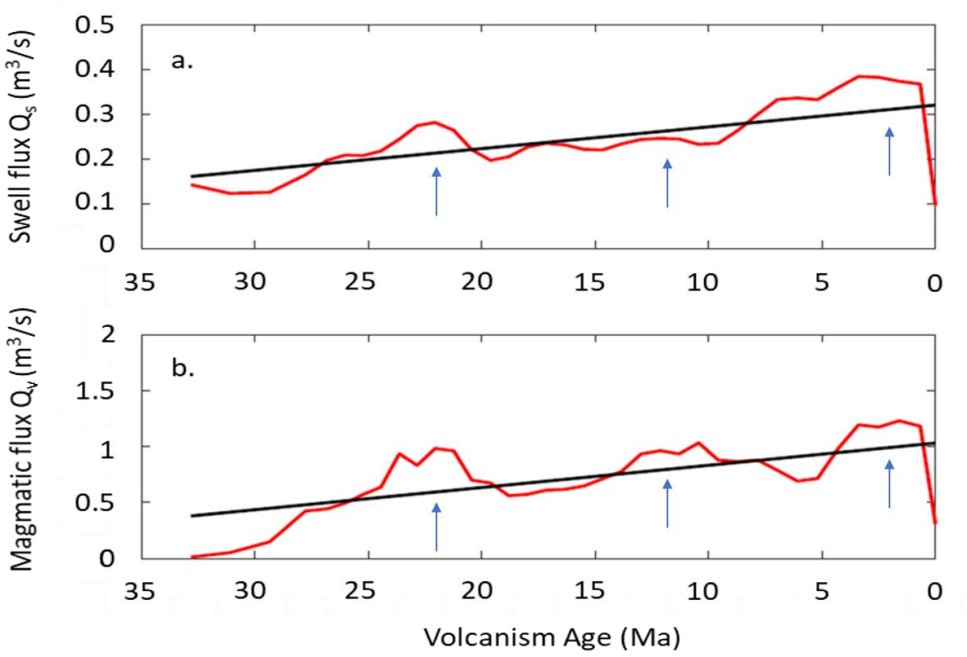

Figure 5.1. Trends and correlations between the (a) swell and (b) magmatic fluxes along the Louisville chain.

The black line indicates the trend of these fluxes. They have been computed through linear regression between the fluxes and volcanism age. The blue arrows indicate peaks that are found simultaneously in Q_s and Q_v.

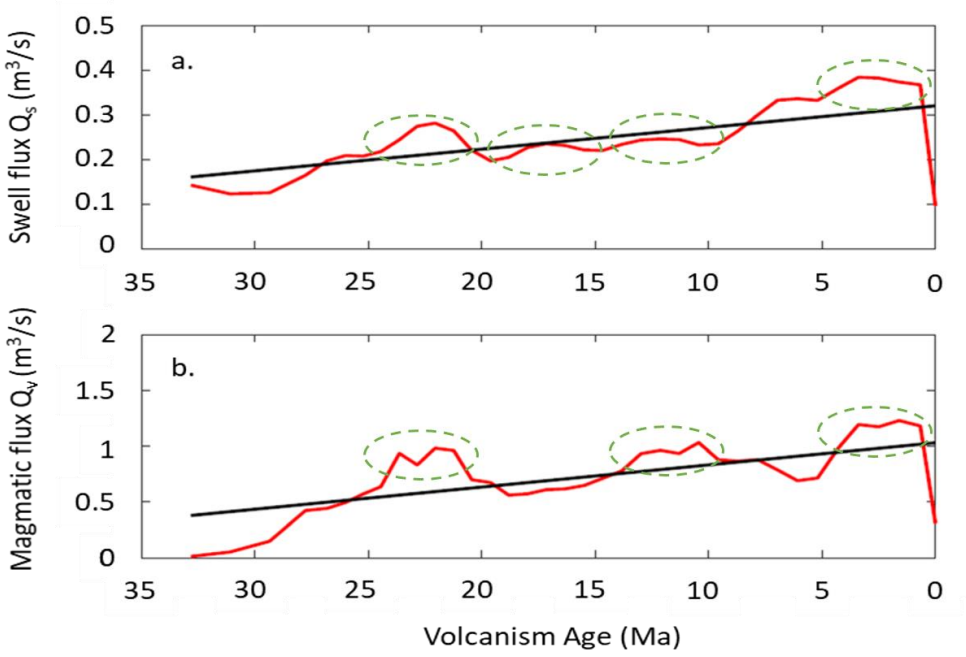

Figure 5.2. Variations of the (a) swell and (b) swell magmatic fluxes along the Louisville chain.

The green dashed ellipses indicate short wavelength features that occur for 5 m.y.

5.1.2 Comparison of plume activity

In Figures 5.1 and 5.2, we observe that the swell and magmatic fluxes along the Louisville seamount chain have been increasing for the past 30 m.y. Similar to the Louisville chain's trend, the Q_s and Q_v for the Hawai'ian chain have been increasing for the past 30 m.y. (Vidal and Bonneville, 2004) (Figure 5.3). Along the Walvis Ridge and St. Helena chain, the Q_s and Q_v have been decreasing over the past 60 m.y. and 80 m.y. respectively (Adam et al. 2007). Interestingly, the Q_s and Q_v trends are generally well correlated along each hotspot track, which indicates a connection between the fluxes. The St. Helena hotspot track seems to be an exception, as the magmatic flux indicates the presence of two plumes (Adam et al., 2007). This pattern makes the interpretation of the temporal evolution of Q_s and Q_v along the St. Helena chain more difficult.

For the Hawai'ian chain, the increasing trend in both Q_s and Q_v has been interpreted as evidence for an increase in the plume activity (i.e., increase in magma production) during the past 30 m.y. (Vidal and Bonneville, 2004), while for the Walvis and St. Helena hotspots, the decrease in both Q_s and Q_v has been interpreted as a decrease in plume activity (i.e., decrease in magma production) during the past 60 and 80 m.y. respectively (Adam et al., 2007). A previous study has reported that the plume activity of the Louisville hotspot has been decreasing for ~20 m.y. (Lonsdale, 1988). Lonsdale (1988) reports that the Louisville chain's plume used to produce magma at a rate of ~3-4 x 10^3 km^3/m.y. that this would create an evenly spaced volcanic chain with volcanoes averaging ~2-4 x 10^3 km^3 in volume. At ~25 Ma, this magma production rapidly declined, creating a dispersed volcanic chain, in which the volcanoes rarely reach sea level (Lonsdale, 1988). However, while Figure 3.1 does indicate a more sparsely distributed volcanic trail, the Q_s and Q_v provide a clearer image on how a plume's activity is behaving (Vidal and Bonneville, 2004; Adam et al., 2007). Based off of the observations seen along the Q_s and Q_v trends of the Hawai'ian and Walvis chains, we interpret the increase of these fluxes along the Louisville seamount chain as an increase in plume activity.

Which phenomena could account for an increase in the plume activity, such as the one observed along Louisville and Hawai'i? According to Vidal and Bonneville (2004), the increase in activity along the Hawai'ian chain can be accounted for by an increase in plume temperature or an increase in the volume of magmatic material from the plume. White (1993) states that the increasing plume activity is caused by the rising melt production rate. The variations seen in the degree of melting could be caused by variations in lithosphere thickness (Regelous et al., 2003). However, Harrison et al. (2017) argues against the influence of lithosphere thickness and instead proposes a change in the Hawai'ian plume source composition.

If the magmatic flux is influenced by lithosphere thickness, then it should also influence the $^{208}Pb^*/^{206}Pb^*$ isotopic signature (Harrison et al., 2017). For example, the $^{208}Pb^*/^{206}Pb^*$ isotopic signature would be lower in lavas that have formed due to higher degrees of melting (Pertermann and Hirschmann, 2003; Garcia et al., 2010). However, both the Emperor seamount chain and Hawai'ian volcanic chain experience a similar range of variations regardless of lithospheric thickness (Figure 5.4). The Emperor seamounts have a lithospheric thickness of 22.4 – 92.2 km and a $^{208}Pb^*/^{206}Pb^*$ signature ranging from 0.89 to 0.94, while the Hawai'ian chain has a lithospheric thickness of 89.4 – 98.2 km and a ranging $^{208}Pb^*/^{206}Pb^*$ signature from 0.92 to 0.97 (Harrison et al., 2017). Since the difference between both of these ranges is only 0.05, it suggests that lithospheric thickness doesn't affect the magmatic flux (Harrison et al., 2017). Harrison et al. (2017) proposes that the enrichment of $^{208}Pb^*/^{206}Pb^*$ along the Hawai'ian chain is the result of deep-mantle plume movement. Since the plume source is currently located in the ultra-low velocity zone (ULVZ) near the Pacific low shear velocity province (LLSVP), Harrison et al. (2017) states that the plume originated outside of this area, but slowly migrated into it. This would mean that the Emperor seamounts low $^{208}Pb^*/^{206}Pb^*$ isotopic signature is from a depleted material while the Hawai'ian chains high $^{208}Pb^*/^{206}Pb^*$ isotopic signature is from an enriched ULVZ and LLSVP material (Harrison et al., 2017).

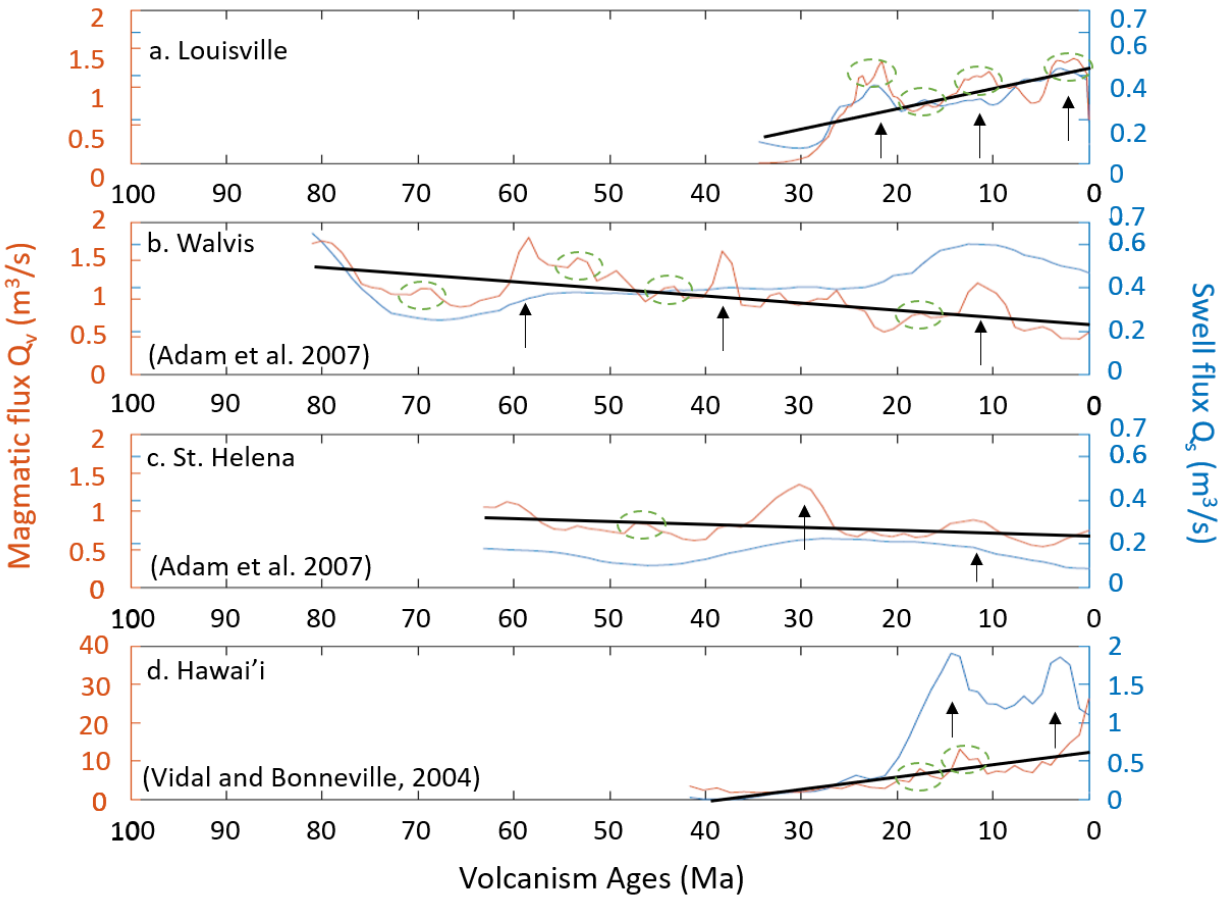

Figure 5.3. Swell and magmatic fluxes along the (a) Louisville, (b) Walvis, (c) St. Helena, and (d) Hawai'i chains.

The blue curve represents the calculated swell flux, the red curve represents the calculated magmatic flux. The dashed green ellipses identify the 5 m.y. long variations seen along every chain. The black arrows represent correlations between the maxima of Q_s and Q_v. Black line represents the calculated trend of the Q_s and Q_v fluxes, this trend was computed through linear regressions between the fluxes and volcanism age. The Hawai'ian chain has a larger vertical scale compared to the other chains to identify the maxima in Q_s and Q_v. The figure is modified from Adam et al. (2007).

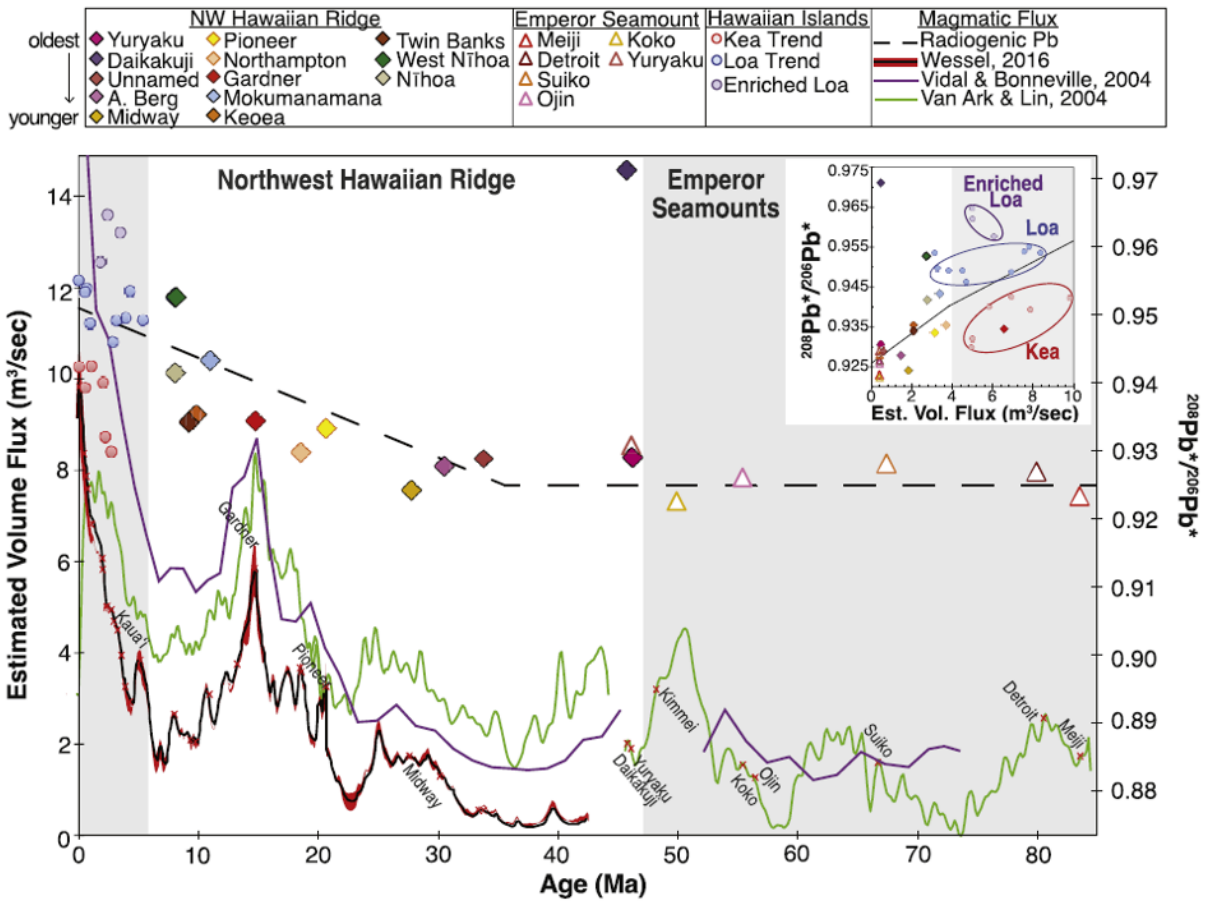

Figure 5.4. Correlation between estimated volume flux (magmatic flux) of the Hawai'ian-Emperor chain and $^{208}Pb^*/^{206}Pb^*$ isotopes.

Different magmatic fluxes of Hawai'i-Emperor seamount chain from previous studies are illustrated by the different colored curved lines, becoming more precise with time. Hawai'ian islands are represented by circles, Emperor seamounts are triangles, and the Hawai'ian ridge is diamonds. The radiogenic Pb is the dashed blue line. Hawai'ian islands have a larger concentration of $^{208}Pb^*/^{206}Pb^*$ isotopes, and the Emperor seamounts have the smallest. The $^{208}Pb^*/^{206}Pb^*$ ratio was calculated by $\frac{^{208}Pb^*}{^{206}Pb^*} = \frac{(\frac{^{208}Pb}{^{204}Pb})_{Sample} - (\frac{^{208}Pb}{^{204}Pb})_{Initial}}{(\frac{^{206}Pb}{^{204}Pb})_{Sample} - (\frac{^{206}Pb}{^{204}Pb})_{Initial}}$. Figure and equation are from Harrison et al. (2017)

However, we don't have any isotopic data like in Harrison et al. (2017) along the youngest part of the Louisville chain. Fitton et al. (2021) conducted a study along the older

segments of the Louisville and Hawai'ian chains, a detailed description of this study can be found in Section 5.3. They could not confirm that the variations seen in the melt production were dependent on the differences in lithospheric thickness (Fitton et al. 2021). The authors were able to confirm that the potential temperature under the Louisville chain would be cooler than the potential temperature under the Hawai'ian chain (Nichols et al. 2014; Fitton et al. 2021). Thus, the increase in Q_s and Q_v can be associated with an increase in melt production rate (these variations are unrelated to lithospheric thickness variations), increase in plume temperature, or a change in the plume's source composition.

5.1.3 Comparison of variations

The 10 m.y. wavelength features from the Louisville track have also been noticed in the maxima of the Walvis, St. Helena, and Hawai'ian chains (Vidal and Bonneville, 2004; Adam et al., 2007). Along the Louisville hotspot track, we observe maxima at 2, 12, and 23 Ma that coincide with maxima in in Q_s and Q_v (blue arrows on Figure 5.1). Other studies point out similar peaks at 10, 38, and 54 Ma for the Walvis Ridge, along with 10 and 30 Ma for the St. Helena (Adam et al., 2007), and 3 and 15 Ma for the Hawai'ian chain (Vidal and Bonneville, 2004) (Figure 39). In general, plumes located on the Pacific plate (Louisville and Hawai'i) have peaks occurring roughly at the same long-term variation periods in Q_s and Q_v, 10 m.y. (Vidal and Bonneville, 2004). The Atlantic plumes (Walvis and St. Helena) have corresponding Q_s and Q_v peaks that occur at a 20 m.y. period (Adam et al., 2007). Several hypotheses have been suggested to explain such variations with a 10 – 20 m.y. periodicity. Whitehead (1982) and Steinberger (2000) propose that these variations are due to a plume conduit that is tilted. The tilt of the plume conduit is created by the lithosphere drifting at the top of the plume. Over time, as the lithosphere is moving, the tilt will continue to increase (Whitehead, 1982). This tilt could be

caused by large scale mantle advection, and if the tilt is more than 60^{o} from the vertical, then the conduit begins to break up, causing a cease in magmatism (i.e., becomes unstable), and may produce oscillations (Whitehead, 1982). Steinberger (2000) reports that the tilt of the Louisville plume conduit may be 78^{o}, 74^{o}, or 55^{o}. Even though the tilt of Louisville's conduit could be larger than 60^{o}, Steinberger (2000) states the plume can still survive. The explanation is based on the viscosity of the surrounding mantle. If the surrounding mantle is highly viscous ($\geq$ ~3 x 10^{22} Pas), then the conduits instability will slowly develop, allowing magmatism to continue. If the surrounding mantle has low viscosity ($\leq$ ~5 x 10^{21} Pas), then broken pieces of the conduit will rise quickly through the conduit, allowing magmatic material to continue to flow through it (Steinberger, 2000). This mechanism has already been invoked by Koppers et al. (2004) to account for the scattered seamount distribution and their volcanic ages, along Louisville.

The short-term, 5 m.y. long variations seen along the Louisville chain (green dashed ellipses on Figure 5.2) have also been observed in the Q_s and Q_v along the St. Helena, Walvis, and Hawai'i chains (Vidal and Bonneville, 2004; Adam et al., 2007). For the St. Helena, Walvis, and Hawai'ian chains, these variations are identified as dashed green ellipses in Figure 5.3. They can be caused by the presence of solitary waves found within the plume conduit (Whitehead and Helfrinch, 1990; Vidal and Bonneville, 2004; Adam et al. 2007). These could form in the plume conduit after it has been deformed by mantle motions, or form due to plume flux variations, or to pressure variations (Olson and Christensen, 1986; Schuber et al. 1989; Olson, 1990). Olson and Christensen (1986) created a model for solitary wave formation by combining two fluids with low viscosity and density into a matrix fluid with a higher viscosity and density. Fluid A was made up of water and ethyl alcohol, fluid B was made up of a sucrose solution, water, and ethyl alcohol, and the matrix fluid is a water and sucrose solution (Olson and Christensen, 1986). They

found two different forms of waves could form: solitary waves that travel up the conduit quickly, and periodic waves tarins that travel slowly (Olson and Christensen, 1986). Figure 5.5 illustrates the formation of the waves found plume conduits in a laboratory-based setting. As these waves are generated, they travel upward towards the surface without any changes to their physical features (i.e., shape and size) (Data et al. 2018). The presence of solitary waves has been used to explain isotopic heterogeneities (West et al. 1987) and why plume material rises quickly through the conduit (Whitehead and Helfrich, 1988; 1990). This upwelling model occurs ten to fifteen times faster than those proposed through fluid mechanics (Whitehead and Helfrinch, 1988). In this study, we are able to confirm that all long-lived hotspots exhibit variations at ~5 m.y. wavelengths.

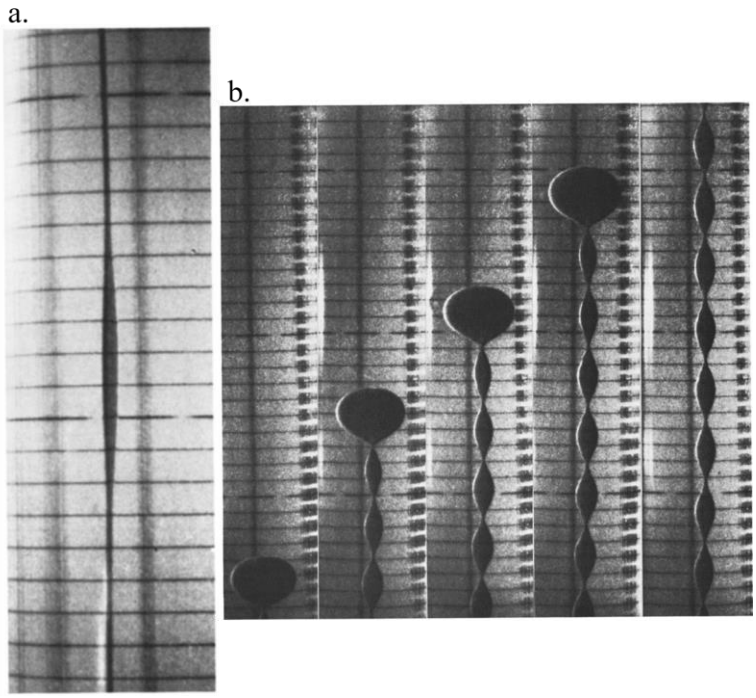

Figure 5.5. Waves within a plume conduit.
Modified from Olson and Christensen (1986). Both panels illustrate the results from Olson and Christensen experiment of fluid A interacting with the matrix fluid. (a.) A solitary wave traveling up the plume conduit. (b.) Propagating wave train traveling up the plume conduit.

5.2 Quantitative comparison with Hawai'i

Before comparing the total volumes of all four chains, we want to take a closer look at the Louisville seamount chain and Hawai'ian volcanic chain. The comparison with Hawaii is particularly interesting, as Louisville and Hawaii are both located on the Pacific plate. The amplitude of the swell and magmatic fluxes differs between Hawaii and Louisville because the swell associated with Hawai'i has a larger width. In Figure 5.5, the amplitude of the Hawai'ian swell is about 1200-1500 m, while the swell associated with Louisville has a 300 m amplitude. In Figure 39, The maximum Q_s for Hawaii is 2 m^3s^{-1}, while for Louisville the maximal Q_s values are around 0.4 m^3s^{-1}, these values are compared to one another in Table 4. Between these two observations, the ratio Q_s Hawaii/Q_s Louisville varies between 4 and 5. Moreover, the swell associated with Hawai'i has a larger width. The swell morphology accounts for the different Q_s ranges found for these two chains.

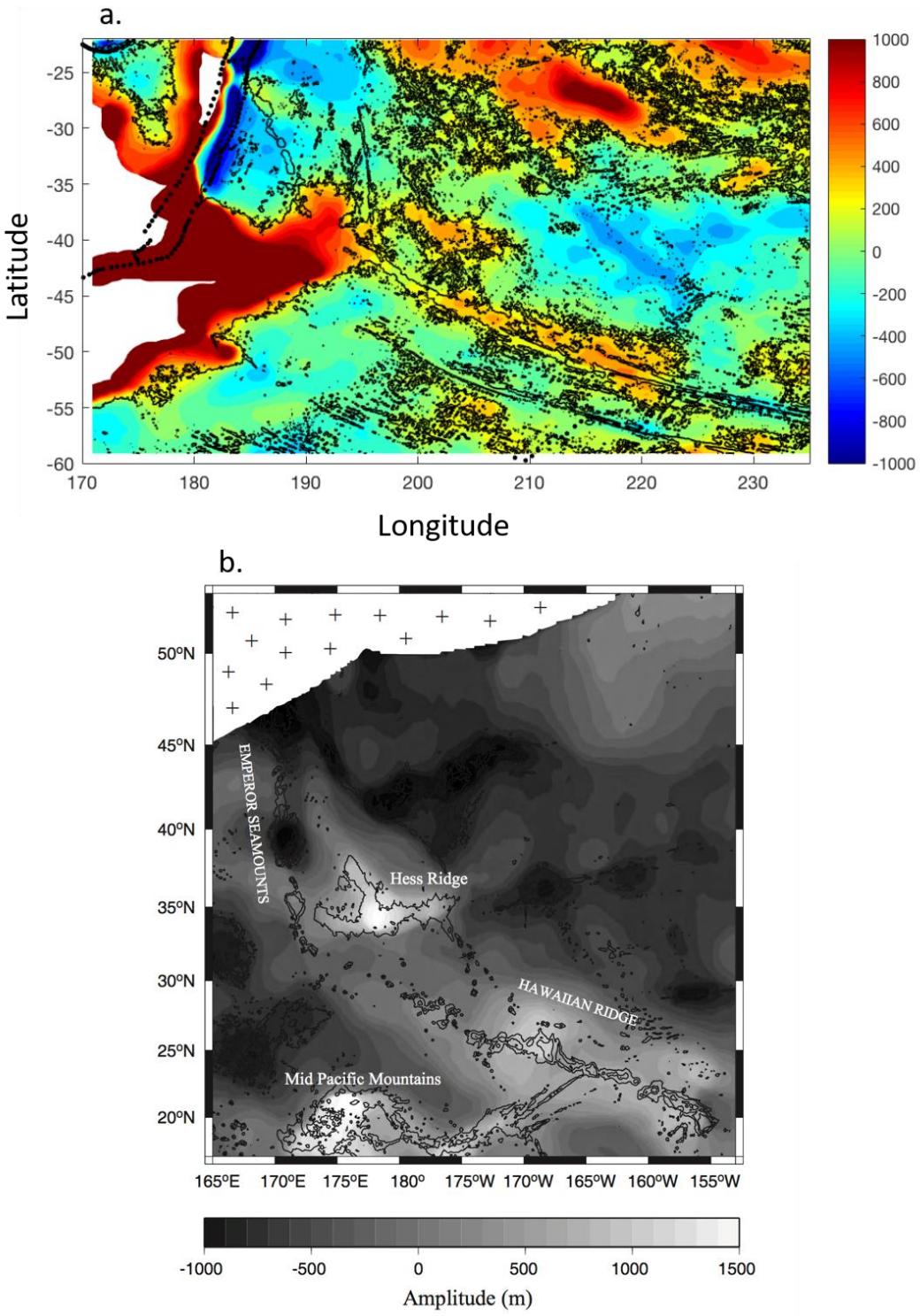

Figure 5.6. Swell maps of the (a) Louisville and (b) Hawai'i-Emperor seamount chains. (a) Present study, (b) from Vidal and Bonneville (2004).

Table 4. Qs Hawai'i/Qs Louisville and Qv Hawai'i/Qv Louisville

	Q_s Hawai'i/Q_s Louisville	Q_v Hawaii/Q_v Louisville
Ratio	4/5	7/8

The Q_v ranges are also different when comparing Hawaii and Louisville in Table 4. Q_v has a maximal value of 20 m^3s^{-1} along the youngest part of Hawaii. For volcanism ages older than 5 Ma, Q_v varies between 0 and 10 m^3s^{-1} along this chain. Such a drastic spike in Q_v for young ages is not observed along the Louisville chain. Along Louisville, Q_v varies between varies between 0 and 1.4 m^3s^{-1}. The ratio Q_v Hawaii/Q_v Louisville is around 7-8. This is explained by considering the volume of the volcanoes (Figure 5.6). The radii of the Louisville volcanoes vary between 40 and 50 km, and their height between 3200 and 4400 m (Figure 5.6a, b). For Hawaii, the radii of the volcanoes are 100-150 km, and their height varies between 5000 and 9200 m (Figure 5.6 a, b). We calculated their respective volumes of the volcanic edifices by using the formula for the volume of a cone, $V = \pi(r)^2*(h/3)$, where h is the cone height and r its radius. The volume of the Louisville volcanoes varies between 7 and 8 $x10^3$ km^3. Profile CC' passes through the big island of Hawai'i which is made up of five different volcanoes. While profile CC' is mainly crossing through Mauna Loa, it also intersects Mauna Kea which is acceptable because the volcanic edifice can be composed of several volcanoes. The volume calculated for Mauna Loa and Mauna Kea is 116.6 $x10^3$ km^3. Profile DD' passes through the Maui island and intersects the West Maui volcano. profile has a volume of 54.2 $x10^3$ km^3. The ratio between the volume of the volcano located along the DD' profile and the volume of the volcano located along the BB' profile is 7.3, similar to the ratio Qv Hawaii/Qv Louisville ratio. Although this may seem circular, we had to make sure the values we provide for Q_s and Q_v are correct, and that they can be accounted for by the morphology of the volcanoes and the swell.

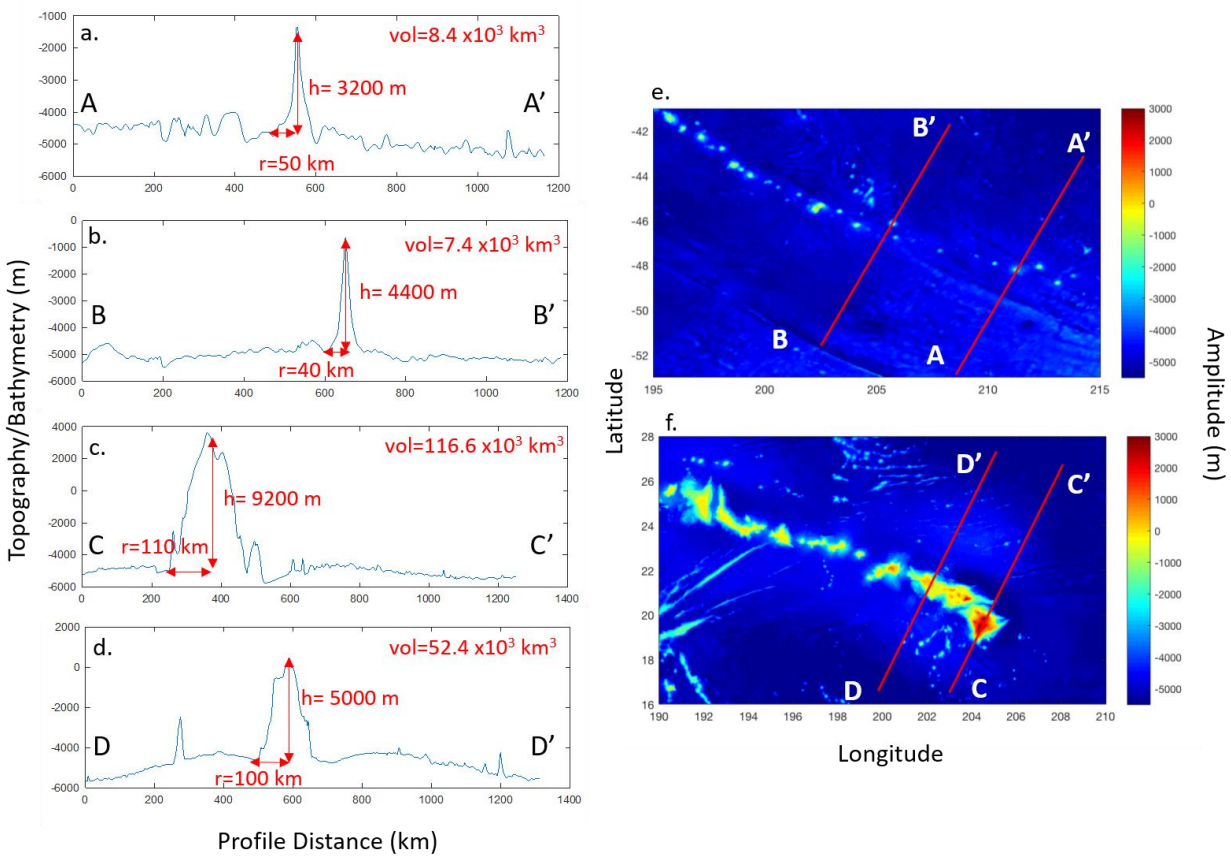

Figure 5.7. Volume of volcanoes along (e) Louisville and (f) Hawai'i hotspot tracks. Depth cross sections showing the bathymetry along Louisville (a, b), and Hawai'i. The maps in panels e and f show the locations of the profiles. Volcanic edifices are often composed by several volcanoes.

5.3. Total volumes and fluxes

The magmatic and swell volumes for the Louisville seamount chain are compared to the results from Vidal and Bonneville (2004) and Adam et al. (2007) in Table 5. Louisville has the smallest magmatic volume at 6.23 x 10^5 km^3 while Hawai'i has the largest at 61.80 x 10^5 km^3. Louisville also has a low swell volume at 2.85 x 10^5 km^3, but St. Helena has the smallest at 2.33 x 10^5 km^3.

The Louisville buoyancy flux, B, is 0.65 Mg s^{-1}. In previous studies done Sleep (1990) and Davies (1988), the Louisville buoyancy flux is reported to be 0.9 Mg s^{-1} and 3.0 Mg s^{-1}

respectively. King and Adam (2014) assess the uncertainties associated with the determination of the buoyancy flux by studying the uncertainties of several factors required to compute the buoyancy fluxes, and placed the buoyancy flux between 0.38 and 0.63 Mg s^{-1} for Louisville. Here we find a similar value, B = 0.65 Mg s^{-1}.

While comparing the buoyancy flux along the different long-lived hotspot chains, we can see that Hawai'i has the largest value (B = 1.75 Mg s^{-1}) while St. Helena has the smallest (B = 0.37 Mg s^{-1}). The value of the buoyancy flux has been used as a criterion to distinguish between deep plumes, for which B > 1 Mg s^{-1}, and shallow plumes for which B < 1 Mg s^{-1} (Albers and Christensen, 1996; Davies, 1988; Sleep, 1990; Courtillot er al., 2003; King and Adam, 2014).

According to the value found in the present study, (B = 0.65 Mg s^{-1}), and to the values found by King and Adam (2014) (B = 0.38 – 0.63 Mg s^{-1}), Louisville's plume would be a shallow plume which could potentially initiate at the boundary layer between the upper and lower mantle (see discussion in the *Introduction* and Courtillot et al. (2003)). However, the reliability of using the buoyancy as a way to distinguish a deep or shallow origin is debated (King and Adam, 2014). As such, we need to consider other arguments for constraining the origin of the Louisville plume.

Table 5. Magmatic and swell volumes and fluxes for the Louisville, St. Helena, Walvis, and Hawai'i chains.

Data for St. Helena, Walvis, and Hawai'i are from Adam et al. (2007).

	Magmatic Volume ($x10^5$ km^3)	Swell Volume ($x10^5$ km^3)	Magmatic Flux (m^3s^{-1})	Swell Flux (m^3s^{-1})	Buoyancy flux (Mg s^{-1})
Louisville	6.23	2.85	0.84	0.28	0.65
St. Helena	11.10	2.33	0.76	0.16	0.37
Walvis	21.40	8.79	1.00	0.41	0.96
Hawai'i	61.80	10.00	4.70	0.76	1.75

According to other authors, the Louisville chain is not created by a plume (Jackson et al., 2021; Fitton et al., 2021). Jackson et al. (2021) used a seismic model modified from the Boschi et al. (2007) tomography model to measure the 'connected conduit length' (i.e., fraction of mantle depth over negative seismic velocity anomalies of the conduits). They found that on average, plume conduits extend across 60% of the mantle (Jackson et al., 2021). They use this value to define whether or not a hotspot is the product of a deep mantle plume, i.e., if the conduit extends over ≥60% of the mantle, then there is a plume present. Jackson et al. (2021) report that the average length for Louisville hotspot conduit is about ~50%, meaning that it does not originate from a deep-mantle plume. However, tomography models such as the one they considered have a lateral resolution on the order of ~200-400 km. This resolution can complicate identification of small plumes (Jackson et al., 2021). Based on the small size of the Louisville volcanoes, and small swell fluxes, the Louisville plume should be relatively small.

Fitton et al. (2021) studied the geochemistry (i.e., major- and trace- elements, REE, and isotopic data) on some of the older seamounts along the Louisville and Hawai'ian chains. Along the Louisville chain, they found that the seamounts are made up of alkali basalts. For these basalts to form, there had to be ~1.5 – 3% partial melting of a garnet-lherzolite mantle. Meanwhile, the Emperor seamounts are composed of tholeiitic and alkali basalts which formed with a 2 – 10% partial melting of a spinel- to garnet-lherzolite mantle (Fitton et al., 2021). They propose a decompression melting model to explain the composition of the Louisville seamount chain, where a cool plume (1350 – 1400^{o} C) experiences dehydration melting of the mantle (Fitton et al., 2021). Or there may not be a plume at all, and the seamount chain formed due to the peridotite-based mantle sources undergoing decompression melting that contain silica-oversaturated and carbonated eclogite in the upper mantle flow (Fitton et al., 2021). This

contradicts other geochemical studies, such as one done on $^{3}He/^{4}He$ isotopic data by Hanyu (2014).

Helium, and other noble gases, isotopic data are used to measure the amount of degassing the Earth has gone through, to observe the composition of the mantle, and to understand how the atmosphere formed (Farley and Neroda, 1998). Helium is a unique noble gas because it's rarely found in Earth's atmosphere, with a measurement of 1.39 R_A (1.39×10^{-6}) compared to the range of values found throughout the mantle, 3 – 30 R_A (Farley and Neroda, 1998). Mid-oceanic ridges (MORBs) generally have a $^{3}He/^{4}He$ ratio of 7 – 9 Ra (Farley and Neroda, 1998; Hanyu, 2014). If a hotspots $^{3}He/^{4}He$ ratio is larger than the MORB's average, than it's plume source is found in the deep mantle, if the ratio is lower than it has a shallower plume source (Farley and Neroda, 1998; Courtillot et al., 2003; Hanyu, 2014). Hanyu (2014) reports that lavas from the Louisville seamount chain have $^{3}He/^{4}He$ ratios ranging values similar to Pacific mid-oceanic ridge basalts up to 10.6 Ra. Since this ratio is larger than the MORB range, Hanyu (2014) proposes that Louisville's plume may have a deep mantle origin. If we are using the classification from Courtillot et al. (2003), as mentioned in section 1.1, Louisville would have a deep plume initiating at the core-mantle boundary.

A strong argument for the existence of a plume (shallow or deep) at the origin of the Louisville chain is the trail of volcanoes, created continuously in the past 80 m.y. (Figure 3.1). Such a volcanic track only forms if a mantle plume interacts with a moving lithosphere moving on top of it (Crough, 1983). Thus, it is difficult to find an alternative explanation for the existence of the volcanoes composing the Louisville chain, characterized by a linear age progression (Figure 3.1).

To summarize, there is still an ongoing debate on the origin of the Louisville chain. Chemical studies provide arguments for a shallow to a deep plume origin or for an absence of a plume, while geophysical studies, point to a shallow origin. Based off of this study, the calculated B value is smaller than 1 Mg s^{-1}, indicating a shallow origin for the Louisville plume (King and Adam, 2014).

Chapter 6 - Conclusions

The goal of this research was to examine the temporal evolution of the swell (Q_s) and magmatism (Q_v) fluxes along the Louisville hotspot in order to characterize the temporal evolution of the plume activity, and its interaction with the lithosphere drifting at the surface mantle. To do this, we used the MiFil filtering method (Adam et al., 2005) to separate the swell and magmatic components of the dynamic topography. The MiFil method is a two stages calculation that requires a minimization step plus filtering through a median filter. We show that the best filter radius to characterize the swell along Louisville is 20 km, whereas the radius for the minimizing median filters is 250 km.

The sliding box method was then used to assess the temporal evolution of the swell and magmatic fluxes along the Louisville seamount from 0 to 35 Ma. We consider the youngest part of the chain because the bathymetry of the older segment is influenced by Hikurangi plateau (Ito and van Keken, 2007). The swell and magmatic volumes encompassed in this box are computed for each iteration step. We tested the parameters of this box (length, width, translating step) in order to make sure that these parameters do not have an influence on the computed fluxes. We showed that the length of the box has to be 700 km in order to encompass the swell and volcanoes associated with the Louisville chain. We showed that the width of the box has to be 50 km in order to identify all the fluxes temporal variations, while excluding variations at the scale of volcanoes. By testing the translation step, we were testing the influence of the overlapping of the sliding boxes. We presented our results with a translating step of 25 km, corresponding to a 50% overlap of the sliding boxes.

Our results show that the swell and magmatic flux associated with the Louisville hotspot have been increasing for the past ~35 m.y., suggesting an increase in plume activity over that

time frame. This contrasts with the results of Londsdale (1988) who suggest that the Louisville plume has been in decline.

Similar to the Louisville hotspot, fluxes for the Hawai'ian have been increasing for the past ~30 m.y. years, whereas the fluxes for the Walvis and St. Helena hotspot have been decreasing for the past ~60 – 80 m.y. (Vidal and Bonneville, 2004; Adam et al., 2007). The increase in plume activity for the Louisville and Hawai'i hotspots could be caused by increase in material supplied by the plume, an increase in plume temperature, variations in the degree of melting not related to variations in lithosphere thickness (White, 1993; Regelous et al., 2003; Vidal and Bonneville, 2004). The plumes activity could also increase if the plumes source composition were to change (Harrison et al., 2017). As the Hawai'ian chain's magmatic flux has been increasing, so has the signature of $^{208}Pb/^{206}Pb$ isotopes, whereas the Emperor seamounts isotopic signature remained constant (Harrison et al., 2017). This is because the Hawai'ian plume migrated from a depleted mantle outside the large low shear velocity providence (LLSVP), to a more enriched environment in the LLSVP, indicating that the plumes source composition can influence the magmatic flux (Harrison et al., 2017).

Q_s and Q_v, i.e., the swell and magmatic fluxes, exhibit peaks along the Louisville chain at 2, 12, and 23 Ma. Such peaks with a 10 – 20 m.y. periodicity have also been reported for both the Hawai'ian chain, and at a 20-30 m.y. periodicity for the Walvis, and St. Helena chains (Adam et al., 2007). These variations have been attributed to a tilt in the plume conduit (Whitehead, 1982; Steinberger, 2000). A similar explanation may apply to the Louisville hotspot chain.

Along the Louisville chain, we also observe shorter wavelength variations (~5 m.y.) in both Q_s and Q_v. Such variations, with a 5 m.y., periodicity have also been reported for the

Hawai'ian, Walvis, and St. Helena chains (Vidal and Bonneville, 2004; Adam et al., 2007). These variations have been attributed to the presence of solitary waves within the plume conduit (Whitehead and Helfrinch, 1990; Vidal and Bonneville, 2004; Adam et al. 2007). The solitary waves are believed to be the result of interaction between the ascending plume and the convection mantle (Olson and Christensen, 1986; Schubert et al. 1989; Olson, 1990).

We calculated the magmatic and swell volumes to be 6.23×10^5 km^3 and 2.85×10^5 km^3 respectively. Of the four hotspot chains we considered, i.e., Louisville, Hawai'i, Walvis, and St. Helena, Louisville has the smallest magmatic volume, while St. Helena has the smallest swell volume. The mean values of the magmatic and swell fluxes along Louisville are 0.84 $m^3 s^{-1}$ and 0.28 $m^3 s^{-1}$, respectively. They are higher than the fluxes of St. Helena, but smaller than the fluxes found for Walvis and Hawaii.

According to a recent geodynamic study by Jackson et al. (2021), the Louisville hotspot is classified as a non-plume, but this analysis conflicts with geochemical studies based on noble gases that indicated a deep origin for the Louisville plume (Hanyu, 2014). The results of this thesis shed light on this controversy. We find the buoyancy flux, B, associated with Louisville is 0.65 Mg s^{-1}, similar to the values reported by King and Adam (2014). The value of the buoyancy flux has been used as a criterion for distinguishing between deep plumes, for which $B > 1$ Mg s^{-1}, and shallow plumes, for which $B < 1$ Mg s^{-1} (Albers and Christensen 1996; Davies, 1988; Sleep, 1990; Courtillot et al., 2003; King and Adam, 2014). The value found in the present study, ($B = 0.65$ Mg s^{-1}), gives distinctive evidence that Louisville's plume has a shallow origin, most likely initiating at the boundary layer between the upper and lower mantle.

References

Adam, C., & Bonneville, A. (2008). No thinning of the lithosphere beneath northern part of the Cook-Austral volcanic chains. *Journal of Geophysical Research, 113*(B10). doi:10.1029/2007jb005313

Adam, C., Vidal, V., & Bonneville, A. (2005). MiFil: A method to characterize seafloor swells with application to the south central Pacific. *Geochemistry, Geophysics, Geosystems, 6*(1). doi: 10.1029/2004gc000814

Adam, C., Vidal, V., & Escartín, J. (2007). 80-Myr history of buoyancy and volcanic fluxes along the trails of the Walvis and St. Helena hotspots (South Atlantic). *Earth and Planetary Science Letters, 261*(3-4), 432–442. doi: 10.1016/j.epsl.2007.07.005

Adam, C., Yoshida, M., Isse, T., Suetsugu, D., Fukao, Y., & Barruol, G. (2010). South Pacific hotspot swells dynamically supported by mantle flows. *Geophysical Research Letters, 37*(8). doi: 10.1029/2010gl042534

Albers, M., & Christensen, U. R. (1996). The excess temperature of plumes rising from the core-mantle boundary. *Geophysical Research Letters, 23*(24), 3567-3570. doi:10.1029/96gl03311

Anderson, D. L. (1998). The EDGES of the mantle. *The Core-Mantle Boundary Region Geodynamics Series*, 255–271. doi: 10.1029/gd028p0255

Anderson, D. L. (2000). The thermal state of the upper mantle; No role for mantle plumes. *Geophysical Research Letters, 27*(22), 3623–3626. doi: 10.1029/2000gl011533

Becker, J. J., Sandwell, D. T., Smith, W. H. F., Braud, J., Binder, B., Depner, J., … Weatherall, P. (2009). Global Bathymetry and Elevation Data at 30 Arc Seconds Resolution: SRTM30_PLUS. *Marine Geodesy, 32*(4), 355–371. doi: 10.1080/01490410903297766

Bercovici, D., & Kelly, A. (1997). The non-linear initiation of diapirs and plume heads. *Physics of the Earth and Planetary Interiors, 101*(1-2), 119–130. doi: 10.1016/s0031-9201(96)03217-7

Betz, F., & Hess, H. H. (1942). The Floor of the North Pacific Ocean. *Geographical Review, 32*(1), 99–116. doi: 10.2307/210361

Boschi, L., Becker, T. W., & Steinberger, B. (2007). Mantle plumes: Dynamic models and seismic images. *Geochemistry, Geophysics, Geosystems, 8*(10). doi:10.1029/2007gc001733

Burke, K. C., & Wilson, J. T. (1976). Hot Spots on the Earths Surface. *Scientific American, 235*(2), 46–59. doi: 10.1038/scientificamerican0876-46

Clouard V. and Bonneville A., Ages of Seamounts and Plateaus on the Pacific Plate, in Foulger G. R., Natland J.H. Prensnall D.C., and Anderson D. L. (2005). *Plates, Plumes and Paradigms, Geological Society of America Special Papers* vol. 388, 71-90.

Courtillot, V., Davaille, A., Besse, J., & Stock, J. (2003). Three distinct types of hotspots in the Earth's mantle. *Earth and Planetary Science Letters, 205*(3-4), 295–308. doi: 10.1016/s0012-821x(02)01048-8

Crough, S. T. (1983). Hotspot Swells. *Annual Review of Earth and Planetary Sciences, 11*(1), 165–193. doi: 10.1146/annurev.ea.11.050183.001121

Dalrymple, G. B., & Clague, D. (1976). Age of the Hawaiian-Emperor bend. *Earth and Planetary Science Letters, 31*(3), 313–329. doi: 10.1016/0012-821x(76)90113-8

Dalrymple. G.B., L., & Clague, D. (1980). Conventional and 40Ar/39Ar k-ar ages of volcanic rocks from ŤJIN (site 430), Nintoku (SITE 432), And suiko (Site 433) seamounts and the chronology of Volcanic propagation along THE Hawaiian-Emperor Chain. *Initial Reports of the Deep Sea Drilling Project*. doi:10.2973/dsdp.proc.55.128.1980

Datta, D., Jagtap, S., & Gaikwad, U. (2018). Application of Differential Quadrature for Modeling Solitary Wave: Numerical Solution of KDV Equation. *International Journal of Computer Applications*, *182*(20), 39–42. https://doi.org/10.5120/ijca2018917990

Davaille, A., Girard, F., & Bars, M. L. (2002). How to anchor hotspots in a convecting mantle? *Earth and Planetary Science Letters, 203*(2), 621–634. doi: 10.1016/s0012-821x(02)00897-x

Davies, G. F. (1988). Ocean bathymetry and mantle convection: 1. Large-scale flow and hotspots. *Journal of Geophysical Research: Solid Earth, 93*(B9), 10467-10480. doi:10.1029/jb093ib09p10467

Davies, G. F. (1992). Temporal variation of the Hawaiian plume flux. *Earth and Planetary Science Letters, 113*(1-2), 277–286. doi: 10.1016/0012-821x(92)90225-k

Detrick, R. S., & Crough, S. T. (1978). Island subsidence, hot spots, and lithospheric thinning. *Journal of Geophysical Research, 83*(B3), 1236–1244. doi: 10.1029/jb083ib03p01236

Divins, D.L., 2011. NGDC total sediment thickness of the world's oceans & marginal seas. http://www.ngdc.noaa.gov/mgg/sedthick/sedthick.html.

Farley, K. A., & Neroda, E. (1998). Noble gases in the earth's mantle. *Annual Review of Earth and Planetary Sciences, 26*(1), 189-218. doi:10.1146/annurev.earth.26.1.189

Fitton, J. G., Williams, R., Barry, T. L., & Saunders, A. D. (2021). The role of Lithosphere thickness in the formation of Ocean Islands and Seamounts: Contrasts between the Louisville and Emperor-Hawaiian Hotspot Trails. *Journal of Petrology, 61*(11-12). doi:10.1093/petrology/egaa111

Garcia, M. O., Swinnard, L., Weis, D., Greene, A. R., Tagami, T., Sano, H., & Gandy, C. E. (2010). Petrology, geochemistry and Geochronology OF Kaua'i Lavas over 4·5 Myr: Implications for the origin of Rejuvenated volcanism and the evolution of the Hawaiian plume. *Journal of Petrology, 51*(7), 1507-1540. doi:10.1093/petrology/egq027

Hanyu, T. (2014). Deep plume origin of the LOUISVILLE Hotspot: Noble gas evidence. *Geochemistry, Geophysics, Geosystems, 15*(3), 565-576. doi:10.1002/2013gc005085

Harrison, L. N., Weis, D., & Garcia, M. O. (2017). The link between Hawaiian mantle plume composition, Magmatic flux, and deep mantle geodynamics. *Earth and Planetary Science Letters, 463,* 298-309. doi:10.1016/j.epsl.2017.01.027

Hill, D. P., & Zucca, J. J. (1987). Geophysical constraints on the structure of Kilauea and Mauna Loa volcanoes and some implications for seismomagmatic processes. *US Geological Survey Professional Paper, 1350*(2), 903-917.

Ito, G., & van Keken, P. V. (2007). Hot Spots and Melting Anomalies. *Treatise on Geophysics*, 371–435. doi: 10.1016/b978-044452748-6.00123-1

Jackson, M. G., Becker, T. W., & Steinberger, B. (2021). Spatial characteristics of recycled and primordial reservoirs in the deep mantle. *Geochemistry, Geophysics, Geosystems, 22*, e2020GC009525. https://doi.org/10.1029/2020GC009525

King, S. D., & Adam, C. (2014). Hotspot swells revisited. *Physics of the Earth and Planetary Interiors, 235,* 66–83. doi: 10.1016/j.pepi.2014.07.006

Koppers, A. A. P., Duncan, R. A., & Steinberger, B. (2004). Implications of a nonlinear40Ar/39Ar age progression along the Louisville seamount trail for models of fixed and moving hot spots. *Geochemistry, Geophysics, Geosystems, 5*(6). doi: 10.1029/2003gc000671

Koppers, A. A. P., Gowen, M. D., Colwell, L. E., Gee, J. S., Lonsdale, P. F., Mahoney, J. J., & Duncan, R. A. (2011). New40Ar/39Ar age progression for the Louisville hot spot trail and implications for inter-hot spot motion. *Geochemistry, Geophysics, Geosystems, 12*(12). doi: 10.1029/2011gc003804

Lindwall, D. A. (1988). A two-dimensional seismic investigation of Crustal structure under the Hawaiian islands near Oahu and Kauai. *Journal of Geophysical Research, 93*(B10), 12107. doi:10.1029/jb093ib10p12107

Lonsdale, P. (1988). Geography and history of the Louisville Hotspot chain in the southwest Pacific. *Journal of Geophysical Research, 93*(B4), 3078. doi:10.1029/jb093ib04p03078

McNutt, M. (1980). Implications of Regional gravity for state of stress in the Earth's crust and upper mantle. *Journal of Geophysical Research: Solid Earth, 85*(B11), 6377-6396. doi:10.1029/jb085ib11p06377

Mcnutt, M., & Bonneville, A. (2000). A shallow, chemical origin for the Marquesas Swell. *Geochemistry, Geophysics, Geosystems, 1*(6). doi: 10.1029/1999gc000028

Menard, H. W. (1964). *Marine geology of the Pacific*. New York: McGraw-Hill.

Müller, R. D., Sdrolias, M., Gaina, C., & Roest, W. R. (2008). Age, spreading rates, and spreading asymmetry of the worlds ocean crust. *Geochemistry, Geophysics, Geosystems, 9*(4). doi: 10.1029/2007gc001743

Nichols, A. R. L., Beier, C., Brandl, P. A., Buchs, D. M. & Krumm, S. H. (2014). Geochemistry of volcanic glasses from the Louisville Seamount Trail (IODP Expedition 330): Implications for eruption environments and mantle melting. *Geochemistry, Geophysics, Geosystems 15*, 1718–1738, doi:10.1002/2013GC005086

Nishimura, C. E., & Forsyth, D. W. (1989). The anisotropic structure of the upper mantle in the Pacific. *Geophysical Journal International, 96*(2), 203-229. doi:10.1111/j.1365-246x.1989.tb04446.x

O'Connor, J. M., & Duncan, R. A. (1990). Evolution of the Walvis Ridge-Rio Grande Rise Hot Spot System: Implications for African and South American Plate motions over plumes. *Journal of Geophysical Research, 95*(B11), 17475. doi: 10.1029/jb095ib11p17475

O'Connor, J. M., & le Roex, A. P. L. (1992). South Atlantic hot spot-plume systems: 1. Distribution of volcanism in time and space. *Earth and Planetary Science Letters, 113*(3), 343–364. doi: 10.1016/0012-821x(92)90138-l

Olson, P. (1990). Hot spots, swells and mantle plumes, *Magma Transport and Storage*, edited by MP Ryan, 33–51.

Olson, P., & Christensen, U. (1986). Solitary wave propagation in a Fluid conduit within a Viscous matrix. *Journal of Geophysical Research, 91*(B6), 6367. doi:10.1029/jb091ib06p06367

Olson, P., Schubert, G., & Anderson, C. (1987). Plume formation in the D″-layer and the roughness of the core–mantle boundary. *Nature, 327*(6121), 409–413. doi: 10.1038/327409a0

Parsons, B., & Sclater, J. G. (1977). An analysis of the variation of ocean floor bathymetry and heat flow with age. *Journal of Geophysical Research, 82*(5), 803-827. doi:10.1029/jb082i005p00803

Pertermann, M., & Hirschmann, M. M. (2003). Partial melting experiments on a MORB-like pyroxenite between 2 and 3 GPa: Constraints on the presence of PYROXENITE in basalt source regions From solidus location and melting rate. *Journal of Geophysical Research: Solid Earth, 108*(B2). doi:10.1029/2000jb000118

Regelous, M., Hofmann, A. W., Acouchami, W., Galer, S. J. G. (2003). Geochemistry of lavas from the Emperor Seamounts, and the geochemical evolution of Hawaiian Magmatism from 85 to 42 Ma. *Journal of Petrology, 44*(1), 113-140. doi:10.1093/petrology/44.1.113

Richards, M. A., Duncan, R. A., & Courtillot, V. E. (1989). Flood Basalts and Hot-Spot Tracks: Plume Heads and Tails. *Science, 246*(4926), 103–107. doi: 10.1126/science.246.4926.103

Sandwell, D. T., Winterer, E. L., Mammerickx, J., Duncan, R. A., Lynch, M. A., Levitt, D. A., & Johnson, C. L. (1995). Evidence for diffuse extension of the Pacific Plate from Pukapuka ridges and cross-grain gravity lineations. *Journal of Geophysical Research: Solid Earth, 100*(B8), 15087–15099. doi: 10.1029/95jb00156

Schilling, J. G., Thompson, G., Kingsley, R., & Humphris, S. (1985). Hotspot—migrating ridge interaction in the South Atlantic. *Nature, 313*(5999), 187–191. doi: 10.1038/313187a0

Schubert, G., Olson, P., Anderson, C., & Goldman, P. (1989). Solitary waves in mantle plumes. *Journal of Geophysical Research, 94*(B7), 9523. doi:10.1029/jb094ib07p09523

Schubert, G., Turcotte, D. L., & Olson, P. (2001). *Mantle convection in the earth and planets*. Cambridge: Cambridge University Press.

Sleep, N. H. (1990). Hotspots and mantle plumes: Some phenomenology. *Journal of Geophysical Research, 95*(B5), 6715. doi: 10.1029/jb095ib05p06715

Sleep, N. H. (2002). Ridge-crossing mantle plumes and gaps in tracks. *Geochemistry, Geophysics, Geosystems, 3*(12), 1-33. doi:10.1029/2001gc000290

Sleep, N. H. (2002). Ridge-crossing mantle plumes and gaps in tracks. *Geochemistry, Geophysics, Geosystems, 3*(12), 1-33. doi:10.1029/2001gc000290

Smith, W. (1990). *Marine Geophysical studies of seamounts in the Pacific Ocean basin*. PhD thesis. Columbia University, New York.

Stein, C. A., & Stein, S. (1992). A model for the global variation in oceanic depth and heat flow with lithospheric age. *Nature, 359*(6391), 123–129. doi: 10.1038/359123a0

Steinberger, B. (2000). Plumes in a convecting mantle: Models and observations for individual hotspots. *Journal of Geophysical Research: Solid Earth, 105*(B5), 11127–11152. doi: 10.1029/1999jb900398

Vidal, V., & Bonneville, A. (2004). Variations of the hawaiian hot spot activity revealed by variations in the magma production rate. *Journal of Geophysical Research, 109*(B3). doi:10.1029/2003jb002559

Walcott, R. (1970). Flexure of the lithosphere at Hawaii. *Tectonophysics, 9*(5), 435–446. doi: 10.1016/0040-1951(70)90056-9

Watts, A. B., & Brink, U. S. T. (1989). Crustal structure, flexure, and subsidence history of the Hawaiian Islands. *Journal of Geophysical Research: Solid Earth, 94*(B8), 10473–10500. doi: 10.1029/jb094ib08p10473

Watts, A. B., & Ribe, N. M. (1984). On geoid heights and flexure of the lithosphere at seamounts. *Journal of Geophysical Research: Solid Earth, 89*(B13), 11152-11170. doi:10.1029/jb089ib13p11152

Watts, A. B., Bodine, J. H., & Ribe, N. M. (1980). Observations of flexure and the geological evolution of the Pacific Ocean basin. *Nature, 283*(5747), 532-537. doi:10.1038/283532a0

Watts, A. B., Cochran, J. R., & Selzer, G. (1975). Gravity anomalies And flexure of the lithosphere: A three-dimensional study of the Great Meteor Seamount, northeast Atlantic. *Journal of Geophysical Research, 80*(11), 1391-1398. doi:10.1029/jb080i011p01391

Watts, A. B., Ten Brink, U. S., Buhl, P., & Brocher, T. M. (1985). A multichannel seismic study of lithospheric flexure across the Hawaiian-Emperor seamount chain. *Nature, 315*(6015), 105-111. doi:10.1038/315105a0

Wessel, P. (1998). An empirical method for optimal robust regional-residual separation of geophysical data. *Mathematical Geology, 30*, 391-408. doi:10.1023/A:1021744224009

Wessel, P. and W. H. F. Smith, Free software helps map and display data, **EOS Trans. AGU**, 72, 441, 1991

West, H. B., Gerlach, D. C., Leeman, W. P., & Garcia, M. O. (1987). Isotopic constraints on the origin of Hawaiian lavas from the Maui Volcanic Complex, Hawaii. *Nature*, *330*(6145), 216–220. https://doi.org/10.1038/330216a0

White, R. (1993). Melt production rates in mantle plumes. *Philosophical Transactions of the Royal Society of London. Series A: Physical and Engineering Sciences, 342*(1663), 137-153. doi:10.1098/rsta.1993.0010

Whitehead, J. A. (1982). Instabilities of fluid conduits in a flowing earth -- are plates lubricated by the asthenosphere? *Geophysical Journal International*, *70*(2), 415–433. doi: 10.1111/j.1365-246x.1982.tb04975.x

Whitehead, J. A., & Helfrich, K. R. (1988). Wave transport of deep mantle material. *Nature, 336*(6194), 59–61. https://doi.org/10.1038/336059a0

Whitehead, J. A., & Helfrich, K. R., (1990). Solitary waves on conduits of buoyant fluid in a more viscous fluid. *Geophysical & Astrophysical Fluid Dynamics*, *51*(1-4), 35-52. doi:10.1080/03091929008219850

Whitehead, J. A., & Luther, D. S. (1975). Dynamics of laboratory diapir and plume models. *Journal of Geophysical Research*, *80*(5), 705–717. doi: 10.1029/jb080i005p00705

Wilson, J. T. (1963). A Possible Origin Of The Hawaiian Islands. *Canadian Journal of Physics, 41*(6), 863–870. doi: 10.1139/p63-094

Zucca, J. J., & Hill, D. P. (1980). Crustal structure of the southeast flank of Kilauea Volcano, Hawaii, from seismic refraction measurements. *Bulletin of the Seismological Society of America, 70*(4), 1149-1159.

Zucca, J. J., Hill, D. P., & Kovach, R. L. (1982). Crustal structure of Mauna Loa volcano, Hawaii, from seismic refraction and gravity data. *Bulletin of the Seismological Society of America, 72*(5), 1535-1550.

Appendix A - Latitudes, Longitudes, and Volcanic Ages

Table 6. Latitudes, longitudes, and volcanic ages of volcanoes along the Louisville chain. Original data was presented in degree, minuet, seconds. We converted the data to decimal degrees using https://www.rapidtables.com/convert/number/degrees-minutes-seconds-to-degrees.html. Original data is from Koppers et al. (2004; 2011).

Latitude °S	Longitude °W	Age ± 2σ (Ma)
25.5	186.0	76.7 ± 0.8
25.5	186.0	78.8 ± 1.3
27.5	185.7	70.8 ± 0.4
27.5	185.7	70.8 ± 0.4
27.5	185.7	69.6 ± 0.5
27.2	186.8	68.9 ± 0.6
30.1	186.8	61.4 ± 0.5
38.2	191.3	50.1 ± 0.4
38.2	191.3	49.4 ± 0.6
38.2	191.3	50.2 ± 0.5
28.0	191.7	50.9 ± 0.5
28.0	191.7	48.4 ± 0.3
28.0	191.7	47.4 ± 0.5
37.1	191.0	47 Ma
37.0	190.2	46.3 ± 0.9
38.3	192.3	45.5 ± 0.8
39.2	192.4	43.9 ± 0.3
39.2	192.4	44.7 ± 0.4
39.5	192.7	45.1 ± 0.3
39.7	193.3	43.3 ± 0.4
39.9	194.0	41.3 ± 0.3
40.5	194.3	41.0 ± 0.5
40.8	194.5	39.6 ± 0.3
40.5	194.3	39.9 ± 0.6
40.5	194.3	39.4 ± 0.2
40.5	194.3	40.4 ± 0.3
40.5	194.3	39.8 ± 0.3
40.8	194.5	39.6 ± 0.8
40.8	194.5	38.9 ± 1.2
41.9	205.3	34.5 ± 0.2

41.9	196.3	33.7 ± 0.5
41.9	196.3	34.5 ± 0.4
41.9	196.3	34.7 ± 0.5
40.8	194.7	33.9 ± 0.3
41.6	195.8	36.5 ± 0.4
43.6	198.5	30.3 ± 0.2
43.6	198.5	29.5 ± 0.3
43.6	198.5	32.2 ± 0.3
44.0	199.4	29.3 ± 0.3
44.0	199.4	26.3 ± 0.2
44.0	199.4	26.7 ± 0.2
44.3	200.2	25.6 ± 0.2
44.9	201.5	26.0 ± 0.3
44.9	201.5	26.2 ± 0.2
44.9	201.5	26.3 ± 0.3
44.6	199.9	25.0
45.4	202.3	24.6 ± 0.2
45.4	202.3	23.9 ± 0.3
45.4	202.3	24.6 ± 0.3
46.2	204.1	21.7 ± 0.3
46.2	204.1	21.5 ± 0.2
46.2	204.1	21.6 ± 0.2
48.2	211.2	13.2 ± 0.2
46.2	204.1	21.3 ± 0.2
50.4	220.9	1.11 ± 0.4